Awakening of the DRAGON

Commissioning of the DRAGON Recoil Separator Facility
&
First Studies on the $^{21}Na(p,\gamma)^{22}Mg$ Reaction

Sabine Engel

Ruhr-Universität Bochum

2003

Awakening of the DRAGON

Commissioning of the DRAGON Recoil Separator Experiment
&
First Studies on the $^{21}Na(p,\gamma)^{22}Mg$ Reaction

A Dissertation
Presented to the Faculty of Physics and Astronomy
of
Ruhr-Universität Bochum
in Candidacy for a Degree of
Doctor of Natural Sciences

By
Sabine Engel

2003

Contents

1 Motivation for the Present Work **1**

2 Astrophysical Interest in the DRAGON Experiment **2**
2.1 Scientific Program of the DRAGON Experiment 2
2.2 Oxygen-Neon-Novae 3
2.3 Type-I X-Ray Bursts 6

3 Theory of Resonant Capture Reactions **8**
3.1 Nuclear Cross Section 8
3.2 Stellar Reaction Rate Formalism 8
3.3 Narrow Isolated Resonances 11
3.4 Laboratory Yield of a Resonance Measurement 14
3.5 Inverse Kinematics 15
3.6 Error Analysis 17

4 The $^{21}Na(p,\gamma)^{22}Mg$ Reaction **18**

5 ISAC Beams **20**

6 The DRAGON Facility **22**
6.1 Gas Target 23
6.2 BGO Gamma Array 25
6.3 Recoil Mass Separator 26
6.3.1 Design of the Filters 29
6.3.2 DRAGON Ion Optics 29
6.4 Heavy Ion Detectors 31
6.5 Data Acquisition Electronics and Software 32

7 Commissioning of the DRAGON **33**
7.1 Properties of the Ion Beam 33
7.1.1 Experimental Set-Up 34
7.1.2 Energy Stability 35
7.1.3 Beam Energy Spread 39
7.2 Energy Calibration 41
7.2.1 Experimental Set-Up 41
7.2.2 Evaluation of the Results 42
7.3 Target Properties 44
7.3.1 DRAGON Gas Target in Detail 44
7.3.2 Target Profile 45
7.3.3 Total Target Thickness 48
7.3.4 Target Gas Distribution 49

7.4 Transmission through the Pumping Stages . . . 51
7.4.1 Experimental Set-Up . . . 51
7.4.2 Angular Acceptance . . . 52
7.4.3 Calculated Transmission . . . 53
7.5 DRAGON Ion Optics . . . 55
7.5.1 Experimental Set-Up . . . 55
7.5.2 GIOS Predictions & Comparison with Reality . . . 55

8 Studies of Nuclear Reactions with Stable Beam 61
8.1 DRAGON Tuning Procedure . . . 62
8.2 Data Normalization and Systematic Errors . . . 63
8.3 The $^{20}Ne(p,\gamma)^{21}Na$ Reaction at $E_{cm} = 1112.6$ keV . . . 64
8.4 The $^{21}Ne(p,\gamma)^{22}Na$ Reaction at $E_{cm} = 258.6$ keV . . . 71
8.5 The $^{21}Ne(p,\gamma)^{22}Na$ Reaction at $E_{cm} = 731.5$ keV . . . 76
8.6 The $^{24}Mg(p,\gamma)^{25}Al$ Reaction at $E_{cm} = 214.0$ keV . . . 83
8.7 The $^{24}Mg(p,\gamma)^{25}Al$ Reaction at $E_{cm} = 402.2$ keV . . . 89
8.8 The $^{24}Mg(p,\gamma)^{25}Al$ Reaction at $E_{cm} = 790.4$ keV . . . 93
8.9 Results . . . 96
8.9.1 Comparison of the Measured Resonance Strengths . . . 96
8.9.2 Agreement with the Energy Calibration . . . 98
8.9.3 Energy Loss compared to the SRIM Data Base . . . 99
8.9.4 Beam Suppression . . . 101
8.9.5 Charge State Distribution . . . 103
8.9.6 BGO efficiency . . . 106

9 Measurement of $^{21}Na(p,\gamma)^{22}Mg$ at $E_{cm} = 821$ keV 107
9.1 Experimental Procedure . . . 107
9.2 Exploring the New Resonance . . . 110
9.3 Gamma Branching Ratios . . . 115
9.4 Influence on Nuclear Astrophysics . . . 118

10 Discussion and Conclusion 120

A List of Run Numbers 121

List of Figures

1 Artist's picture of a nova environment . . . 3
2 Graphical summary of the NeNa cycle . . . 5
3 Photograph of a meteoritic grain . . . 5
4 Path of the nucleosynthesis of an X-ray burst, by courtesy of Hendrik Schatz [SCH02] . . . 7
5 Gamow peak . . . 10
6 Breit-Wigner curve . . . 13
7 Thick target yield curve . . . 15
8 Recoil opening cone due to de-excitation of the compound nucleus . . . 16
9 ^{22}Mg nucleus, showing the excitation energies [BAT01] and presumed spin assignments with Gamow windows indicated for several temperatures . . . 19
10 Layout of the ISAC hall . . . 20
11 ISAC accelerators . . . 21
12 Perspective layout of the DRAGON set-up . . . 22
13 Gas target cell . . . 23
14 Schematic plot of the differential pumping system . . . 24
15 Layout of the pumping tubes . . . 24
16 Layout of the BGO detector array . . . 25
17 Dragon Layout . . . 27
18 Photograph of the DRAGON Facility . . . 28
19 Schematic view of a double sided silicon strip detector . . . 31
20 Block diagram of the data acquisition electronics . . . 32
21 Modified version of the BGO detector array consisting of 13 BGO crystals along the target box . . . 34
22 Set-up of the movable BGO detector shielded by lead bricks . . . 35
23 Typical gamma energy spectrum for $^1H(^{15}N,\alpha\gamma)^{12}C$ at $E_{cm} = 843$ and 404 keV . . . 36
24 Scans of the 426 keV resonance, with and without energy shift correction . 37
25 Position shift of the low energy resonance monitored with the z-mask feature 37
26 Typical spectrum of the time correlation between elastic monitor and rf-signal 38
27 Linear relation of the position of gamma ray activity within the target and the position of the peak in the elastic monitor time spectrum . . . 38
28 Energy calibration of MD_1 . . . 43
29 Typical gamma energy spectrum for $^1H(^{15}N,\alpha\gamma)^{12}C$ at 1.45 MeV/u . . . 45
30 Correlation of the background peak with the position of the detector . . . 46
31 Gas target density profile . . . 47
32 Measurement of total target thickness . . . 48
33 Sketch of the 3x3 mm^2 aperture and the deflection of the outgoing beam . . 51
34 Transmission through the pumping tubes of the gas target . . . 52
35 Projection of gamma ray momentum onto x and y axis . . . 54

36 Separation of recoils and beam ions in projection onto the xy-plane at the mass slits for the improved and the calculated tune 57
37 Focus properties of the DRAGON Recoil Separator at the charge slits for the old, the improved and the calculated tune 58
38 Focus properties of the DRAGON Recoil Separator at the mass slits for the old, the improved and the calculated tune 59
39 Focus properties of the DRAGON Recoil Separator at the final slits for the old, the improved and the calculated tune 60
40 Recoil energy spectra in singles and coincidence mode for $^{20}Ne(p,\gamma)^{21}Na$ at E_{cm} = 1112.6 keV 64
41 Gamma energy spectrum in singles and coincidence mode with the position distribution of gamma ray events within the target, the elastic energy spectrum and the count rate of the "good" elastics above background for a typical run of $^{20}Ne(p,\gamma)^{21}Na$ at E_{cm} = 1112.6 keV 65
42 Decay scheme for the ^{21}Na excited state at E_x = 3.54 MeV. 66
43 Energy loss measured for the $^{20}Ne(p,\gamma)^{21}Na$ recoils at E_{cm} = 1112.6 keV . 67
44 Full excitation curve of the $^{20}Ne(p,\gamma)^{21}Na$ reaction at E_{cm} = 1112.6 keV . 68
45 Beam energy versus the position of the resonance (z-mask) for $^{20}Ne(p,\gamma)^{21}Na$ at E_{cm} = 1112.6 keV 70
46 BGO efficiency along the beam axis for 3.5 MeV gammas 70
47 Recoil energy spectra in singles and coincidence mode for $^{21}Ne(p,\gamma)^{22}Na$ at E_{cm} = 258.6 keV 71
48 Gamma energy spectrum in singles and coincidence mode with the position distribution of gamma ray events within the target, the elastic energy spectrum and the position distribution of recoils in the DSSSD for a typical run of $^{21}Ne(p,\gamma)^{22}Na$ at E_{cm} = 258.6 keV 72
49 Fit to a typical recoil energy spectrum for $^{21}Ne(p,\gamma)^{22}Na$ at E_{cm} = 258.6 keV 73
50 Decay scheme for the ^{22}Na excited state at E_x = 6.998 MeV. 74
51 Observed resonance yield for $^{21}Ne(p,\gamma)^{22}Na$ at E_{cm}= 258.6 keV 75
52 Recoil energy spectrum in singles and coincidence mode for $^{21}Ne(p,\gamma)^{22}Na$ at E_{cm} = 731.5 keV 76
53 Gamma energy spectrum in singles and coincidence mode with the z-mask gamma distribution, the elastic energy spectrum and the correlation of ion detection time in the end detector with the rf-phase of the accelerator for a typical run of $^{21}Ne(p,\gamma)^{22}Na$ at E_{cm} = 731.5 keV 77
54 Yield for $^{21}Ne(p,\gamma)^{22}Na$ resonance at E_{cm} = 731.5 keV 79
55 Decay scheme for the ^{22}Na excited state at E_x = 7.47 MeV. 80
56 Coincidence recoils versus γ-energy and projection to the γ-energy axis for $^{21}Ne(p,\gamma)$ at E_{cm} = 731.5 keV. 81
57 Efficiency of BGO array versus position for the $^{21}Ne(p,\gamma)^{22}Na$ resonance at E_{cm} = 731.5 keV 82

58 Beam energy versus resonance position within target for $^{21}Ne(p,\gamma)^{22}Na$ at $E_{cm} = 731.5$ keV 82
59 Recoil energy spectra in singles and coincidence mode for the $^{24}Mg(p,\gamma)^{25}Al$ reaction at $E_{cm} = 214.0$ keV 83
60 Gamma energy spectrum in singles and coincidence mode with a two dimensional time-of flight graph showing γ versus heavy ion time and heavy ion versus γ time, a two dimensional plot showing the relation of γ and heavy ion energy as well as its projection on the y(γ energy)-axis for a typical run of $^{24}Mg(p,\gamma)^{25}Al$ at $E_{cm} = 214.0$ keV 84
61 Recoil energy spectra in singles and coincidence mode with various cuts on the t-o-f and γ-energy for $^{24}Mg(p,\gamma)^{25}Al$ at $E_{cm} = 214.0$ keV 85
62 Gamma energy spectrum for the highest energy gamma detected in coincidence, compared to the sum of all singles gammas for the $^{24}Mg(p,\gamma)^{25}Al$ reaction at $E_{cm} = 214.0$ keV, summed over all runs 86
63 Decay scheme for the ^{25}Al excited state at $E_x = 2.49$ MeV. 87
64 Yield curve measured for the $^{24}Mg(p,\gamma)^{25}Al$ resonance at $E_{cm} = 214.0$ keV 88
65 Recoil energy spectrum in singles and coincidence mode for $^{24}Mg(p,\gamma)^{25}Al$ at $E_{cm} = 402.2$ keV 89
66 Gamma energy spectrum in singles and coincidence mode with a two dimensional graph showing γ versus heavy ion energy, the spectrum of the elastically scattered protons and their rate versus run time for a typical run of $^{24}Mg(p,\gamma)^{25}Al$ at $E_{cm} = 402.2$ keV 90
67 Decay scheme for the ^{25}Al excited state at $E_x = 2.67$ MeV. 91
68 Yield measured at various energies for $^{24}Mg(p,\gamma)^{25}Al$ at $E_{cm} = 402.2$ keV . 92
69 Recoil energy spectrum in singles mode for $^{24}Mg(p,\gamma)^{25}Al$ at E_{cm} =790.4 keV 93
70 Recoil time versus rf-signal peak and position distribution on the DSSSD, as well as the elastically scattered proton energy and rate for a typical run of $^{24}Mg(p,\gamma)^{25}Al$ at $E_{cm} = 790.4$ keV 94
71 Yield measured at various energies for $^{24}Mg(p,\gamma)^{25}Al$ at $E_{cm} = 790.4$ keV . 95
72 Agreement of resonance strengths measured with DRAGON compared to the literature values 97
73 Comparison of measured resonance energies to the literature values 98
74 Comparison of measured energy losses with predictions of the SRIM code . 100
75 Leaky beam suppression for various stable beam reactions 102
76 Gaussian fits to the measured charge state distributions 104
77 Comparison of predicted (blue) to measured charge state distribution (purple) 105
78 Energy loss in the target for ^{21}Na ions at $E_{lab} \approx 840$ keV/u 108
79 Focus properties of the DRAGON recoil separator at the charge, mass and final slits calculated for a realistic $^{21}Na(p,\gamma)^{22}Mg$ tune at $E_{cm} = 821$ keV . 109
80 Recoil energy spectrum with and without gamma coincidence requirements for $^{21}Na(p,\gamma)^{22}Mg$ at $E_{cm} = 821$ keV 110

81 Elastically scattered proton energy spectrum, rates of elastically scattered protons and detected betas over the run time, recoil position in the DSSSD and recoil versus related gamma energy for a typical run of $^{21}Na(p,\gamma)^{22}Mg$ at E_{cm} = 821 keV 111
82 Resonance in the elastic scattering channel $^{21}Na(p,p')$ at E_{cm} = 821 keV . 112
83 Relation of the current on FC4 to the rate in the beta monitor 113
84 Excitation curve of the $^{21}Na(p,\gamma)^{22}Mg$ reaction at E_{cm} = 821 keV 114
85 Comparison of beam suppression for stable and unstable beam 115
86 Energy spectrum of the detected gammas with and without coincidence requirements, summed over several runs of $^{21}Na(p,\gamma)^{22}Mg$ at E_{cm} = 821 keV 116
87 Decay scheme of the ^{22}Mg excited state at E_x = 6.23 MeV. 117
88 Fit to the coincidence gamma energy spectrum for $^{21}Na(p,\gamma)^{22}Mg$ at E_{cm} = 821 keV 118
89 Plot of ^{21}Na lifetime versus temperature under X-ray burst conditions . . . 119

List of Tables

1 Design of the Magnetic & Electric Benders 29
2 First Order Matrix Elements 29
3 Contributions to Total Beam Energy Spread, without Last HEBT Buncher 40
4 Magnetic Constant c_{mag} 42
5 Target Profile Fitting Parameters 47
6 Fitting Parameters for Angular Transmission 52
7 Measured Ion Optics Matrix Elements Compared to Calculated Values . . . 56
8 Stable Beam Reactions Measured at DRAGON 61
9 Charge State Distribution of ^{21}Na recoils at E_{lab} 1100 keV/u 67
10 Fitting Parameters of the $^{20}Ne(p,\gamma)^{21}Na$ Yield at E_{cm} = 1112.6 keV . . . 68
11 Charge State Distribution for ^{22}Na recoils at E_{lab} 730 keV/u 78
12 Fitting Parameters for the $^{24}Mg(p,\gamma)^{25}Al$ Yield at E_{cm} = 214 keV 88
13 Charge State Distribution for the ^{25}Al recoils at E_{lab} = 400 keV/u 91
14 Charge State Distribution for the ^{25}Al recoils at E_{lab} = 780 keV/u 95
15 Measured Resonance Strength 97
16 Measured Resonance Energies 99
17 Measured Energy Loss 99
18 Measured Beam Suppression 101
19 Fit to the Measured Charge State Distributions 103
20 Deviation from Calculated Charge State Probability 105
21 Parameters of the $^{21}Na(p,\gamma)^{22}Mg$ Reaction 107
22 Charge State Distribution of the ^{22}Mg recoils at E_{lab} 820 keV/u 113
23 Branching Ratios for ^{22}Mg at E_x = 6323 keV 117
24 Preliminary DRAGON Results on $^{21}Na(p,\gamma)^{22}Mg$ Resonances Below E_{cm} = 821 keV [BIS02] 119
25 List of Run Numbers 121

Abstract

The "Detector of Recoils And Gammas Of Nuclear reactions", DRAGON, is a new facility, especially designed to measure absolute cross sections of radiative proton- and alpha-capture reactions on radioactive nuclei of astrophysical interest. Located at the TRIUMF-ISAC radioactive ion beams laboratory in Vancouver, Canada, the DRAGON performs studies on reactions in inverse kinematics with ion beams in the mass range of 6 to 30 amu impinging on a gas target at energies of 0.15 to 1.5 MeV/u. A BGO detector array to tag the prompt gamma radiation emitted in a reaction surrounds the target, followed by a recoil mass separator and a double sided silicon strip detector which measures position and energy of the recoil at the final focus. Beam suppression of the order of $10^{11} - 10^{15}$ is needed to fully separate the radioactive beam ions from the much rarer reaction products. Systematic studies of various configurations using stable beams along with measurements of well-known resonance reactions were completed for the commissioning of the complete facility and the energy calibration of the new ISAC radioactive beam accelerator. Additionally, the first results of the scientific program, that has been launched with a study on the $^{21}Na(p,\gamma)^{22}Mg$ reaction at $E_{cm} \approx 821$ keV, will be presented.

Abstrakt

Der DRAGON, Detektor für Rückstoßkerne und Gammas von Nuklearen Reaktionen, ist ein neues Experiment, das speziell zur Bestimmung von Wirkungsquerschnitten von Proton- und Alpha- Einfangreaktionen konzipiert wurde. Der Aufbau befindet sich am TRIUMF ISAC Labor für radioaktive Ionenstrahlen in Vancouver, Canada. Hier werden astrophysikalisch relevante Reaktionen in inverser Kinematik gemessen, mit Ionenstrahlen in der Massenregion von 6 bis 30 amu und Energien von 0.15 bis zu 1.5 MeV/u. Die beschleunigten Ionen treffen auf ein Gastarget, das von BGO Detektoren, zur Beobachtung der unverzögerten Reaktionsgammas, umgeben ist. Dem Target folgt ein Rückstoß-Massenseparator und, an dessen Ende, ein doppelseitiger Silizium-Streifen Detektor, um Position und Energie der gefilterten Reaktionsprodukte zu bestimmen. Dabei ist eine Strahlunterdrückung in der Grössenordnung von $10^{11} - 10^{15}$ erforderlich, um die wenigen Rückstoßkerne vollständig von den wesentlich intensiveren Strahlionen zu trennen.
Um die Eigenschaften des gesamten experimentellen Aufbaus zu testen und die Energien des neuen ISAC Beschleunigers zu kalibrieren, wurden systematische Untersuchungen der verschiedenen Konfigurationen mit stabilen Ionenstrahlen neben vollständigen Messungen bekannter Reaktionen durchgeführt. Zusätzlich werden in dieser Arbeit die ersten Ergebnisse des astrophysikalischen Programms präsentiert, das kürzlich mit der Messung der $^{21}Na(p,\gamma)^{22}Mg$ Reaktion bei $E_{cm} \approx 821$ keV gestartet wurde.

1 Motivation for the Present Work

Observations and theoretical predictions have shown that proton and alpha capture reactions on medium mass nuclei play an important role in the nucleosynthesis of the elements. In explosive environments such as X-ray bursts or novae, besides stable isotopes, also radioactive nuclei participate in the nuclear network, since their reaction likelihoods become comparable to their beta-decay probabilities. Initially started by the production of helium from hydrogen, this nucleosynthesis network may extend up into the heavy element region, if temperatures are sufficiently high. According to present models, several key reactions at the beginning of the burst seem to determine its further evolution significantly. Therefore, better knowledge about their reaction rates will lead to more accurate models concerning stellar evolution and nucleosynthesis.

The DRAGON experiment at the TRIUMF-ISAC radioactive beams facility was carefully designed to match the requirements of the intended astrophysical program, namely, the study of the resonance strength of certain important proton- and alpha-capture reactions involving radioactive reactants. These key reactions will be measured in inverse kinematics via the detection of the recoiling reaction product. Due to de-excitation of the populated resonance state by gamma emission, the reaction recoil leaves the target within a broadened opening angle. A crucial task is the sufficient separation of the recoiling nucleus from the more intense initial beam ions, which leave the target with roughly the same momentum, but at slightly higher energies and smaller angles. Monte Carlo based simulations had been performed to guarantee full acceptance of the recoil cone, suppression of the beam ions, and a baseline of understanding for the evaluation of the reaction data.

Nevertheless, commissioning studies are essential to confirm actual operational characteristics. Therefore, a set of tests were proposed and performed. Among them the parameters of the gas target were determined and the ion optics of the recoil separator were evaluated with stable beams. In addition the DRAGON magnets were calibrated to measure the energy of the incoming beam. Finally, tests with well known stable beam reactions were performed to provide an understanding of the overall detection efficiency of the complete system. In the framwork of this thesis, the DRAGON experiment will be presented and the commissioning program explained, performed, and analyzed, step by step.

Though the present work will focus on the commissioning of the DRAGON facility, the scientific aspects should not be forgotten. To put the importance of the commissioning work into perspective, the astrophysical background of the scientific program will be discussed briefly. This thesis will be completed by the study of the resonance in $^{21}Na(p,\gamma)^{22}Mg$ at $E_{cm} = 821$ keV. The parameters of this resonance had, up to now, only been inferred from indirect experiments and theoretical considerations. It presents the first reaction studied at the DRAGON facility involving a radioactive ion beam and the start of the astrophysical program.

2 Astrophysical Interest in the DRAGON Experiment

Over the past 75 years nuclear astrophysics has opened a new path in one of the oldest sciences on Earth. Once the connection between the stellar light emission and nuclear fusion processes was found, sophisticated models were developed according to which the origin of many of the astronomical observations in far away galaxies could be explained just as well as the isotopic composition of chemical elements on Earth. The interaction of observation, theory and experiment lead to complex networks that, today, allow to relate cross sections of microscopic processes to macroscopic phenomena.

According to present understanding, Big Bang nucleosynthesis produced only very light elements such as hydrogen, helium and lithium, while the majority of the elements was formed through nuclear reactions inside stars [BUR57]. Stars generate their energy through nuclear fusion reactions. At the end of a stellar life, some of these synthesized elements being ejected back into space serve as the seeds out of which new stars and planets evolve. Several stages during stellar evolution may be distinguished. For a main sequence star in the Hertzsprung-Russel diagram, the energy production starts with quiescent nuclear burning where the pp-chain and CNO cycle act as the main source of energy. The evolution carries on to violent sites, when explosive nucleosynthesis under extreme conditions leads to a thermonuclear runaway, such as in novae or X-ray bursts. Here, degenerate matter conditions, hot temperatures and densities, in which the decay of radioactive nuclei may be bypassed by fast proton- and alpha-capture reactions, push the nucleosynthesis out of the valley of stability. In such a scenario a significant amount of the energy is generated by catalyst cycles such as the hot CNO or the NeNa cycle. With higher temperatures the rapid-proton capture (rp-) process takes over the energy production and synthesizes elements up to the SnSbTe region.

2.1 Scientific Program of the DRAGON Experiment

In the past, laboratory studies in nuclear astrophysics have been largely performed using stable nuclei in order to supply data for nuclear reaction networks mostly describing quiescent burning stages. Yet, a complete interpretation of the observation requires information on explosive sites, thus knowledge of reactions involving radioactive nuclei. The use of light proton, deuterium or helium beams on solid or gaseous radioactive targets can only provide direct data for fairly long-lived species. In order to measure reactions with nuclei having half lifes of the order of seconds, experiments have to employ radioactive ion beams impinging on light, stable targets in inverse kinematics.

The ISAC facility [LAX01] was designed to provide high intensity, accelerated radioactive ion beams. With such beams, reactions of astrophysical relevance in explosive nucleosynthesis can be measured with the DRAGON facility. Experiments planned for the near

future include reactions determining the time scale of a nucleosynthesis network; bottleneck reactions such as the direct capture of $^{13}N(p,\gamma)^{14}O$ or $^{15}O(\alpha,\gamma)^{19}Ne$ as a possible break-out paths from the hot CNO cycle; $^{19}Ne(p,\gamma)^{20}Na$ leading to the NeNa-Cycle; as well as $^{23}Mg(p,\gamma)^{24}Al$ and $^{25}Al(p,\gamma)^{26}Si$ connecting the NeNa-cycle to the subsequent MgAl-cycle and on to higher masses. The goal of the DRAGON facility is to measure absolute cross sections or resonance strengths with an accuracy better than 20%.

The astrophysical program has been launched with studies on the $^{21}Na(p,\gamma)^{22}Mg$ cross section. It was initially chosen, since the decay product of ^{22}Mg produces an important astronomical observable: the 1.28 MeV gamma originating from the decay of ^{22}Na, the daughter nucleus of ^{22}Mg. Measurements of resonance parameters in the $^{21}Na(p,\gamma)^{22}Mg$ reaction will help to constrain production mechanisms for ^{22}Na in a wide variety of astrophysical scenarios.

2.2 Oxygen-Neon-Novae

One site for explosive nucleosynthesis are so called oxygen-neon-novae which represent about 30% of all observed novae. In the present understanding, novae are a stage in the evolution of a close binary system [STA89]. In the special case of ONe-novae it is believed that the binary system consists of a white dwarf star that already underwent carbon burning in its prior life [WEI90]. Thus, its surface composition is enriched in ^{16}O, ^{20}Ne and ^{24}Mg, whereas its companion is still in a stage of quiescent burning, surrounded by a thick shell of mostly hydrogen. During its evolution, the main sequence or red giant star can expand so that its outer layers fill the Roche lobe. From this point of equipotential, the material may be captured into the gravitational field of the white dwarf forming an accretion disk through which the hydrogen rich material slowly accumulates on the ONe surface.

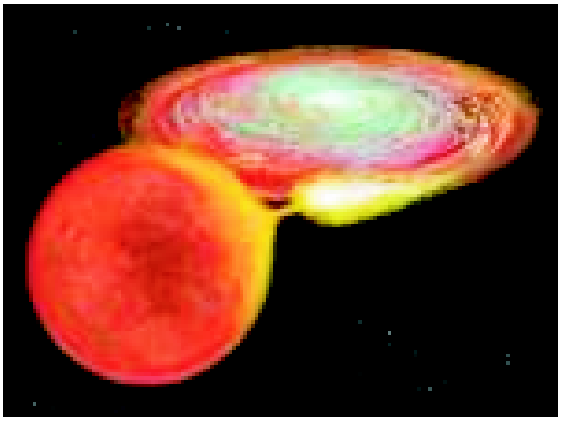

Figure 1: Artist's picture of a nova environment

Dredge-up of the underlaying white dwarf material allows mixing of the heavier isotopes with the hydrogen envelope [GLA97]. Once a critical mass has been accreted and the temperature governed by the gravitational field is high enough to start nuclear fusion, proton capture will ignite. The conditions during the initial phase of the nucleosynthesis are strongly determined by the mass of the underlying white dwarf and the accretion rate from the near main sequence companion. If cooling is adequate, ignition can start under degenerate conditions. These are further enhanced by the heat produced in the commencing pp-chain, followed by the CNO cycle. Proton capture on the oxygen, neon, and magnesium seed nuclei will produce additional heat. Recent models predict that the ^{20}Ne and ^{24}Mg seeds will contribute to the thermonuclear runaway through catalytical cycles producing a significant abundance of ^{22}Na and ^{26}Al.
The conditions for classical novae are generally believed to cover temperatures up 0.1 to 0.4 GK and densities in the area of $10^3 g/cm^3$ [STA89], which are too low for a breakout into the rapid proton capture region. Typical time scales are of the order of several minutes. Once the degeneracy is lifted, the expansion of the burning shell is initiated. Convective zones may form and, within time scales of the order of 100 sec, may transport material to the outside, among it long-lived β^+ unstable nuclei, possibly also ^{22}Na.

In the modelling of nucleosynthesis in nova explosions, important parameters such as temperature and density to describe the hydrodynamics are often unknown. To constrain these models, observables like specific gamma-ray emitters are needed, such as ^{22}Na. ^{22}Na has a half life of 2.6 years, β^+-decaying to a short lived excited state in ^{22}Ne, that de-excites by emission of a 1.275 MeV gamma. Potentially, those gamma rays can be observed by new space based telescopes. In recent years the COMPTEL Gamma Ray Observatory provided upper limits for the ^{22}Na abundance in novae Her1991 and Cyg1992 that were well below the expected value [IYU95]. INTEGRAL, launched in October 2002, will continue the studies. Meanwhile, the study of the involved nuclear reactions has to proceed to reduce uncertainties in the theoretical models.

Nucleosynthesis via the NeNa cycle (fig. 2) is not yet fully understood. According to recent models, a ^{20}Ne seed captures a proton and forms ^{21}Na, which decays via β^+ to ^{21}Ne. Two subsequent radiative proton captures lead to ^{23}Mg. From here, if the temperature is high enough, the nucleosynthesis can jump into the MgAl cycle. Alternatively, at lower temperatures, a β^+ decay followed by a (p, α) reaction feeds ^{23}Mg back into the cycle. Later within the nova explosion, when the temperature has risen, the β^+ decay of ^{21}Na can be bypassed by another radiative proton capture forming ^{22}Mg. A very low Q-value of only 125 keV hampers the production of ^{23}Al, which photo-disintegrates immediately back to ^{22}Mg. ^{22}Mg decays with a half life of 3.86 s to ^{22}Na. Recent models predict that the uncertainty in the final amount of ^{22}Na in the expelled material is determined mainly by the reaction rate of $^{21}Na(p,\gamma)^{22}Mg$ [JOS99] and [ILI02]. Surprisingly, when the rate is reduced by a factor of 100 in the simulation, the amount of ^{22}Na in the expelled material is increased by a factor of 2 to 3. This can be understood, since with

decreased probability of $^{21}Na(p,\gamma)^{22}Mg$ the competing path $^{21}Na(\beta^+)^{21}Ne(p,\gamma)^{22}Na$ is favored. Thus, the ^{22}Na production is delayed. Then, once the envelope is expanding and cooling, the destruction of ^{22}Na via subsequent fusion is hampered. Consequently, a major fraction of ^{22}Na survives the explosion [JOS99]. The production of ^{26}Al is governed by $^{24}Mg(p,\gamma)^{25}Al(\beta^+)^{25}Mg(p,\gamma)^{26}Al$, with the supply of ^{24}Mg maintained via $^{23}Mg(p,\gamma)^{24}Al(\beta^+)^{24}Mg$.

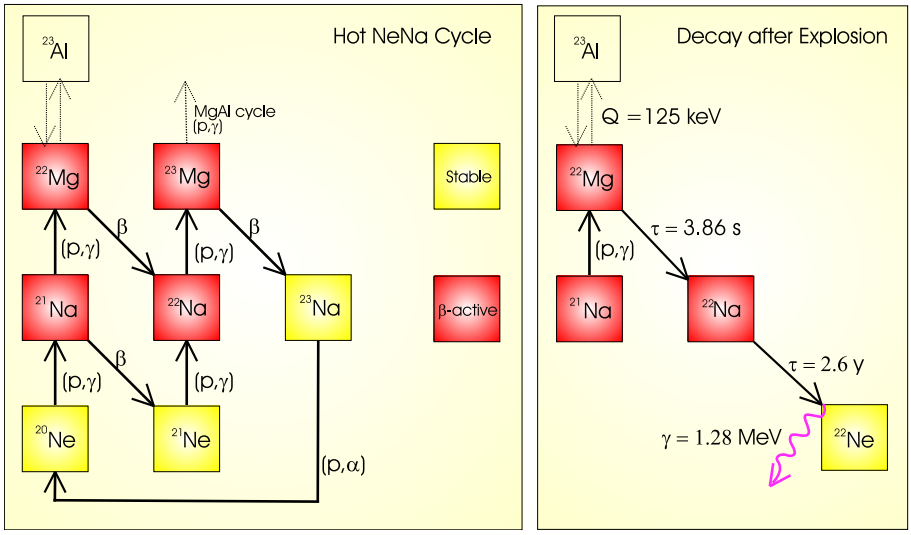

Figure 2: Graphical summary of the NeNa cycle

Once the production and destruction mechanisms for ^{22}Na are sufficiently known, carbonaceous meteoritic grains (fig. 3), that contain enrichments compared to the solar abundance of its daughter product ^{22}Ne, could possibly be linked to nova sites. Thus, isotopic abundances found in such grains could be related to their origin [ZIN95] and [AMA01] and put further constraints on the theoretical models.

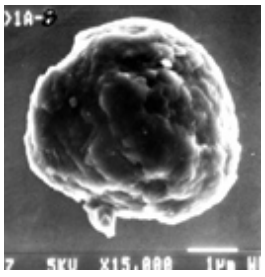

Figure 3: Photograph of a meteoritic grain

2.3 Type-I X-Ray Bursts

According to present understanding, the source of a type-I X-ray burst is a thermonuclear runaway on the surface of a neutron star in a close binary system. As in novae, the neutron star accumulates hydrogen rich material from the main sequence or red giant companion on its surface. Here, radiative proton captures on the heavier seeds, that have not been depleted by spallation, cause nucleosynthesis through a network of nuclear reactions. Though X-ray bursts are a frequent phenomenon within our galaxy, the nucleosynthesis is not completely understood. Assumptions for the hydrogen accretion rate vary between 0.1 - $1{\cdot}10^{-9}$ solar masses per year. The higher gravitational field on the degenerate neutron star material allows densities of up to $10^6 g/cm^3$ with temperatures peaking at 2 to 3 GK before the degeneracy is lifted. In this environment, the nucleosynthesis is ignited by the pp-chain and subsequently the CNO cycle. It is assumed that the first phase of the burst ends with the conversion of ^{12}C into ^{14}O in the hot CNO cycle, which depends sensitively on the rate of $^{13}N(p,\gamma)^{14}O$. Consequently significant amounts of ^{14}O, ^{15}O and ^{18}Ne are left at so called waiting points. Around 0.24 GK the triple-α-process, converting three ^4He nuclei into ^{12}C, is starting the second phase of the burst. Thus, newly available ^{12}C is produced, while subsequent α-capture depletes the waiting point nuclei. The nucleosynthesis evolves through rapid proton capture (rp-) and (α,γ) reactions, the so-called αp-process. It reaches temperatures around 2.5 GK and quickly leaves the bounds of stability in a thermonuclear runaway that follows the proton drip line up to ^{56}Ni. Here, nuclear fusion terminates. As a result the energy production drops quickly, while most of the initial He accumulates in the ^{56}Ni waiting point. Further nucleosynthesis up to the end point around tin, antimony and tellurium is probably determined by the rates of $^{56}Ni(p,\gamma)^{57}Cu$ and $^{57}Cu(p,\gamma)^{58}Zn$. Typical time scales for X-ray bursts are of the order of 10 to 100 seconds. [WIE98]

As figure 4 demonstrates, current network calculations imply that the nucleosynthesis in an X-ray burst goes through the $^{21}Na(p,\gamma)^{22}Mg$ reaction. Because of the kinematically available energy at temperatures of 2 GK, the reaction path can go through potential resonances around $E_{cm} = 945 \pm 466$ keV. Yet, the importance of single resonances depends not only on the lifetime of ^{21}Na with respect to proton capture, but also on the β^+ decay time of the nucleus compared to the time frame of the entire burst and possibly other concurrent reaction paths.

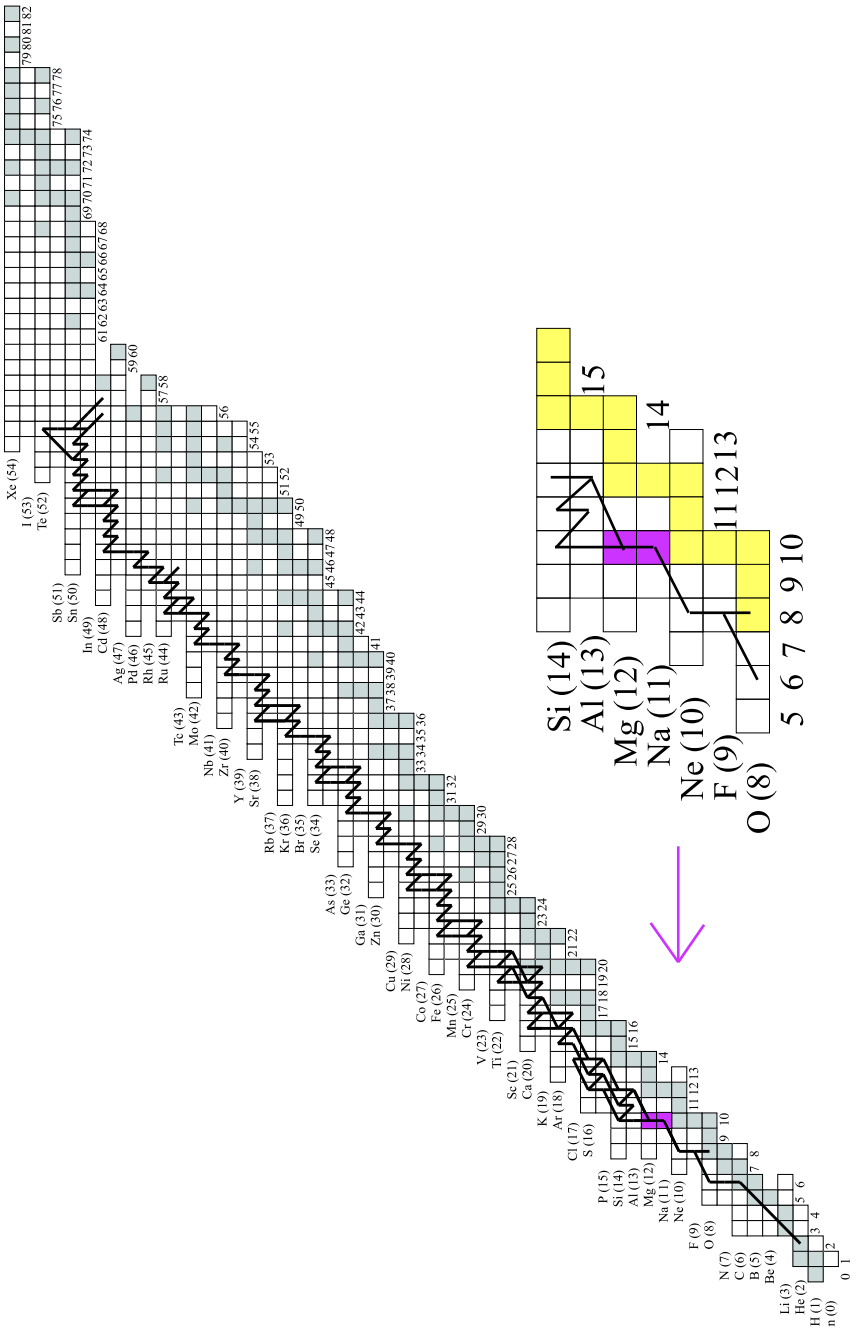

Figure 4: Path of the nucleosynthesis of an X-ray burst, by courtesy of Hendrik Schatz [SCH02]

3 Theory of Resonant Capture Reactions

In the following, all equations are based on [ROL88] and references herein.

3.1 Nuclear Cross Section

While in the classical treatment the cross section of a two body reaction is represented by the geometrical area $\sigma = \pi(r_1+r_2)^2$ of the two interacting particles, in nuclear reactions the quantum mechanical particle-wave dualism leads to a slightly different, energy dependent approach:

$$\sigma \;=\; \frac{1}{4\pi}\,\lambda^2. \tag{1}$$

Here, the cross section is proportional to the square of the de Broglie wavelength $\frac{\lambda}{2\pi}$ of the two particle system.

$$\lambda^2 \;=\; \frac{m_p + m_t}{m_p \cdot m_t}\,\frac{h^2}{2E_{cm}} \tag{2}$$

with m_p and m_t representing projectile and target mass, E_{cm} the energy in the center-of-mass frame and h the Planck constant. In experimentally more common units with E_{cm} in keV and the reduced mass $\mu = \frac{m_p m_t}{m_p+m_t}$ in amu, it follows

$$\lambda^2 \;=\; 4\pi\,\frac{656.6}{\mu \cdot E_{cm}} \quad barn. \tag{3}$$

3.2 Stellar Reaction Rate Formalism

Contrary to laboratory experiments, in a stellar environment the particles of interest show a broad energy distribution. Assuming that the stellar gas or plasma resides in thermodynamic equilibrium, this distribution for a certain temperature T can be described with the Maxwell-Boltzmann formalism. It can be shown that the distribution of the relative velocity v of any two particles also follows the same mathematical description:

$$\Phi(v) \;=\; 4\pi v^2\,(\frac{\mu}{2\pi kT})^{\frac{3}{2}} \quad exp\,(\frac{-\mu v^2}{2kT}), \tag{4}$$

where k is the Boltzmann constant.
Consequently the cross section has to be folded with the energy or velocity distribution of the reacting particles, so that the stellar reaction rate r for two particles with a number density N_i is

$$r \;=\; N_1 N_2 < \sigma v > (1+\delta_{12})^{-1} \tag{5}$$

with

$$< \sigma v > = \int_0^\infty \Phi(v)\, v\, \sigma(v)\, dv. \tag{6}$$

Inserting formula 4 into 6 gives

$$< \sigma v > = \sqrt{\frac{8}{\pi\mu}}\, \frac{1}{(kT)^{3/2}} \quad \int_0^\infty \sigma(E_{cm})\, E_{cm}\, exp\,(-\frac{E_{cm}}{kT})\, dE. \tag{7}$$

The Maxwell-Boltzmann formalism can also be applied on the surface of white dwarfs and neutron stars. Although the underlying matter is degenerate, it is assumed that nuclei on the surface form a very dense, but normal gas.

In stellar environments, exothermic (energy releasing) reactions dominate the network. However, their rate is hampered by the repulsive Coulomb force E_C of the two positively charged interacting nuclei with atomic numbers Z_1 and Z_2 at a distance r.

$$E_C(r) \;=\; \frac{Z_1 Z_2\, e^2}{r} \tag{8}$$

Here, e^2 is $1.44 \cdot 10^{-10}$ keV·cm and $r \;=\; r_1 + r_2$ with $r_i \;\approx\; 1.3 \cdot 10^{-13} A^{1/3}$ cm. Although the Coulomb barrier is partially shielded by the surrounding electron cloud, in the case of $^{21}Na(p,\gamma)$, the nuclei still need to overcome a potential of the order of 3 MeV. The required kinetic energy is equal to a temperature of 34 GK or 34 T_9 which is a factor of 10 times higher than believed to be reasonable for X-ray bursts. Clearly, within the Maxwell-Boltzmann distribution, a few particles lying in the high energy tail might reach enough energy, even at lower stellar temperatures. Yet, in order to account for the observed rates, another factor has to be considered which is quantum mechanical tunnelling [GAM28]. Solving the Schrödinger equation for the Coulomb barrier potential leads to the tunnelling probability P that, for the $E_{cm} \ll E_C$ approximation for s-waves, can be written as

$$P \;=\; exp\,(-2\pi\eta) \tag{9}$$

where the Sommerfeld parameter η for E_{cm} in keV and μ in amu is defined as

$$\eta \;=\; 31.29\, Z_1 Z_2 \sqrt{\frac{\mu}{E_{cm}}}. \tag{10}$$

Then the stellar cross section can be expressed as the product of the penetration probability, a factor $1/E$ originating from the energy dependence of the de Broglie wave length, and the astrophysical S-factor $S(E)$ that shall describe all nuclear effects. Thus, the latter varies only slowly with the energy for a non-resonant reaction.

$$\sigma(E) \;=\; \frac{1}{E_{cm}} \quad exp\,(-2\pi\eta)\, S(E) \tag{11}$$

For non-resonant reactions, where $S(E)$ can be assumed constant over a wide energy range, equation 11 changes equation 7 to

$$< \sigma v >= \sqrt{\frac{8}{\pi\mu}} \frac{1}{(kT)^{3/2}} S(E_0) \quad \int_0^\infty exp\,(-\frac{E_{cm}}{kT} - \frac{b}{\sqrt{E_{cm}}}) \quad dE \tag{12}$$

and

$$b \;=\; \sqrt{2\mu} \quad 2\pi^2 \frac{e^2 Z_1 Z_2}{h}. \tag{13}$$

b^2 is referred to as the Gamow energy. Taking the first derivative, it can be shown that the cross section folded with the relative velocity of the two interacting particles reaches a peak at the energy E_0.

$$E_0 \;=\; (\frac{bkT}{2})^{\frac{2}{3}} \;=\; 1.22 \sqrt[3]{Z_1^2 Z_2^2 \mu T_6^2} \qquad keV \tag{14}$$

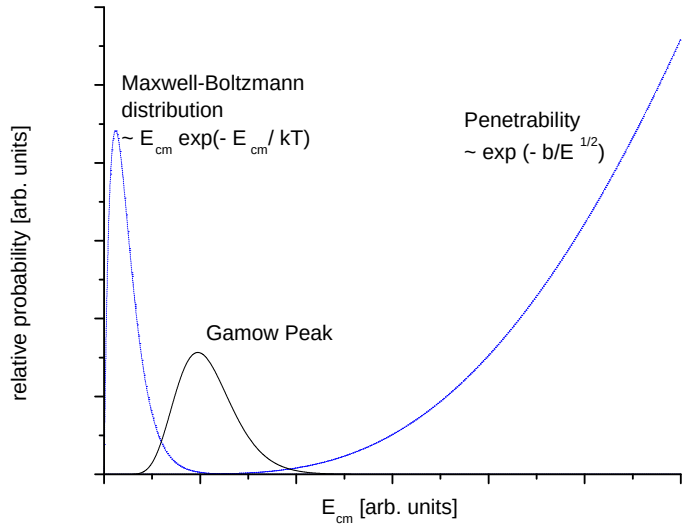

Figure 5: Gamow peak

Although the Gamow peak is strictly speaking not symmetric, the exponential term in equation 12 can be approximated by a Gaussian function. Thus, the width of the Gamow peak Δ can be expressed as

$$\Delta \;=\; \sqrt{\frac{16}{3} E_0\, kt} \;=\; 0.749(Z_1^2 Z_2^2\, \mu T_6^5)^{\frac{1}{6}} \qquad keV. \tag{15}$$

The Gamow window $E_0 \pm \frac{\Delta}{2}$ corresponds to the energy range within which most reactions in the stellar environment are likely to occur. Obviously, the energy depends on the atomic number of the interacting nuclei and shifts for heavier masses to higher temperatures, while the rate depends on the Coulomb barrier. Consequently, even with heavier nuclei present, the lightest elements with the smallest Coulomb barrier will be the most significant contributors to the stellar energy production.

Assuming a Gaussian shape of the non-resonant reaction rate the integral in equation 12 can be solved. The reaction rate is then

$$< \sigma v > = \; 7.20 \cdot 10^{-19} \; \frac{1}{\mu Z_1 Z_2} \; \varepsilon^2 \; exp(-\varepsilon) \; S(E) \quad cm^3/s \tag{16}$$

and

$$\varepsilon \; = \; 42.46 \sqrt[3]{\frac{Z_1^2 Z_2^2 \; \mu}{T_6}}. \tag{17}$$

The particle density N_j in a given environment can be calculated from its relation to the mass density ρ in g/cm^3, the mass fraction X_j and the atomic mass number A_j in amu by

$$N_j \; = \; \rho \, N_A \frac{X_j}{A_j} \quad part/cm^3. \tag{18}$$

N_A is the Avogadro constant. Then the lifetime of an element i towards destruction by a nucleon j in this environment is

$$\tau_j(i) \; = \; \frac{1}{N_j \; < \sigma v >}. \tag{19}$$

3.3 Narrow Isolated Resonances

At explosive sites such as novae, the nucleosynthesis often involves resonant reactions, where two particles interact through a compound nucleus. Excited states E_x in the compound nucleus may enhance the cross section at certain well defined relative energies. If the relative energy E_{cm} of the reacting nuclei plus their combined mass excess Q is equal to an excitation energy E_x

$$E_x \; = \; Q + E_{cm} \; = \; Q + E_R \tag{20}$$

the reaction may occur with a strength increased by several orders of magnitude. Then the relative energy E_{cm} is refereed to as the resonance energy E_R. The previous geometrical picture of the cross section has to be revised for the special case of resonant reactions.

The reaction cross section for resonant reactions depends strongly on the characteristics of the level in the compound nucleus such as the excitation energy, the level width and the relation to neighboring states. All reactions discussed in the present work are sufficiently narrow so that they may be considered isolated, which means that they overlap neither with each other nor with the ground state. Therefore, they can be treated separately.
Whether resonant behavior can be observed for a given reaction channel depends on quantum mechanical selection rules. For angular momentum conservation, the angular momentum J of the excited state in the compound nucleus has to be equal to the vector sum of the incoming spins J_p and J_t of projectile and target, plus their relative orbital momentum l. Parity conservation requires that the product of the parities in the incoming channel form the parity of the excited state:

$$J \;=\; J_p \pm J_t \pm l \tag{21}$$

and

$$\pi(J) \;=\; \pi(J_p) \cdot \pi(J_t) \cdot (-1)^l. \tag{22}$$

When a resonance may occur, the Breit-Wigner formalism supplies a semi-classical approach to describe the resonant behavior of a two particle interaction. The cross section, depending strongly on the energy, can then be regarded as

$$\sigma_{BW}(E) \;=\; \frac{\lambda^2}{4\pi} \quad \omega\tilde{\gamma}. \tag{23}$$

In addition to the previous description in equation 1, the statistical factor ω accounts for the number of possible states in the compound nucleus compared to the number of states in the entrance channel. These are equal to the number of magnetic sub-states $(2J+1)$, for any given state with spin J. Thus, ω is:

$$\omega \;=\; \frac{(2J+1)}{(2J_p+1)(2J_t+1)}\,(1+\delta_{pt}). \tag{24}$$

The factor $(1+\delta_{pt})$ accounts for an increasing cross section by a factor 2, if two identical particles interact.

The resonant behavior is treated like a harmonic oscillator with a dissipative force that allows the oscillator to swing within an energy range of $E_{cm} - E_R$. The oscillator strength is determined by the partial widths of the incoming and outgoing channel Γ_{in} and Γ_{out}. The half maximum of the resonance is the total width Γ_{tot} of the excited state in the compound nucleus. For a narrow resonance the energy dependence of the partial and total widths may neglected. Thus, the characteristic Lorentzian form (see fig. 6) of a single resonance results from the oscillator term $\tilde{\gamma}$.

$$\tilde{\gamma} \;=\; \frac{\Gamma_{in}\Gamma_{out}}{(E_{cm}-E_R)^2 + (\Gamma_{tot}/2)^2} \tag{25}$$

The Breit-Wigner cross section in equation 23 can be put into the stellar rate equation 7. Then for a narrow resonance, E_R may be assumed constant and taken outside the integral,

$$< \sigma v > = \sqrt{\frac{8}{\pi\mu}} \frac{E_R}{(kT)^{3/2}} \quad exp\,(-\frac{E_R}{kT}) \quad \int_0^\infty \sigma_{BW}(E)\, dE, \tag{26}$$

such that the integral over the Breit-Wigner cross section can be solved for the limit $E \rightarrow E_R$ and a negligible energy dependence of the partial and total widths. It follows

$$\int_0^\infty \sigma_{BW}\, dE \;=\; \frac{\lambda^2(E_R)}{2}\, \omega\gamma \tag{27}$$

with

$$\gamma \;=\; \frac{\Gamma_{in}\Gamma_{out}}{\Gamma_{tot}}. \tag{28}$$

The product $\omega\gamma$ is commonly referred to as the resonance strength.

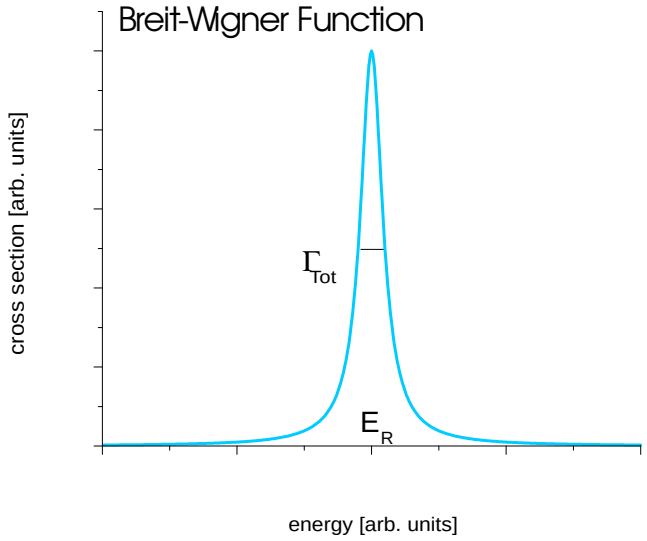

Figure 6: Breit-Wigner curve

If several narrow resonances contribute, the stellar rate can be written as the sum over the individual states.

$$< \sigma v > = \; (\mu kT)^{-3/2} \frac{h^2}{\sqrt{2\pi}} \quad f \quad \sum_i (\omega\gamma)_i \; exp\,(-\frac{E_i}{kT}) \tag{29}$$

Here, the factor f accounts for electron screening effects, reducing the repulsive Coulomb force.

3.4 Laboratory Yield of a Resonance Measurement

In a laboratory environment the target is at rest while the projectiles approach with a very small distribution in energy. Predominantly through Coulomb interactions, the projectile ions lose a fraction of their kinetic energy while travelling through the target material. The energy loss ε is defined as the energy loss per target particle in a unit area or

$$\varepsilon \;=\; \frac{1}{n}\,\frac{dE}{dx} \tag{30}$$

with dx being the target length in beam direction and n the number of active target ions. Assuming that their geometrical cross sections don't overlap, n can be calculated for a gas target at pressure P in Torr and temperature T in Kelvin, using the Lohschmidt number $L = 2.69 \cdot 10^{19}\; at/cm^3$; ν represents the number of atoms per molecule:

$$n \;=\; \nu L\,\frac{P}{760}\,\frac{273}{T}. \tag{31}$$

Traversing the target, the projectile ions approach the target nuclei with decreasing, yet assimilable energy. Contrary to the stellar rate, the experimentally observed yield Y per incident ion is therefore the cross section integrated over the total energy loss ΔE, which simultaneously accounts for the target density.

$$Y(E_{in}) \;=\; \int_{E_{in}-\Delta E}^{E_{in}} \sigma(E)\,\frac{1}{\varepsilon} \quad dE \tag{32}$$

For a narrow resonance the Breit-Wigner cross section (23) σ_{BW} may be employed. Thus, in good approximation, the integral is solved by the function

$$Y(E_{in}) \;=\; \frac{\lambda^2}{2\pi}\,\omega\gamma\,\frac{m_p+m_t}{m_t}\,\frac{1}{\varepsilon} \quad [\,atan\,(\frac{E_{in}-E_R}{\Gamma/2}) - atan\,(\frac{E_{in}-E_R-\Delta E}{\Gamma/2})\,], \tag{33}$$

assuming that the energy dependence of the partial widths $\Gamma_{in,out}$, energy loss ε and de Broglie wave length λ are negligible.

A simplified excitation curve for a thick target yield $\Delta E \gg \Gamma_{tot}$ is displayed in fig.7. For an infinitely thick target, the energy loss is such, that the full resonance, including the high and low energy tails, is contained within the target. The yield is maximized. For a finite target, a thick target condition can be assumed when the energy loss ΔE within the target is at least six times the width of the resonance Γ_{tot}. While the steepness of the edges contains information about the resonance width and the energy spread of the beam, the maximum yield per incident ion is given by the height of the plateau (eq.33). Here, λ^2 is in cm^2, $\omega\gamma$ in eV, the projectile and target mass in amu and ε in eV cm^2/atom.

$$Y_{max} \;=\; \frac{\lambda^2}{2}\,\omega\gamma\,\frac{m_p+m_t}{m_t}\,\frac{1}{\varepsilon} \tag{34}$$

To calculate the maximum yield, corrections for the detection efficiency of each specific set-up have to be applied.

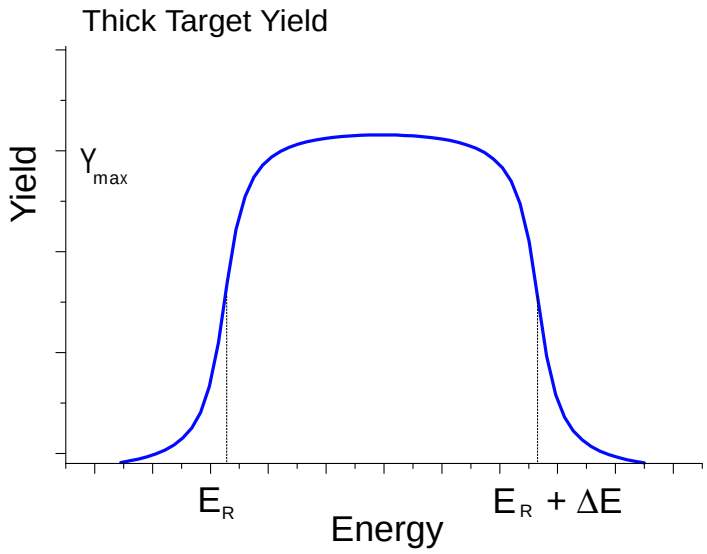

Figure 7: Thick target yield curve

3.5 Inverse Kinematics

In this work, only radiative proton capture reactions were considered. All resonance measurements were performed in inverse kinematics with the heavy ion beam impinging on a light hydrogen gas target. Momentum conservation requires that the recoiling nuclei leave the target with almost the same momentum as the incident beam particles, neglecting a slight difference in energy loss within the target. Therefore, the relation between projectile and recoil energy is

$$E_r \;=\; \frac{m_p}{m_r} E_p \;. \tag{35}$$

Because of the prompt gamma emission, the recoil momentum distribution is broadened and the recoils can leave the target at a slight angle from the beam axis (fig. 8). In general, the recoil opening angle depends on the beam energy and the energies of the emitted γ-rays. Even when the energy can be released through a cascade of emitted γ-quanta, with momentum transfers in different directions, the maximum angle is defined by the excitation energy of the compound state E_x.

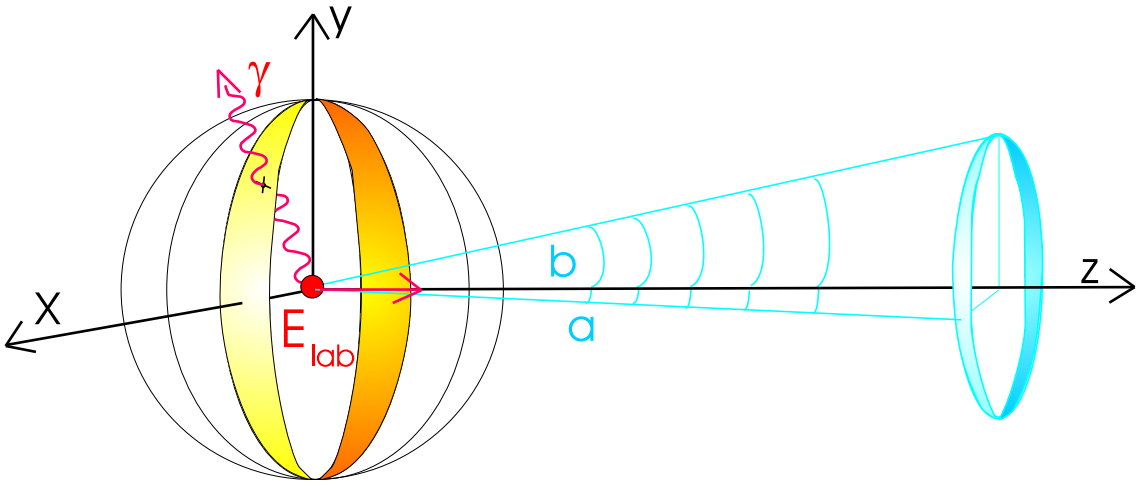

Figure 8: Recoil opening cone due to de-excitation of the compound nucleus

If the energies are in keV and the mass in amu, the maximum angle of the recoil opening cone $\Phi_{1/2}$ can be calculated

$$\Phi_{1/2} \;=\; \arcsin\frac{E_x}{c\cdot p_p} \;=\; 0.733\frac{E_\gamma}{\sqrt{E_{lab}\,m_p}}\,. \tag{36}$$

The gamma emission causes a spread of momentum within the recoiling ions according to

$$\frac{\Delta p}{p} \;=\; \frac{E_\gamma}{\sqrt{2m_pc^2\,E_{lab}}} = 0.0733\,\frac{E_\gamma}{\sqrt{E_{lab}\,m_p}}\,. \tag{37}$$

That leads to an energy spread twice as high, because of

$$\frac{dE}{E} \;=\; 2\,\frac{dp}{p}\,. \tag{38}$$

The transformation from laboratory energy to the center-of-mass system goes simply like

$$E_{lab} \;=\; \frac{m_p+m_t}{m_t}\,E_{cm}. \tag{39}$$

3.6 Error Analysis

The error analysis was performed employing a common Gaussian approach. To avoid any misunderstanding the applied standard equations shall be summarized briefly in the following.

The statistical error of an individual measurement with n_i good events is

$$\sigma_i \;=\; \sqrt{n_i}. \tag{40}$$

Then the weighted mean value $\bar{x}$ of several independent measurements of the results x_i is

$$\bar{x} \;=\; \sum_{i=1}^{N} \frac{x_i}{\sigma_i^2} \quad (\sum_{i=1}^{N} \frac{1}{\sigma_i^2})^{-1}, \tag{41}$$

with the error on the mean value being the bigger number of

$$\sigma \;=\; \sqrt{\frac{1}{\sum \frac{1}{\sigma^2}}} \qquad or \qquad \sigma \;=\; \sqrt{\frac{\sum \frac{(x_i-\bar{x})^2}{\sigma_i^2}}{(n-1)\sum \frac{1}{\sigma_i^2}}}\,. \tag{42}$$

When the final calculated number $f(y_i)$ is the result of several individual values x_i with independent errors Δx_i, Gaussian error propagation was applied to calculate the overall error Δf according to

$$\Delta f \;=\; \sqrt{\sum_i (\frac{\partial f}{\partial x_i}\Delta x_i)^2}. \tag{43}$$

Finally, the fit to the measured yield curve can be evaluated in a χ^2- test

$$\chi^2 \;=\; \sum \frac{(y_i - f(x_i))^2}{\sigma_i^2}\,, \tag{44}$$

with $f(x_i)$ being the value of the fit at the variable x_i with the value y_i and the error σ_i.

4 The $^{21}Na(p,\gamma)^{22}Mg$ Reaction

Since the nucleosynthesis through $^{21}Na(p,\gamma)^{22}Mg$ will be dominated by resonant capture, in comparison to the much weaker direct capture, the experimental objective is to provide the required data on the resonances, in order to improve network calculations. The present knowledge on resonant states in ^{22}Mg is based on transfer reactions such as the recently published $^{24}Mg(p,t)^{22}Mg$ [BAT01] and $^{12}C(^{16}O,^{6}He)^{22}Mg$ [CHE01]. Additional sources of information are comparisons with the isospin mirror nucleus ^{22}Ne and recent data on the elastic scattering channel $^{21}Na(p,p')^{21}Na$ [RUI02]. All of these help to find the energy levels, their particle widths and possibly the spin assignments needed to estimate the gamma width of the exit channel, and thus, the resonance strengths anticipated in the $^{21}Na(p,\gamma)^{22}Mg$ reaction. In the energy regime of interest the level scheme of the compound nucleus ^{22}Mg is dominated by narrow, isolated resonances. Figure 9 provides a graphical summary of the present knowledge. To transfer the level energy into the center-of-mass frame, the literature value for the proton threshold of $Q = 5.501$ keV [AUD95] was employed. As can be seen, at temperatures below 0.4 GK only the lowest three anticipated resonances will contribute significantly to the total rate, unless low energy tails of higher, but broader resonances reach down to the energy regime of interest. While the resonances at $E_x = 5.714$ and 5.962 MeV have been observed in a number of different transfer measurements [BAT01], the resonance at $E_R = 5.837$ MeV was only observed in one study [ROL72] and never independently confirmed. At higher temperatures, like 1 GK possible in X-ray bursts, the Gamow peak lies at $E_0 = 594$ keV with a width $\Delta = 522$ keV. Thus, the Gamow window will cover the resonances at 6.046, 6.248 and 6.323 MeV.

Although much effort has been put into assigning the level spins of the ^{22}Mg nucleus to the isospin mirror, so far no agreement could be achieved. Only the states at 5.714 and 6.046 MeV could be linked to a spin and parity of 2+ and 0+, respectively [BAT01]. According to the available data for the states at 5.294, 5.455 and 5.837 MeV ambiguous assignments have been proposed ([BAT01], [CHE01], and references herein). Moreover, the resonance at 6.248 MeV might even be a doublet. The 5.962, 6.323 and 6.609 MeV states could not be related to the isospin mirror, yet natural parity is usually assumed [BAT01]. Recent measurements of the $^{21}Na(p,p')^{21}Na$ scattering channel have shown that the resonance at 6.323 MeV is very strong [RUI02], so that a J^π of 1^+ seems to be likely. Thus, compared to ^{22}Ne, there is still a state with spin parity 3^- missing. As may be seen, despite extended research, the knowledge on the ^{22}Mg nucleus remains sparse. Therefore, once identified as a potential key reaction, attempts were made to measure the resonance strength directly. If successful, errors due to ambiguous spin assignments can be avoided.

Because ^{21}Na has a half life of only $\tau = 22.48$ sec, experiments on a ^{21}Na target would have been exceedingly difficult. A more promising approach was the study of $^{21}Na(p,\gamma)^{22}Mg$ in inverse kinematics. Here, unstable ^{21}Na ions were formed by online methods and accel-

erated to a radioactive ion beam impinging on a hydrogen gas target. But measurements of the γ-de-excitation of the compound nucleus alone would have been hampered by pile-up gammas of the beta-decaying ion beam. However, a recoil mass separator allows the detection of the recoiling nucleus instead. In addition, coincidence requirements with the recoil provides a background reduced gamma spectrum.

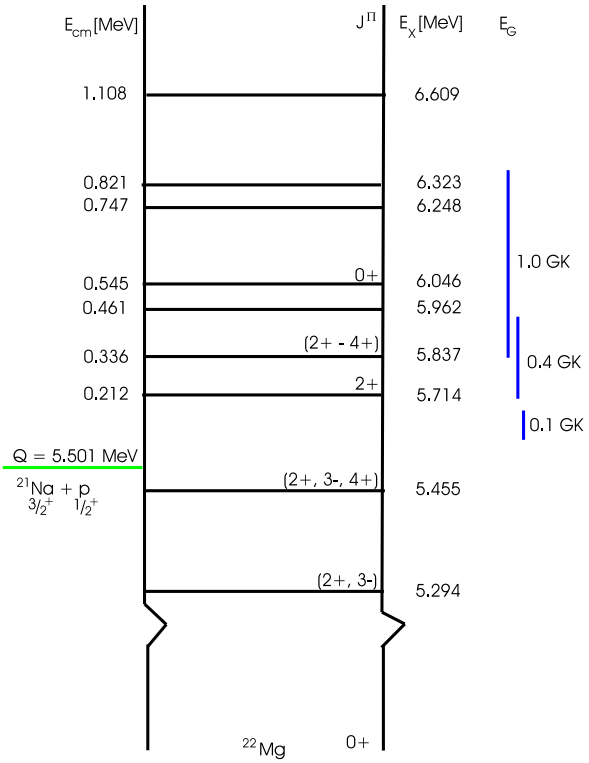

Figure 9: ^{22}Mg nucleus, showing the excitation energies [BAT01] and presumed spin assignments with Gamow windows indicated for several temperatures

Initially, the scientific goal was the measurement of the resonances presumably involved in the nucleosynthesis of nova explosions, mainly the resonance at $E_{cm} = 212$ keV as well as 306, 461 and 545 keV. Those are part of another thesis and will be described elsewhere [BIS02] and [BIS03]. However, in consideration of recent developments, the state at $E_x = 6.323$ MeV was explored first, as it offers a strong resonance, and therefore a promising starting point for the scientific program with respect to the nucleosynthesis of X-ray bursts. Thus, the first experiment conducted with radioactive ion beams at the DRAGON facility, namely, the study of $^{21}Na(p,\gamma)^{22}Mg$ at $E_{cm} \approx 821$ keV, the results obtained and their implementation on nuclear astrophysics will be discussed in the present work.

5 ISAC Beams

The interest in direct measurements of reactions involving radioactive nuclei has lead to the development of radioactive beams facilities. Elaborated ion sources provide a number of different, even short-lived, isotopes for nuclear physics experiments. Meanwhile the accelerator technology has proceeded, so that high intensity pulsed beams with low energy dispersion and narrow emittance become available.
The DRAGON experiment is situated in the new isotope separator and accelerator facility ISAC (fig. 10) recently commissioned at TRIUMF, Vancouver in Canada [LAX01].

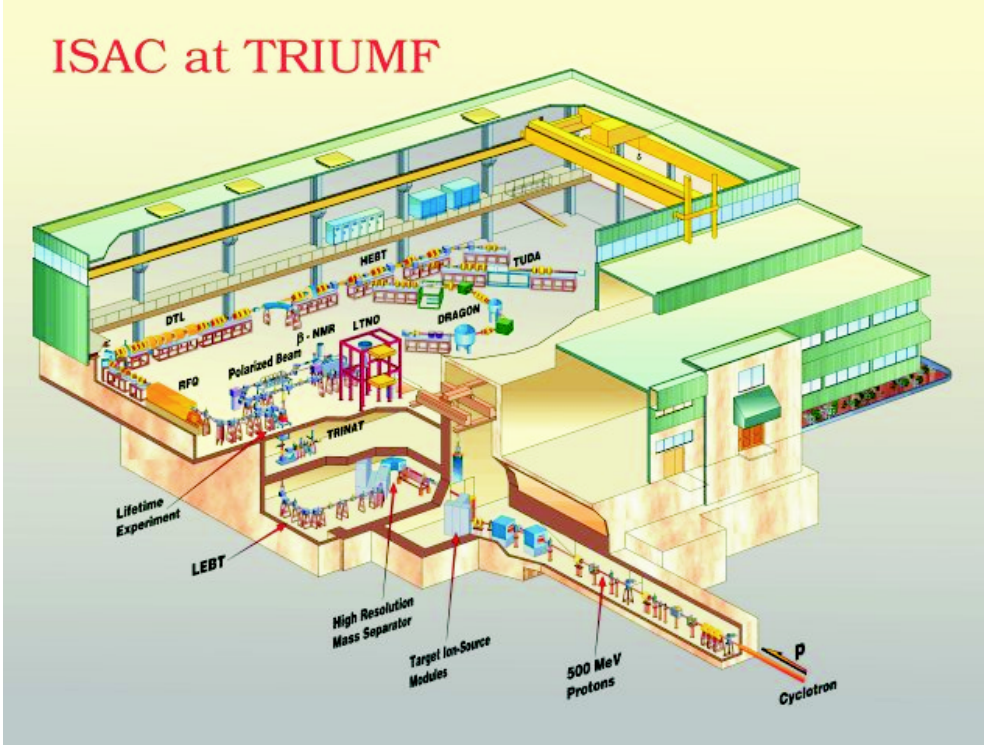

Figure 10: Layout of the ISAC hall

Stable beams are available from an off-line 2.45 GHz microwave source, with intensities of the order of 10 pnA, while radioactive ion beams are produced online employing the ISOL (isotope separator online) method. In this case, a 500 MeV proton beam of up to 100 μA intensity from the TRIUMF main cyclotron hits a heated target. In the case of ^{21}Na beams, this consists of a stack of silicon carbide pellets or foils. Through spallation reactions, various stable and radioactive nuclides are formed and, upon heating to roughly 1500 degrees Celsius, leave the source material by diffusion. The atoms are fed into a subsequent surface ion source, ionized, extracted and mass analyzed in a high resolution

($\Delta M/M = 1/10000$) mass separator. Since a surface ion source primarily ionizes alkali elements, an additional laser and an ECR ion source, are now being installed for future ion beams. Radioactive and stable beams from the off-line ion source are pre-bunched with 11.8 MHz and accelerated through a radio frequency 35.4 MHz quadrupole (RFQ). The RFQ is designed for beams with a ratio $1/30 \leq q/A \leq 1/6$ providing a final energy of 153 keV/u. In the subsequent medium energy beam transport (MEBT) system the ions are further striped through a foil to $1/6 \leq q/A \leq 1/3$ before they are accelerated to their final energy of 0.153 to 1.53 MeV/u by a drift tube linac (DTL), operating at 106 MHz. Since the fundamental frequency of the pre-buncher is chosen to be the third harmonic of the RFQ accelerator, a pulsed structure is imposed on the beam such that out of nine buckets one is filled with beam, with a spacing of 85 ns between bunches. Bunchers placed every 8 to 10 m maintain good longitudinal emittance, low energy spread and high acceleration efficiency, while choppers in the MEBT and high energy beam transport system (HEBT) following the DTL essentially remove most beam leaking into the side buckets of the pulsed structure (fig. 11).

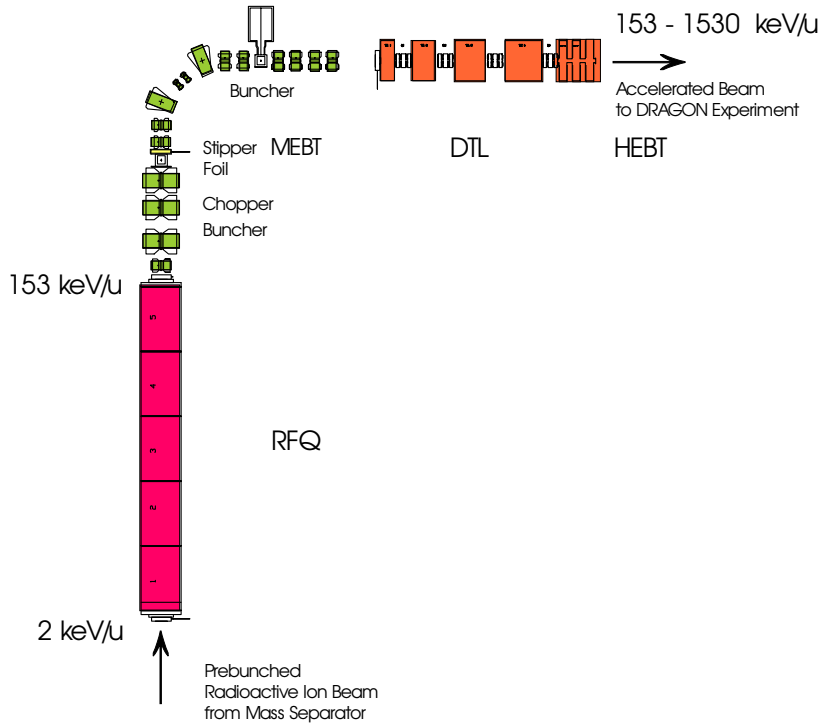

Figure 11: ISAC accelerators

6 The DRAGON Facility

The DRAGON facility [HUT02] includes a windowless gas target with densities of the order of $3 \cdot 10^{17}$ atoms/cm^3 over a geometrical length of 11 cm. Here, the beam ions interact with the target material. The gas target is tightly surrounded by a 30 BGO detector array to monitor the prompt reaction γ-ray. Two surface barrier detectors, at 30 and 55 degrees inside the target chamber, observe beam intensity fluctuations. In addition, radioactive beams are monitored by a beta-detector, measuring the beta activity of the decaying beam at the mass dispersive focus, about 10 m downstream. The target is followed by a double-stage recoil separator of roughly 21 m length, to isolate the recoils of interest from the initial beam. At its end, at the final focus, the recoils are registered in a double sided silicon strip detector (DSSSD).

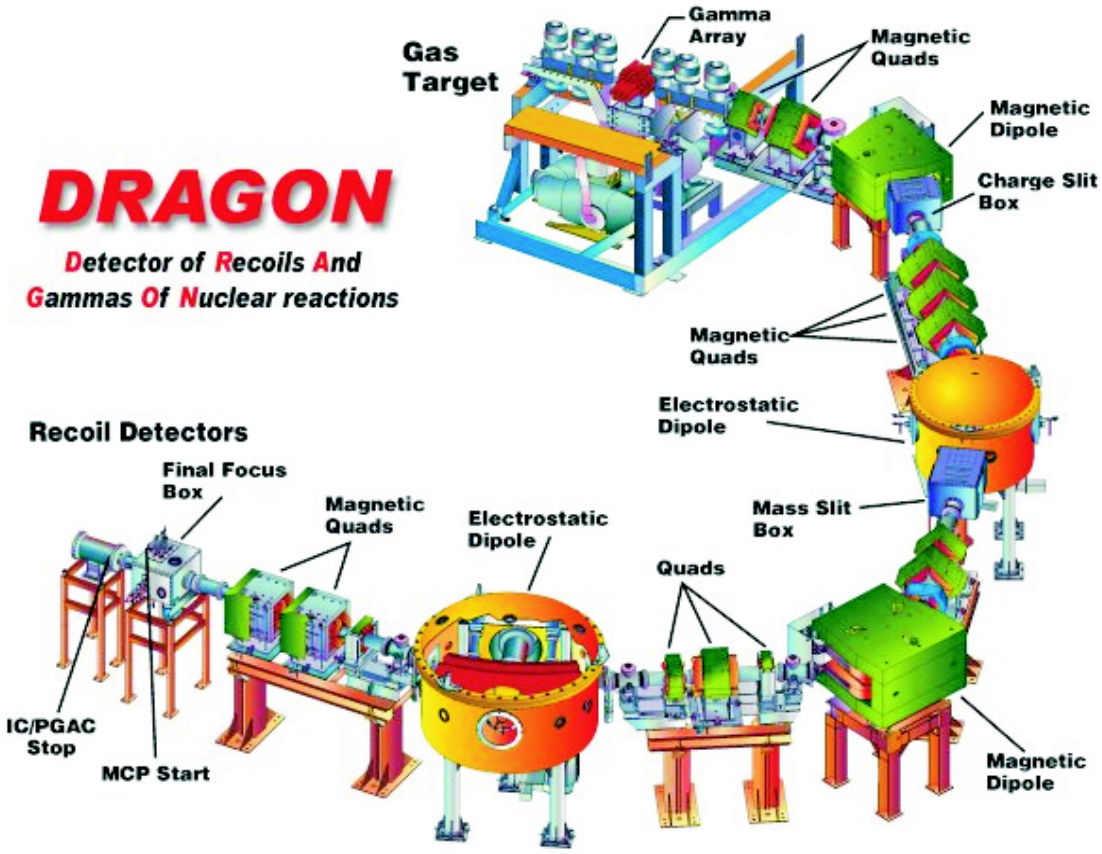

Figure 12: Perspective layout of the DRAGON set-up

6.1 Gas Target

The target is a windowless, differentially pumped, recirculating gas target running hydrogen or helium at typical pressures of about 4.5 Torr in the center cell (fig. 13).

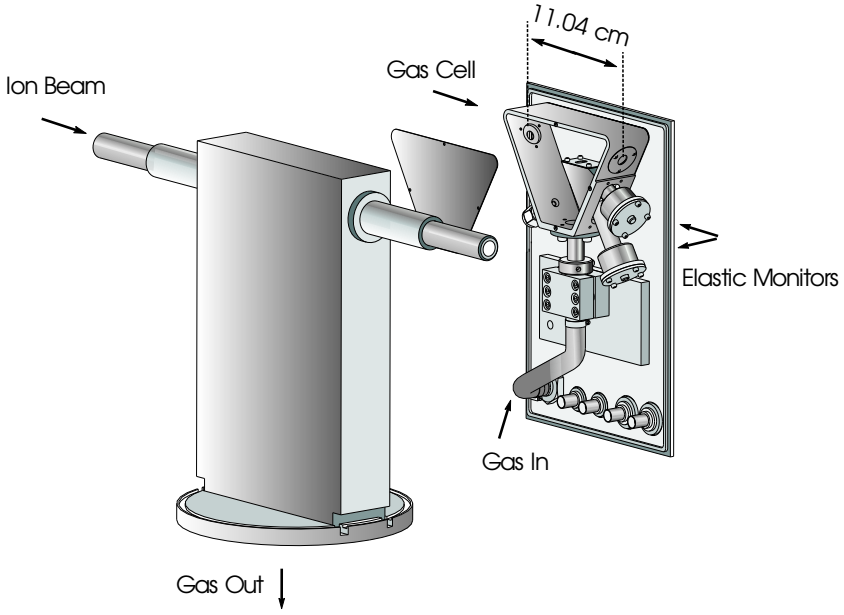

Figure 13: Gas target cell

The inner target cell has a length of 11.02 cm, restricted by two apertures of 6 mm diameter at the upstream and 8 mm diameter at the downstream side. The ends of the inner cell are inclined to 30 degrees to avoid particularly hydrogen gas streaming out into the adjacent pumping tubes. Outside the main cell, in the enclosing box, the pressure is reduced by one order of magnitude to about 0.35 Torr, dropping to 10^{-6} Torr after three more pumping stages upstream and four subsequent stages on the downstream side. Each of the stages is separated from the neighboring through an extended tube to limit the gas flow (fig. 14). The individual tubes are designed to transmit particles leaving the target with a maximum angle of 20 mrad relative to the central axis (fig. 15).

Roots blowers compress the gas from the target system to 45 Torr for recirculation through the cooling trap back into the inner gas cell. The trap contains 2 l of zeolite at liquid nitrogen temperature and purifies the gas to avoid contamination due to pump oil or vacuum leaks. Once saturated with approximately 50 atm l of hydrogen, this stock helps stabilizing the pressure in the target cell to an accuracy better then 1%. Heat exchange within the trap, in addition to the high operational temperature of the pumps, heats the target gas to 300 K, which has been measured with a thermocouple.

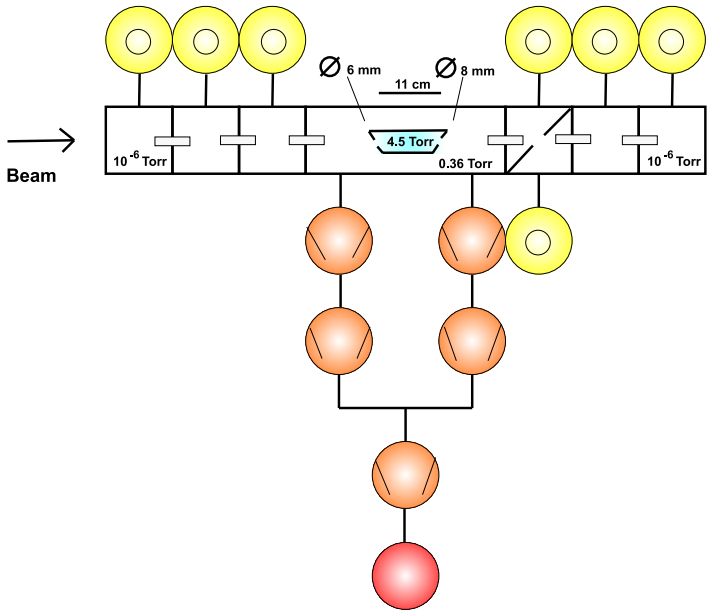

Figure 14: Schematic plot of the differential pumping system

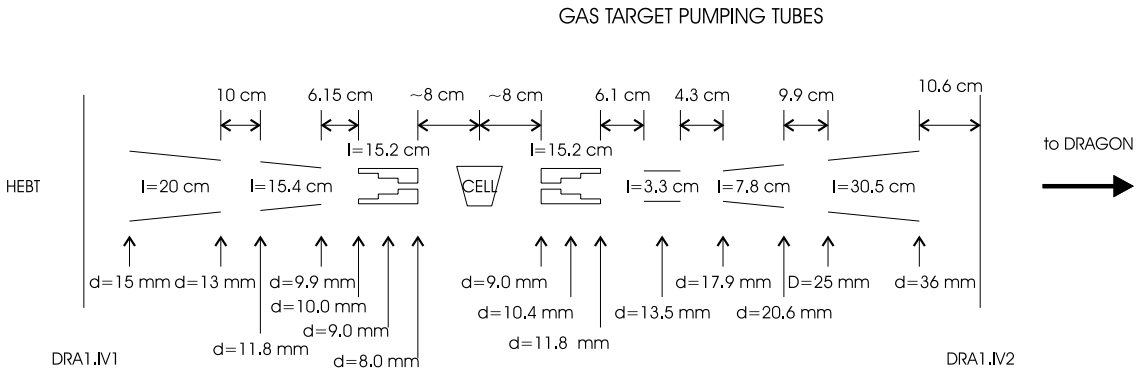

Figure 15: Layout of the pumping tubes

6.2 BGO Gamma Array

The gamma array consists of 30 bismuth germanate (BGO) scintillation detectors of hexagonal cross section with 5.8 cm diameter [HUT02]. These are assembled tightly around the gas target to monitor the prompt reaction γ-rays (fig. 16). The average full width half maximum resolution for a 6.13 MeV γ-energy is 7%. The BGO array was designed to provide additional background suppression via coincidence requirements of the prompt gamma and the recoil detected at the end detector. This, however, can only be done at the cost of overall efficiency.

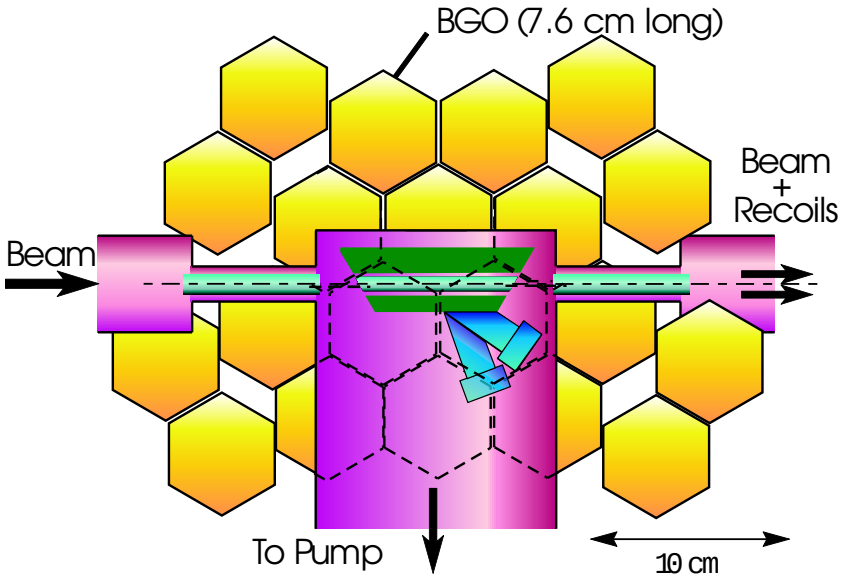

Figure 16: Layout of the BGO detector array

For some radioactive beams, significant background is caused by 511 keV gammas resulting from radioactive β^+-decay of beam ions implanted on the apertures along the beam line. To reduce the dead time, part of the beam line is covered in lead and individual hardware thresholds of 1 to 2 MeV are applied to each single detector when running with radioactive beam. Still, pile-up events cause a beam induced background in the gamma energy spectrum up to approximately 3 MeV. Thus, without coincidence requirements, lower energy reaction gammas cannot be distinguished from background in experiments with radioactive ion beam.
The BGO array detection efficiency strongly depends on the gamma energy, and therefore, the branching characteristics of each individual state populated by resonant capture. Monte Carlo simulations have to be applied in order to calculate the full yield when coincidence events have to be taken into account. Adequate studies will be part of another thesis project [GIG03] and will not be discussed in the present work.

6.3 Recoil Mass Separator

The recoil mass separator [HUT02] is chosen to match the requirements for $^{15}O(\alpha,\gamma)^{19}Ne$. This reaction has a low anticipated yield of 10^{-14} recoils per incoming ion for the relevant resonance at $E_R = 0.504$ MeV, but the widest opening angle ($\Theta/2 = 16$ mrad) among the reactions of interest. An angular acceptance of at least 20 mrad half angle is required, taking into account momentum spread for the incoming particles and further momentum broadening in the gas target due to energy straggling. To reject the incoming beam, the mass separator is designed to have a suppression factor of 10^{-12}. In addition, further discrimination can be achieved by coincidence requirements with the gamma array. Highest mass resolving powers are required in order to separate recoils and beam in the proposed $^{25}Al(p,\gamma)^{26}Si$ experiment, where a mass dispersion of $\frac{\Delta M}{M} \leq \frac{1}{26}$ is necessary. To avoid beam scattering off the electrodes in the filter units, a two stage mass separator was designed. Thus, the first stage could be limited to reject only the majority of the beam, while the second stage has higher mass resolving power to suppress initial beam particles leaking through the mass slits due to charge exchange in the residual gas of the system. The full length of the DRAGON from target center to end detector is 20.7 m (fig. 17).

Following the gas target, a quadrupole doublet Q_1Q_2 focuses the beam onto the first focal plane (Q), just behind a magnetic dipole MD_1, that separates the ions according to their magnetic rigidity $\frac{mv}{q}$ along the horizontal axis, where m, v and q are particle mass, velocity and charge. It should be mentioned that a small sextupole contribution is included in Q_2 through the shaping of its pole tips. Since in a nuclear reaction the momentum is conserved, the magnetic field of MD_1 filters out the most probable charge state, which contains 40 to 60 % of the recoils of interest as well as a large fraction of the beam. A pair of movable, so-called charge slits rejects the rest. Mass separation is provided in combination with an electric dipole ED_1 which follows a quadrupole triplet. The latter is enclosed in a pair of sextupoles (SX) for second order correction $SX_1Q_3Q_4Q_5SX_2$. The electric field distinguishes ions according to their electric rigidity $\frac{mv^2}{q}$ spreading the beam along the mass-dispersive plane (M). Movable mass slits enforce the velocity separation at ED_1 that, including the first filter, implies a mass separation or, strictly speaking, an $\frac{m}{q}$ separation. During normal operation the separator is tuned to achieve an achromatic focus at the mass slits. To increase the mass separation in the second stage, the subsequent filters are designed for an increased resolving power. After a quadrupole doublet in combination with a sextupole, the ions are spread again in the field of the second magnetic dipole ($Q_6Q_7SX_3MD_2$), before another quadrupole focuses them through the last sextupole into the second electric dipole ($Q_8SX_4ED_2$). The last quadrupole doublet Q_9Q_{10} determines the position of the final achromatic focal plane (F), where a pair of slits can be used for further beam rejection before the ions are registered in the end detector.

To tune the beam through the separator ahead of every experiment, four pairs of horizontal and vertical steerers are distributed along the separator, while beam position and

diameter can be monitored during tuning through the movable slits. Each of the slits exists as a combination of horizontal and vertical slits followed by an electron-suppressed Faraday cup. Six beam centering monitors along the beam line support the tuning procedure. Each consists of four isolated square metal plates forming a square from which individual currents are taken.

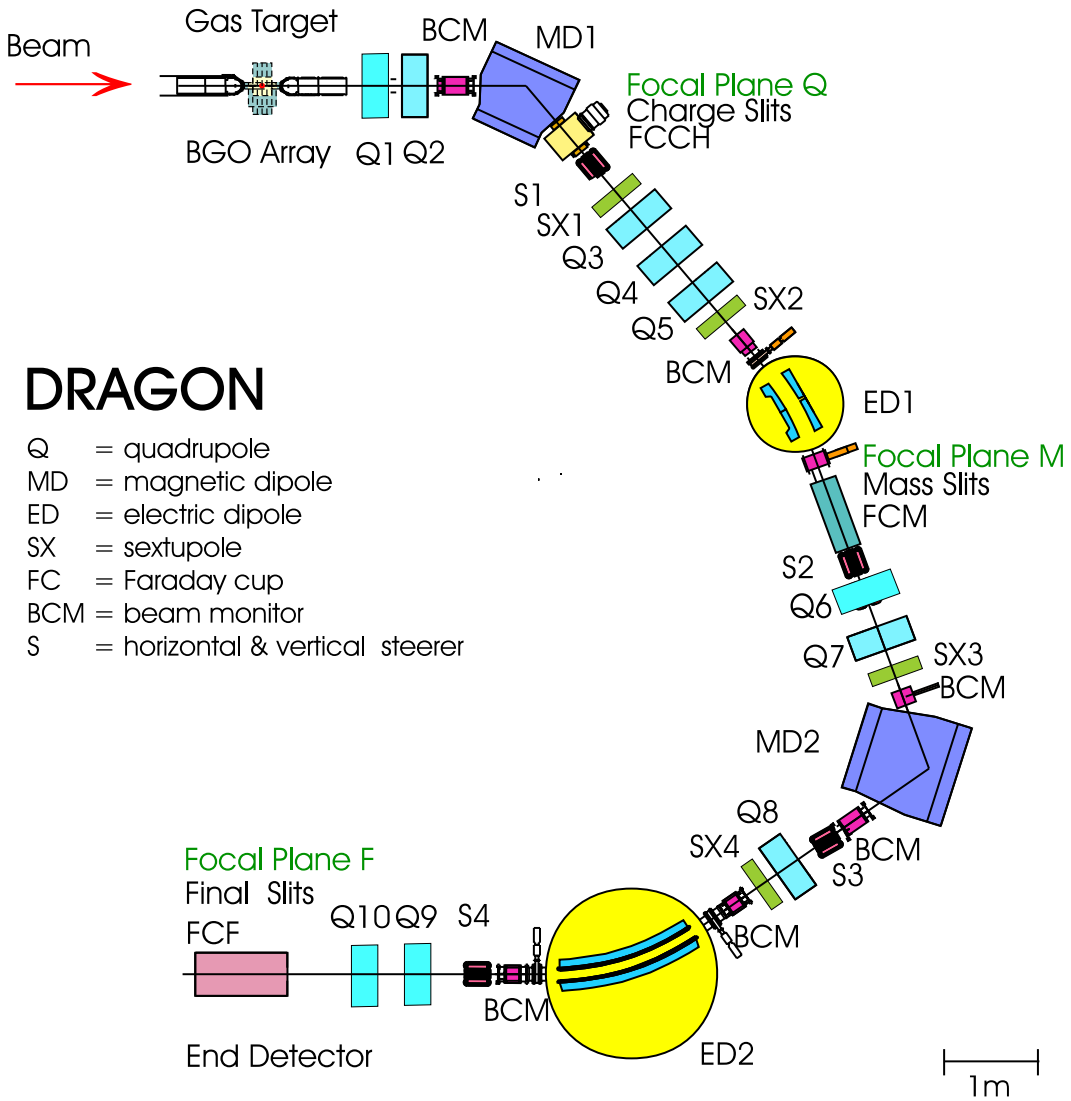

Figure 17: Dragon Layout

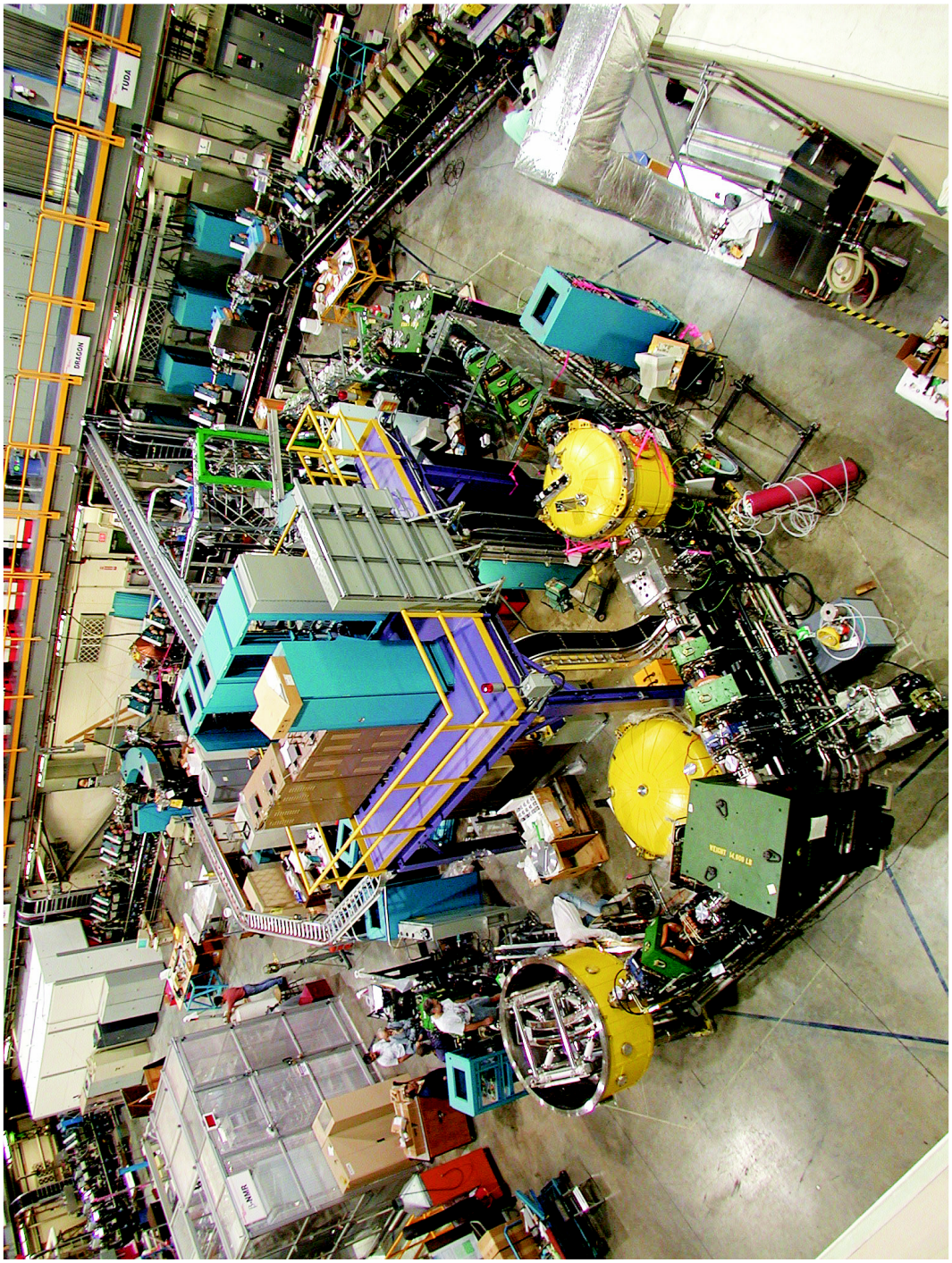

Figure 18: Photograph of the DRAGON Facility

6.3.1 Design of the Filters

All magnetic and electric devices of the separator were designed, constructed and field mapped. Each magnetic device is configurated with a Hall probe to monitor the field; only the two magnetic dipoles are equipped with NMR probes to improve the accuracy. The parameters of the two magnetic and two electric dipoles are listed in the following table 1.

Table 1: Design of the Magnetic & Electric Benders

	Bend Angle [deg]	Radius [cm]	Gap[cm]	Effective Length [cm]
MD_1	50	100	10	87.27
MD_2	75	81.3	12	106.42
ED_1	20	200	10	69.81
ED_2	35	250	10	152.72

6.3.2 DRAGON Ion Optics

The DRAGON recoil separator is characterized by its imaging functions at the focal planes. Of special importance are the foci at charge slits, mass slits and final slits, where movable slits allow transmission of the recoils while simultaneously blocking the beam.
Table 2 provides a list of first-order transfer matrix elements calculated by GIOS [WOL87].

Table 2: First Order Matrix Elements

	Charge	Mass	Final
$(x\|x)$	-0.440	0.688	1.005
$(x\|a)$	0.000	0.000	0.000
$(x\|g)$	0.302	-0.472	-1.870
$(x\|d)$	0.302	0.000	0.000
$(a\|x)$	-1.650	1.146	0.318
$(a\|a)$	-2.276	1.453	0.995
$(a\|d)$	0.401	0.017	-0.021
$(t\|x)$	0.173	0.003	-0.002
$(t\|a)$	0.368	0.000	0.000
$(t\|g)$	0.151	0.504	0.515
$(t\|d)$	-0.485	0.493	-0.477
$(y\|y)$	-3.532	0.980	-1.668
$(y\|b)$	-0.053	-0.441	0.000
$(b\|y)$	-1.554	2.300	1.860
$(b\|b)$	-0.260	0.014	-0.600

In terms of ion optical calculations the different elements are described as matrices. According to the general nomenclature in GIOS, the ion parameters are defined as follows: x, y are the position along the horizontal and vertical axis in meters looking upstream, while z is in the beam direction, a and b are defined as the angles of the ion velocity towards the horizontal and vertical axis in rad. Finally, t, g and d are the fractional time, mass and energy difference, respectively, compared to the mean value. As an example, the matrix element $(x|d)$ describes the particle's distance x from the beam center at a given point in dependence of its initial relative energy $d = \frac{\Delta E}{E}$, while the linear magnification $(x|x)$ marks the position x at a given plane in dependence of the initial value of the coordinate. Thus, the parameters at a given focal plane j can be calculated from the values at an initial position i according to

$$\begin{bmatrix} x_j \\ a_j \\ d_j \\ g_j \end{bmatrix} = \begin{bmatrix} (x|x)_j & (x|a)_j & (x|d)_j & (x|g)_j \\ (a|x)_j & (a|a)_j & (a|d)_j & (a|g)_j \\ (d|x)_j & (d|a)_j & (d|d)_j & (d|g)_j \\ (g|x)_j & (g|a)_j & (g|d)_j & (g|g)_j \end{bmatrix} \begin{bmatrix} x_i \\ a_i \\ d_i \\ g_i \end{bmatrix}$$

According to the ion optics of the DRAGON mass recoil separator, the m/q dispersion for the first stage of the separator can be calculated using the matrix elements as follows:
The energy/charge dispersion at the charge slits is $(x|d)_c$, with the linear magnification from the target center to the slits being $(x|x)_c$. Because of the forces in a magnetic field, the mass/charge dispersion is equal to the energy dispersion $(x|g)_c = (x|d)_c$. From the charge to the mass slits, $(x|x)'_m$ and $(x|d)'_m$ give the linear magnification and energy dispersion, while the mass dispersion is $(x|g)'_m = 0$. Then the overall mass/charge dispersion from the target to the mass slits is given by

$$\frac{m}{\Delta m} = -(x|d)_c \cdot \left(\frac{(x|x)'_m}{(x|x)_c (x|x)'_m}\right) = -\frac{(x|d)_c}{(x|x)_c} \, .$$

The achromatic condition at the mass slits requires

$$\frac{(x|d)'_m}{(x|x)'_m} \; = \; -\,(x|d)_c \, .$$

The second stage with MD_2 and ED_2 can be regarded the same way. There are no slits following MD_2 planned yet to enlarge the separation, and the final slits have usually been operated with a wide opening. Therefore up to now, the second stage has merely been used to transfer the recoils rather than to further separate them, although it may be seen from table 2 that the mass resolving powers of the second stage are significantly higher, than that of the first stage.

6.4 Heavy Ion Detectors

All tests and experiments so far were performed with a double sided silicon strip detector DSSSD (fig. 19) at the final focus. The DSSSD provides spatial resolution in both vertical and horizontal dimension through a grid of 16 individual strips on each plane. Each strip is 3 mm wide and electrically separated from its neighbors by a 110 μm wide gap, thus covering a total area of 5x5 cm^2. Heavy ions hitting the detector produce signals in both layers, thus allowing to measure their position and energy. The back signal is also used for timing. Though events hitting the gap region will be lost for the full energy peak, it has been shown that most of them are detected with an energy reduced by 50%. When a collimated source was moved perpendicular to the strips, the total amount of all counts in the integrated energy spectrum remained constant, even when the source was illuminating a gap region [WRE02]. It should be noted that also leaky beam events might contribute to the low energy counts. However, with statistical methods, these contributions may be accounted for. The detector efficiency is, therefore, assumed to be 99% as is common for regular silicon detectors. The energy resolution in each individual strip measured with a ^{241}Am source (5.486 MeV α-particles) is better than 0.9%. For the beam experiments, the DSSSD is placed in a box, contaminated by an α-emitter during earlier experiments. Events in the DSSSD related to this contamination are sufficiently low in energy to be clearly separated from the recoils of interest, and the α-particles provide a useful source to monitor the DSSSD condition during runs.
In addition to the elastic monitors in the gas target, beam stability during runs with proton-rich radioactive beams can be measured with a "β-monitor", detecting the decay of the beam ions stopped at the mass slits. It consists of two 6 mm thick plastic scintillator slices, recording the positrons released in the decay. Background is suppressed by coincidence requirements of both detector parts.
More sophisticated set-ups are planned. Tests with an ionization chamber as an dE/E telescope or a cooled silicon detector, micro channel plates and a parallel grid avalanche counter for a local time-of-flight are in progress, but will not be discussed in this work.

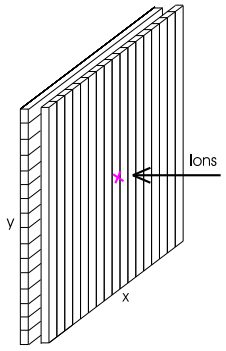

Figure 19: Schematic view of a double sided silicon strip detector

6.5 Data Acquisition Electronics and Software

As can be seen in the block diagram of the DRAGON data acquisition electronics in figure 20, all signals coming from the individual gamma or heavy ion detectors are separately amplified and discriminated [ROG03] and [HUT02]. The signals from the elastic monitors in the gas target are treated like the events in the DSSSD, though not separately indicated in the diagram. Heavy ion events and gammas produce independent trigger signals leading to separate memory buffers with different dead times. Those two triggers are compared via a time to digital converter and tagged in software as a coincidence event if detected within 4 μs. Once one memory buffer is filled to 75%, a signal sent to the data acquisition computer enables the readout of both memories simultaneously. Online, as well as in the off-line analysis, signals can be displayed as singles or, if tagged as such, as coincidence events. Since one event trigger may contain signals from different detector elements, correlations of different signals such as two gamma events from one cascade can be observed as well as the total energy of a single gamma event distributed among different detectors. In addition, independently of the trigger and readout electronics, scalers are counting all events in β-monitor and elastics scattering detector, BGO array and DSSSD together with a pulser. Comparison of the number of events in these scalers (called presented events) to acquired (accepted) events allows the calculation of the system dead time. The data is acquired using the TRIUMF standard MIDAS system [AMA03]. While on-line various spectra are prepared with the PAW++ software [PAW], the off-line analysis discussed in the present work was done with the NOVA analysis software [NOV].

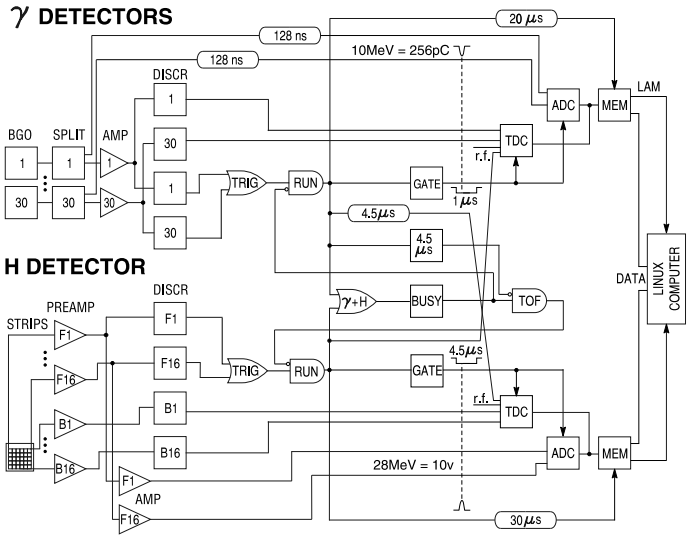

Figure 20: Block diagram of the data acquisition electronics

7 Commissioning of the DRAGON

To achieve reliable and reproducible results from any experiments on the DRAGON set-up, the operation of the experimental equipment and its parameters have to be well understood. Therefore, a series of tests was designed and carried out using various stable beams from the off-line ion source.
First, important ion beam properties such as energy spread and stability were studied to ensure that a resonance, once positioned in the gas target, does not move significantly during data taking. Further, it is shown, how the first DRAGON bending magnet MD_1 could be used to independently determine the absolute ion beam energy. Following these documentations of ion beam properties, experiments to understand the gas target density profile and total thickness are discussed. Next, the ion optical properties of the DRAGON mass separator were compared to their simulated specifications. As a final test, a number of well-known nuclear reactions were re-measured with the DRAGON to compare the results to the published values.
The fundamental ideas and experimental procedures are detailed in the following, along with the analysis of the results and a discussion of their impact on the scientific program.

7.1 Properties of the Ion Beam

Measurements of small cross sections with yields of only a few counts per day rely on the stability of the ion beam energy. Once positioned in the center of the target, the resonance should not move by more than a centimeter and additional broadening should be avoided, thus confining the resonance geometrically well within the gas target cell. These requirements determine the beam properties needed. The geometrical confinement translates into a beam stability and reproducibility of the order of 1 keV/u. In order to keep the total resonance width as narrow as possible, the energy spread of the ion beam should be comparable to the energy broadening in the target. The latter is due to a zero-point motion of the gas molecules, sometimes referred to as a Doppler shift, and energy straggling in the gas target. Combined, this will be of the order of 1 to 2 keV/u.

The first DRAGON beam time at the new ISAC heavy ion accelerator was used to measure the energy stability and spread of the accelerated heavy ion beam. A method to monitor the energy variation even during low intensity radioactive beam measurements was devised. Additionally, a new variation of the nuclear resonance method was employed to determine such properties of the ion beam as energy stability, reproducibility and spread. Here, the resonance was placed in the extended DRAGON gas target, while a geometrical scan over the resonance was performed.

7.1.1 Experimental Set-Up

To measure the beam properties, two resonances at E_{cm} = 404 and 843 keV in the $^{15}N(p,\alpha\gamma)^{12}C$ [ROL74] reaction with natural energy widths of 0.1 and 1.3 keV, respectively in the center-of-mass frame, were employed. The tests were performed using stable ^{15}N beam impinging on a hydrogen gas target. Because the cooling trap was not yet available, the complete gas load was exchanged every 4 to 6 hours. Elastically scattered target material in the 55 deg monitor showed that target contamination was not significant.
To achieve better spatial resolution, the regular DRAGON set-up of the BGO array was slightly altered: On one side of the gas target box, 13 hexagonal BGO gamma detectors were placed in two rows along the beam axis covering a total range of 40.8 cm (Fig. 21). The so-called z-mask fit describes a function of the individual detector response in dependence of its geometrical position, accounting for the geometrical efficiency. Thus, at least within the inner 10 cm of the target box, the relative response of the detectors within the array provided a position sensitivity of approximately 2 mm to the origin of the main reaction, or the position of the resonance. This z-mask feature was employed to measure the distance of a narrow resonance from the target center. Thus, beam shifts of the resonance position within the target could be observed with the BGO array and corrected for in the later analysis.

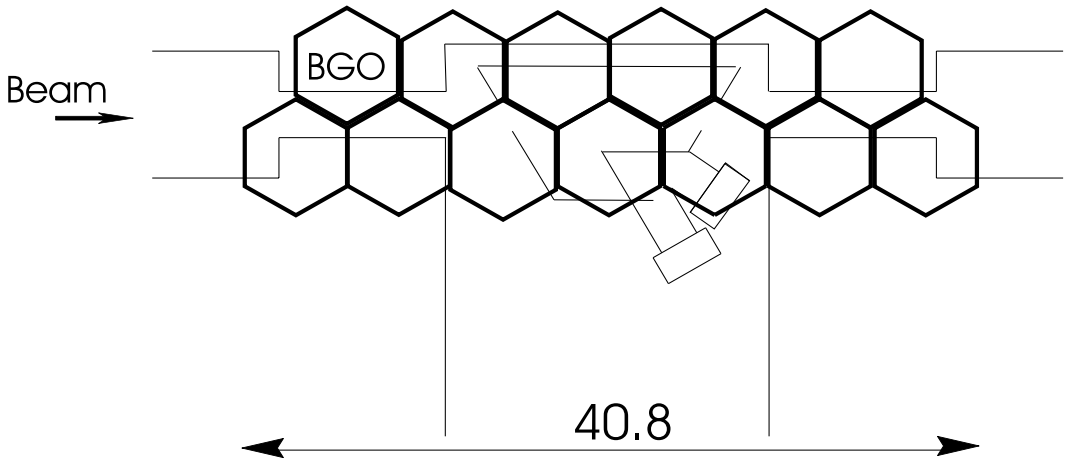

Figure 21: Modified version of the BGO detector array consisting of 13 BGO crystals along the target box

On the opposite side of the target chamber, a single BGO crystal shielded with 10 cm of lead to the front and 5 cm to the sides was placed on a movable sleigh (Fig. 22). A 10 cm long slit of 0.55 cm width starting at a distance of 3 cm to the center of the target allowed to monitor an effective target length of 0.94 $\pm$ 0.1 cm, which was measured with an AmBe source (4.4 MeV γ-energy). The position of the shielded detector was determined by a

scale, mounted on the outside of the target, with the mark at 21 cm roughly corresponding to the target center.
The beam energy was selected to center the resonances in the target. By moving the collimated BGO along the beam axis, the resonances were scanned at various pressures, namely, 5.2 Torr for the 843 keV resonance and at 5.7, 5.6, 4.1, and 2.5 Torr for the 404 keV resonance. For some measurements the room background was reduced by requiring coincidence of gamma signal and the radio frequency pulse coming from the accelerator pre-buncher. Then the count rate in the BGO detector was normalized to the elastically scattered protons to correct for beam intensity variations over the runs.

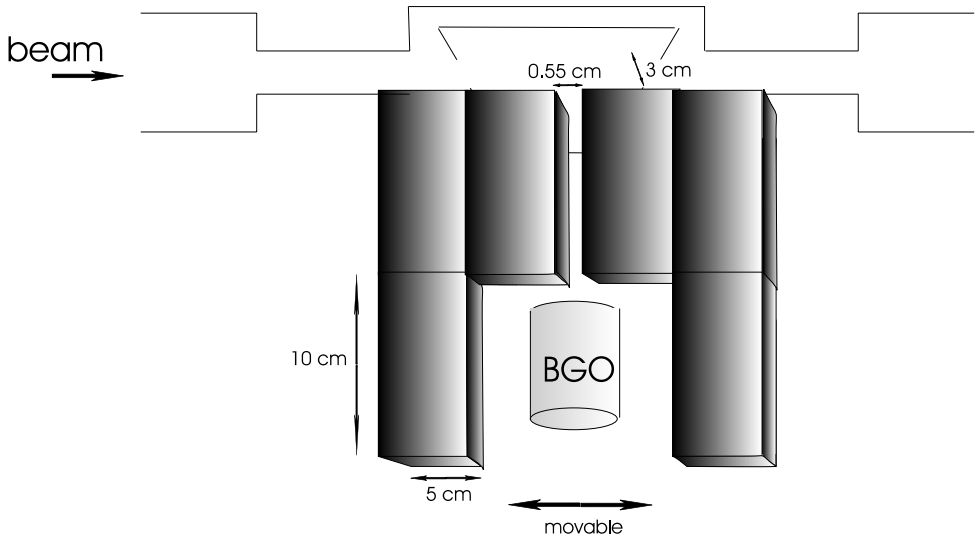

Figure 22: Set-up of the movable BGO detector shielded by lead bricks

7.1.2 Energy Stability

The 4.4 MeV gamma ray spectrum produced by the two nuclear resonances was almost free of background as shown in figure 23. Yet, as could be observed during the runs, the energy of the beam shifted over time. At 2.5 Torr, two data sets of the low energy resonance were obtained by scanning it twice within 4 hours (fig. 24). During the time the position of the resonance had shifted by 0.53 cm, which would correspond to a beam energy shift of 4.4 keV (0.29 keV/u) [BIE00]. This position shift over run time could also be monitored in the z-mask fit which displayed the position of the center of gamma-activity in the target. According to the z-mask, the total shift summed up to 0.9 cm or 0.5 keV/u over 190 min (fig. 25). Similarly, for other measurements the observed shifts varied between -0.6 and +0.4 keV/u, each over periods of 3 to 7 hours. The results of the shift observed in the z-mask were compared with the time correlation of the 55 degree elastic scattering monitor

versus the rf-signal (fig. 26). The clear correlation confirmed the assumption of a change in the beam energy (fig. 27).
To take the energy variation into account, the detector position was corrected relative to the resonance center with the shift measured in the z-mask fit. For the runs at 2.5 Torr this led to a single curve with a center at 23.5 cm and a width of 3.6 cm (fig. 24).

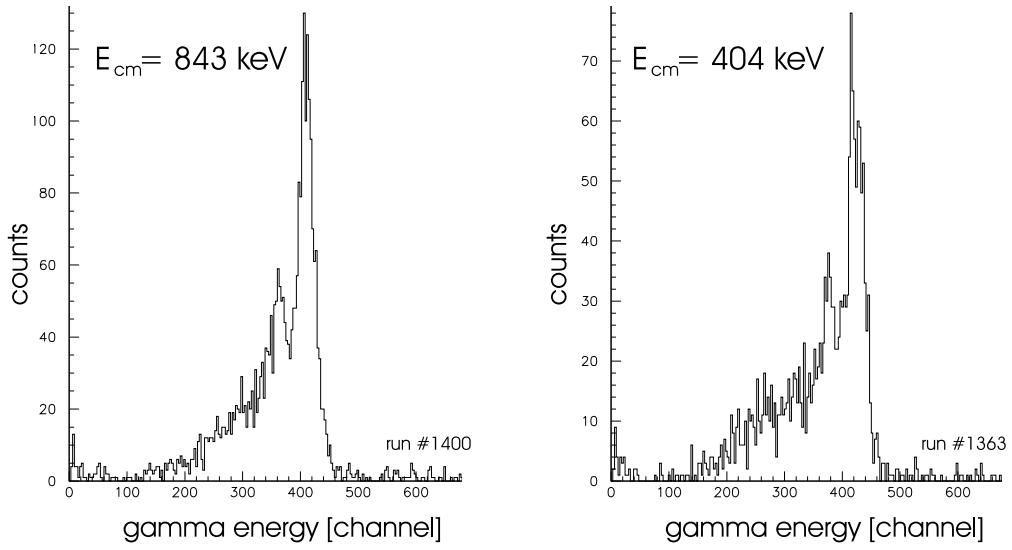

Figure 23: Typical gamma energy spectrum for $^1H(^{15}N, \alpha\gamma)^{12}C$ at E_{cm} = 843 and 404 keV

Instabilities in the beam energy, probably resulting from a degradation in the stripping foil, are unavoidable. In principle, they can be corrected for with the z-mask. However, this procedure relies on high gamma yields which will not be available in experiments with low intensity radioactive ion beams. Yet, as has been shown, the relation of the rf-time and the scattering monitor is capable of recording small energy changes over time, though not unambiguous due to the high repetition frequency of the beam pulses. Alternatively, as it was done in later experiments, relatively short run times can be chosen with the incoming beam energy being measured before every run.

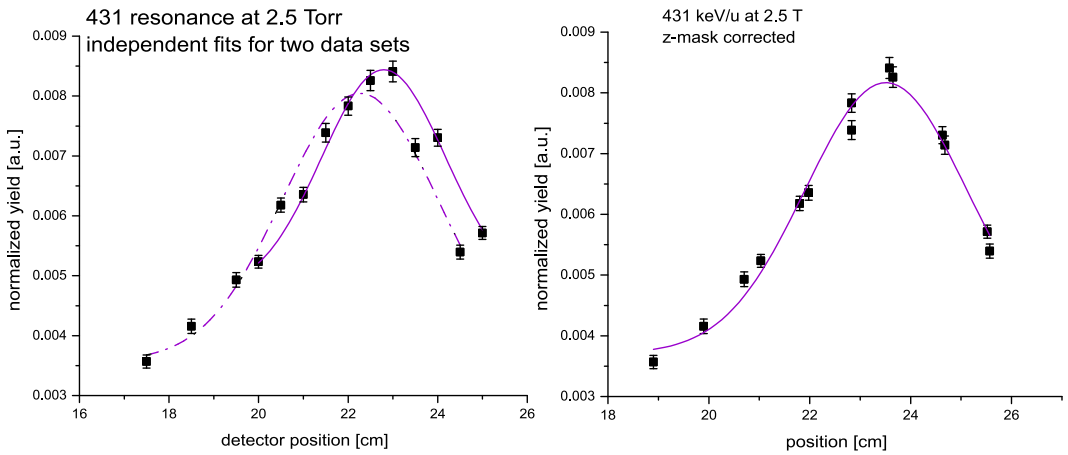

Figure 24: Scans of the 426 keV resonance, with and without energy shift correction

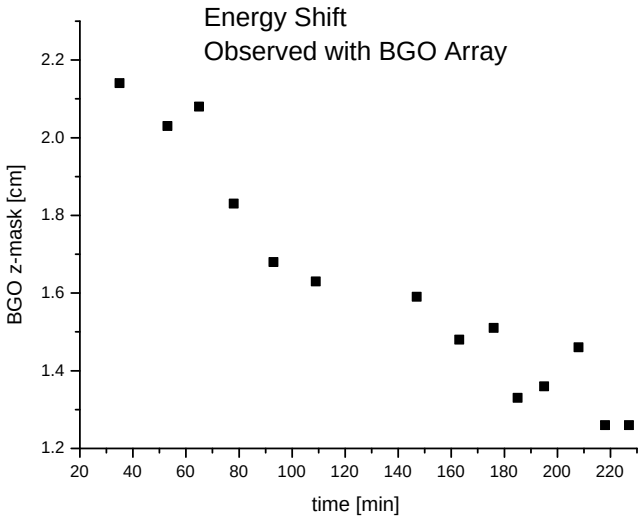

Figure 25: Position shift of the low energy resonance monitored with the z-mask feature

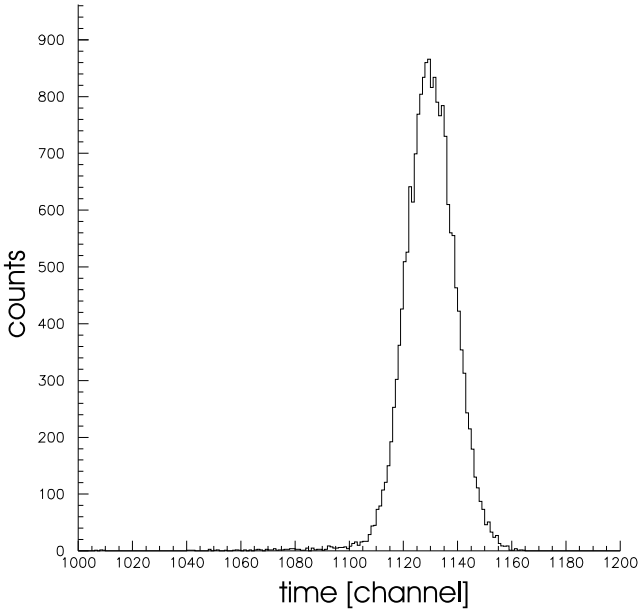

Figure 26: Typical spectrum of the time correlation between elastic monitor and rf-signal

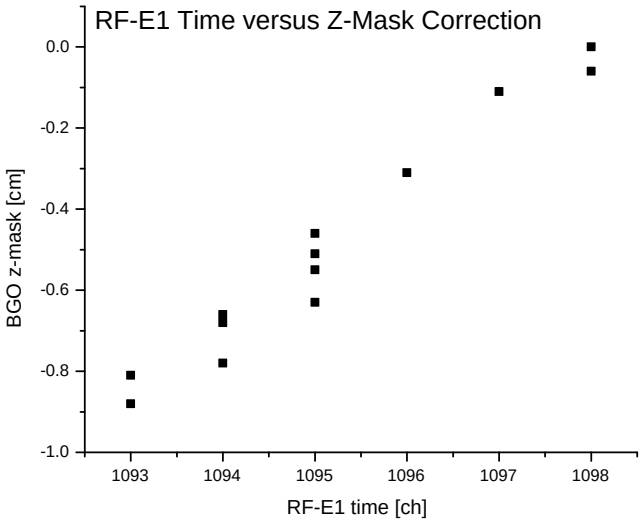

Figure 27: Linear relation of the position of gamma ray activity within the target and the position of the peak in the elastic monitor time spectrum

7.1.3 Beam Energy Spread

In order to determine the energy spread of the beam coming from the accelerator, the yield curve was measured with the shielded detector at five different accelerator tunes and various pressures. Once the yield curve was fitted with a Gaussian function, the geometrical width obtained in centimeter was transferred to keV/u using SRIM [BIE00]. To de-convolute the contribution from the accelerator, it was assumed that the energy width of the resonance had four main components, namely, the natural width of the Lorentzian shaped resonance Γ_{nat} plus the Gaussian shaped broadening due to the Doppler broadening by the molecular movements in the gas $\Gamma_{Doppler}$, the energy straggling of the projectiles in the gas target Γ_{strag}, and the beam energy spread from the accelerator Γ_{beam}, which was specific for each accelerator tune. While the latter three Gaussian contributions could be summed quadratically, the Lorentzian natural width was added linearly [AMS83].

$$\Gamma_{tot} = \Gamma_{nat} + \sqrt{\Gamma_{beam}^2 + \Gamma_{Doppler}^2 + \Gamma_{strag}^2} \tag{45}$$

The Doppler spread was measured for the low energy resonance [BOR99] and, in general, may be scaled for a gas with only translational degrees of freedom according to [BET37]

$$\Gamma_{Doppler} = 4\sqrt{ln2} \cdot \sqrt{\frac{m_p}{m_t} E_R \cdot kT}. \tag{46}$$

To correct for additional broadening due to vibrations and rotations of the H_2 molecule equation 46 has to be extended to

$$\Gamma_{drv} \;=\; 4\sqrt{ln2} \cdot \sqrt{\frac{m_p}{m_t} E_R \, (E_{trans} + E_{vib} + E_{rot})} \tag{47}$$

Thus, the factor kT becomes the quadratical sum over all velocities contributing to the target movement. Here E_{vib} and E_{rot} give the energy of the vibrational and rotational excitation of the target molecule [BOR99] and [HOR88].
For the resonance at $E_{cm} = 404$ keV the total Doppler broadening of the resonance was measured [BOR99] and calculated [HOR88] to be roughly 8.5 ± 0.07 keV or 0.57 ± 0.01 keV/u. For other resonances it scales with

$$\Gamma_{drv} \;=\; 8.5 \, \frac{1}{m_p} \sqrt{\frac{m_p}{15} \cdot \frac{E_{lab}}{431}} \quad keV/u \; . \tag{48}$$

To estimate the energy straggling the measurements of [HOR88] were used and scaled to the energy loss in the much thinner DRAGON target.

$$\Gamma_{stragg} \;=\; 1.69\,\frac{1}{m_p}\,\sqrt{dE} \tag{49}$$

Here, dE is the energy loss in the target up to the position of the resonance in keV.

The geometrical detector resolution of 0.94 cm was treated like an additional Gaussian broadening subtracted in quadrature from the measured resonance width. The results of the beam energy spread are listed in table 3. It should be noted that the energy spread in the tune for the resonance at $E_{lab} = 901$ keV/u was known to be about 3 times broader than normal.

Table 3: Contributions to Total Beam Energy Spread, without Last HEBT Buncher

E_{true} (keV/u)	P (Torr)	Γ_{nat} (keV/u)	Γ_{tot} (keV/u)	$\Gamma_{Doppler}$ (keV/u)	Γ_{strag} (keV/u)	Γ_{beam} (keV/u)	$\frac{\Gamma_{beam}}{E_{beam}}$ %
438	5.7	0.12	3.4 ± 0.3	0.56 ± 0.01	1.3 ± 0.07	2.9 ± 2.0	0.7 ± 0.5
434	4.1	0.12	2.2 ± 0.3	0.56 ± 0.01	1.1 ± 0.06	1.7 ± 0.9	0.4 ± 0.2
433	2.5	0.12	2.1 ± 0.1	0.56 ± 0.01	0.9 ± 0.04	1.7 ± 0.4	0.4 ± 0.1
437	5.6	0.12	2.5 ± 0.1	0.56 ± 0.01	1.3 ± 0.07	1.9 ± 0.5	0.4 ± 0.1
899	5.2	1.6	8.2 ± 1.3	0.82 ± 0.02	1.1 ± 0.06	6.7 ± 21.6	0.7 ± 2.4

As can be seen, for a normal ion beam tune, the energy spread of the beam is in the order of the energy straggling in the target. Thus, the beam energy spread causes a broadening of the resonance that is less than 2 cm. However, it should be mentioned that the above tests were performed, before the last buncher, following the DTL accelerator, was installed. Though DRAGON time schedules did not permit a comparison of the above results with improvements expected from this upgrade, it can be assumed that these results may be treated as upper limits.
As expected from the accelerator design, a constant energy spread of 1 keV/u over the full range of energies was measured in a later study and is presented elsewhere [LAX01]. Therefore, the present beam properties should be equal or better than the 2 to 7 keV/u measured, especially at energies above 400 keV/u, where the high beta buncher is usually employed now.

7.2 Energy Calibration

Although not initially planned when designing the DRAGON, it was considered needed to find an independent procedure to measure the energy of the incoming beam. The most obvious solution was to use the first magnetic bender MD_1 of the DRAGON recoil separator. For a given mass and charge state, MD_1 provides a velocity and therefore energy dispersive focus according to

$$(\vec{B} \times \vec{v}) \cdot q = \frac{m\vec{v}^2}{\vec{r}} \tag{50}$$

$$E_{lab} = c_{mag} \cdot \frac{B^2 \cdot q^2}{m} \tag{51}$$

in the non-relativistic approximation, where c_{mag} is a constant. It can be shown that the systematic error due to the neglect of the relativistic effects is below 0.1/A %, which falls significantly below other contributions discussed later in this chapter.
In principle the magnetic constant c_{mag} may be calculated using the bending radius r from the specifications. With m the particle mass in amu, E_{lab} the energy of the particle in the laboratory frame in keV/u, q the charge in units of e, and B the magnetic field in Gauss needed to center the beam at the subsequent charge slits, it follows

$$c'_{mag} = 4.824 \cdot 10^{-4} \quad \frac{keV\ amu}{Gauss^2}. \tag{52}$$

However, this calculation had to be verified experimentally.

7.2.1 Experimental Set-Up

The magnetic constant in equation 51 was measured with two well known resonances, that were previously studied in independent experiments with independent energy calibrations, namely $^{21}Ne(p,\gamma)^{22}Na$ at E_{cm} = 258.6 keV [GOE82] [END98] and $^{20}Ne(p,\gamma)^{21}Na$ at E_{cm} = 1112.6 keV [BLO69], [END98]. It should be mentioned that, strictly speaking, the above resonance in $^{21}Ne(p,\gamma)^{22}Na$ is a doublet. Yet, since the state at 257.6 keV is a factor of 40 times weaker than its companion, its effect was neglected in the analysis.
In both cases, the resonance position was obtained using the z-mask feature of the BGO array for at least three different pressures with a given beam energy. In addition, the magnetic field needed to center the outgoing beam at the charge slits for each pressure was determined. Thus, the relation between position and pressure as well as pressure and magnetic field were measured. The pressure required to center the resonance in the z-mask distribution was determined by interpolating to P(z=0). Likewise, for each energy the magnetic field B was interpolated and determined for B(z=0). The latter gives already

the magnetic constant for a beam with an energy equal to the resonance energy minus the energy loss in the second half of the target. However, to avoid errors due to an uncertainty in the energy loss, P(z=0) and the related magnetic field were measured for decreasing beam energies, thus shifting P(z=0) to lower pressures. Then, plotting the necessary magnetic field B(z=0) versus the target pressure P(z=0) and extrapolating the relation to zero pressure, provided the magnetic field corresponding to the resonance energy without any energy loss.

7.2.2 Evaluation of the Results

Figure 28 shows the results for the tests with $^{20}Ne(p,\gamma)^{21}Na$ at E_{cm} = 1112.6 keV and $^{21}Ne(p,\gamma)^{22}Na$ at E_{cm} = 258.6 keV. Both curves agree remarkably well with the calculated relation.
To calculate c_{mag} the adopted resonance energies were taken from the Endt compilation [END98], while the masses were used with respect to the 1995 update to the atomic mass evaluation [AUD95]. The errors listed in table 4 on c_{mag} indicate the uncertainties of the linear fits.

Table 4: Magnetic Constant c_{mag}

Reaction	E_{cm}	m_p	B-field	q	c_{mag}
$^{20}Ne(p,\gamma)$	1112.6 ± 0.6	19.992	3874.0 ± 0.7	8	(4.828 ± 0.003) $\cdot 10^{-4}$
$^{21}Ne(p,\gamma)$	258.6± 0.4	20.994	3927.4± 3.1	4	(4.806 ± 0.011) $\cdot 10^{-4}$

Therefore, the weighted mean value for c_{mag} is

$$c_{mag} \;=\; (\,4.827 \;\pm\; 0.003\,) \cdot 10^{-4} \quad \frac{keV\ amu}{Gauss^2}\ .$$

Without slits on the upstream side of MD_1 the incoming angle is, in principle, only confined by the pumping tubes of the gas target. Thus, this method is limited in accuracy. Because the DRAGON optics (see table 2) are designed to produce a focus at the charge slits, the position should be independent of that of the beam angle in first order optics. However, in second order calculations (table 7) a 4 mrad discrepancy from the central axis, limited by the pumping tubes, leads to a 15 μm/mrad$^2\cdot$(4 mrad)^2 de-positioning at the charge slit image point. With an energy dispersion of 3 mm per percent, the related energy uncertainty is 0.08%. In addition also the magnification $(x|x)$ of the DRAGON optics limits the sensitivity, since a deviation dx from the central position in the target results in an energy uncertainty of $(x|x)/(d|x)\cdot$dx. Assuming a possible misplacement in the target of dx = 1 mm, the resulting energy uncertainty is 0.15%, although careful tuning does limit these effect to a minimum. Including the operator dependent precision

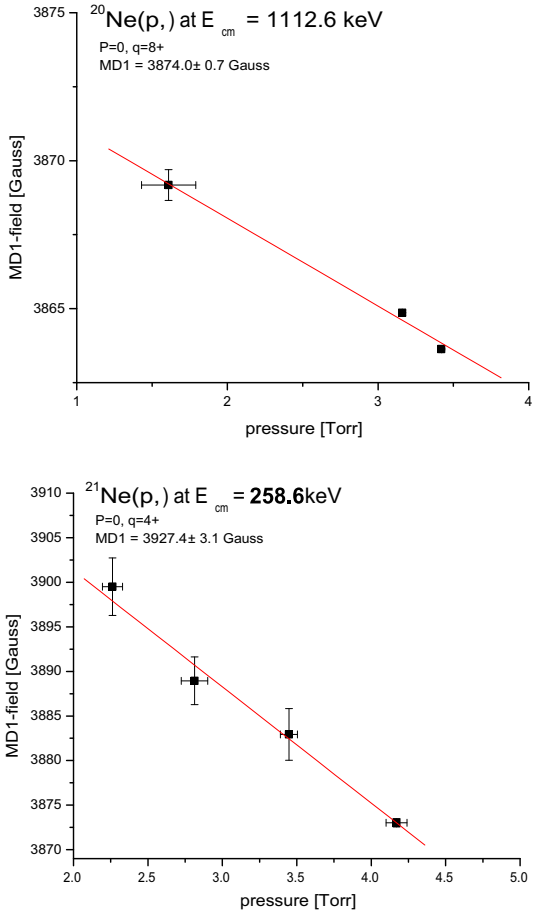

Figure 28: Energy calibration of MD_1

of the MD_1 tune, which is about 0.5 mm in average or 0.15%, the overall accuracy for an individual measurement is about 0.2%.
It should be mentioned that the masses used in the following are the published isotope masses from [AUD95] up to the third decimal place. Within the precision of the employed method a correction for the lost electron mass in the ionized particle appears not to be necessary.

7.3 Target Properties

The target properties are important parameters in the analysis of the obtained cross section data for any nuclear reaction. The total thickness of the target is an important input parameter to calculate the energy loss, which goes linearly into the calculation of the resonance strength. Furthermore, the density in the center should be high enough to assume that a narrow resonance reaction takes place within a limited slice of gas. This will ensure that the position dependent detection efficiency of the BGO array is well known and the angular acceptance of the recoils may be calculated with a straightforward geometrical approach. In order to calculate the relation between observed yield and resonance strength for a thick target experiment, only the energy loss per unit length and the charge state distribution of the outgoing recoils have to be carefully determined.

The scientific program also includes broader resonance reactions or non-resonant cross sections, where the thick target approximation is not valid and the observed yield rate is geometrically spread over the full length of the target. Therefore, the detection efficiency varies with the position along the beam axis. The first DRAGON experiment involved a resonance in $^{21}Na(p,\gamma)^{22}Mg$ with a total width comparable to the total target thickness. Thus, the measured data will need to be described by folding the detection efficiency of the system, the cross section of the reaction and the density distribution of the target. A knowledge of those parameters to an accuracy of at least 5% is required to reach sufficient accuracy for the complete experiment.

In the following, studies to understand the target density profile and the total target thickness will be presented. Since the maximum angular cone for the outgoing recoils is defined by the pumping tubes, tests on the angular acceptance had to be performed.

7.3.1 DRAGON Gas Target in Detail

The DRAGON gas target is windowless, differentially pumped (fig. 13 and 14) and typically runs in recirculation, with a cooling trap providing gas purity. Normally, hydrogen or helium gas is used with central pressures of the order of 4.5 Torr, while during the commissioning of the DRAGON various pressures between 0.5 and 10 Torr were used.

The central target section has a geometrical length of 11.02 cm and is limited by apertures of 6 mm diameter at the upstream and 8 mm diameter at the downstream side. Looking into the direction of the beam, the holes appear to be round, though they are actually elliptical with the surface slanted by 30 degrees. This geometry helped in decreasing the pressure in the subsequent pumping stage, as it avoids direct gas jets streaming from the inner target cell into the adjacent pumping tubes. The inner target cell is placed in a rectangular box, that contains a tube leading the gas into the inner cell, the mounting

tubes for the two silicon detectors as well as several electrical feedthroughs (fig. 13). From the bottom of the box the gas is pumped out by a series of Roots blowers. One tube to each side along the beam path connects the target box to the adjacent differential pumping stage. From there the gas is pumped via 3 additional pumping stages at the upstream side and 4 stages on the downstream end, each separated from the next one by an additional collimator tube with gradually increasing diameter (fig. 15). The differential pumping leads to a pressure decreasing to 10^{-6} Torr at the connections to beam line and mass separator. The pressures in each stage are measured by ionization and convection gauges, showing that the gas density in the square target box is usually around 0.35 Torr, for typical target pressures of 4.5 Torr in the inner cell under normal operation.

7.3.2 Target Profile

The gas target profile was measured using a non-resonant region of the $^1H(^{15}N, \alpha\gamma)^{12}C$ cross section at 1.45 MeV/u [ROL74]. Scanning the yield, a γ-detector with a slit width of 0.95 cm was moved parallel to the beam axis over a length of 16 cm, limited by the geometry of the adjacent pumping stages (fig. 22). Here, the yield of the 4.4 MeV γ-rays along the beam axis only depended on the gas density observed by the single collimated BGO detector within the effective target interval of 1.65 cm. To avoid errors due to beam instabilities the response curve was normalized to the yield in the elastic scattering monitor at 55 deg for each individual data point.

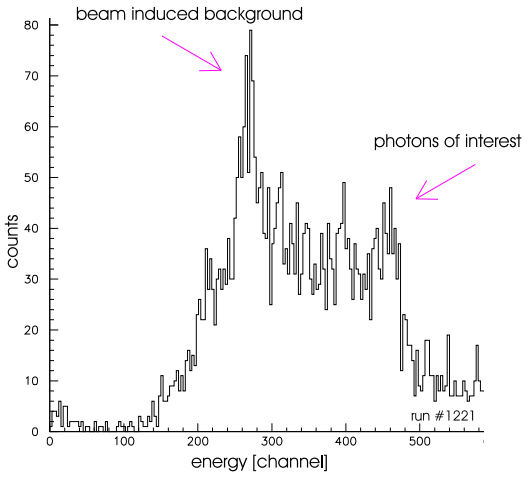

Figure 29: Typical gamma energy spectrum for $^1H(^{15}N, \alpha\gamma)^{12}C$ at 1.45 MeV/u

Significant beam-induced background hampered the measurement especially in the outer target regions, where the γ-yield was reduced due to low gas density (see fig. 29). The background contribution caused a broad peak in the γ-ray spectrum around 2.6 MeV, showing the same time relation to the rf-signal as the γ-rays of interest. Plotting the intensity of those background γ-rays versus the position of the detector proved their correlation with the target cell apertures at 14.6 cm and 25.5 cm on the mounted scale (fig. 30). It was assumed that heavy ion reactions at the apertures produced neutrons that reacted in the lead shielding, as this part of the background vanished when the lead shields were removed.

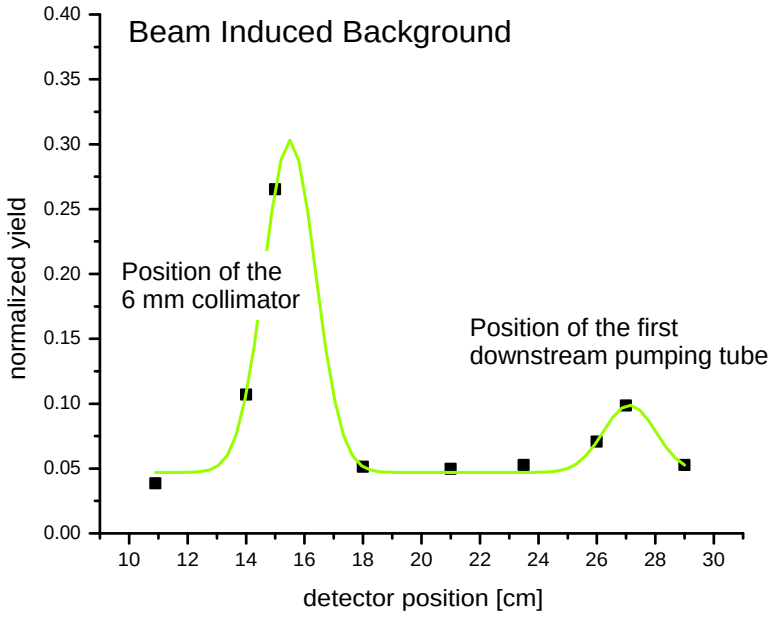

Figure 30: Correlation of the background peak with the position of the detector

The yield curve dependence on the detector position was fitted with

$$y \;=\; P1 \quad [\, atan\,(\frac{x-P2}{P4}) - atan\,(\frac{x-P2-P3}{P4})\,] + P5. \tag{53}$$

which led to a total target length of 10.8 $\pm$ 0.6 cm that dropped over approximately 1 cm from 75% to 25% with edges leading through the gas cell apertures (Fig. 31). The full set of fitting parameters is listed in table 5.

Seemingly, the pressure in the outer box drops to 34% of the inner target cell pressure, which would corresponds to 1.5 Torr for the target box at 4.5 Torr in the cell. The fact

Table 5: Target Profile Fitting Parameters

Parameter	Value	Units
P1	$(2.3 \pm 0.4) \cdot 10^{-4}$	counts/elastics
P2	-14.5 ± 0.3	cm
P3	10.8 ± 0.6	cm
P4	$(5.7 \pm 3.0) \cdot 10^{-1}$	cm
P5	$(3.5 \pm 0.7) \cdot 10^{-4}$	counts/elastics

that this does not agree with the pressure measured to 0.35 Torr by a capacitance vacuum gauge near the pumps of the first stage could be explained by obstacles (i.e. elastic scattering monitors, cables etc.) decreasing the conductivity and thus limiting effective pumping power close to the inner collimator. But this measurement could possibly be faulty at the edges of sensitivity outside of the central target region, where strong beam induced background overpowered the gammas of interest. Therefore, further constrains were required, like the measurement of the total amount of target material, which would allow an estimation of the target gas distribution.

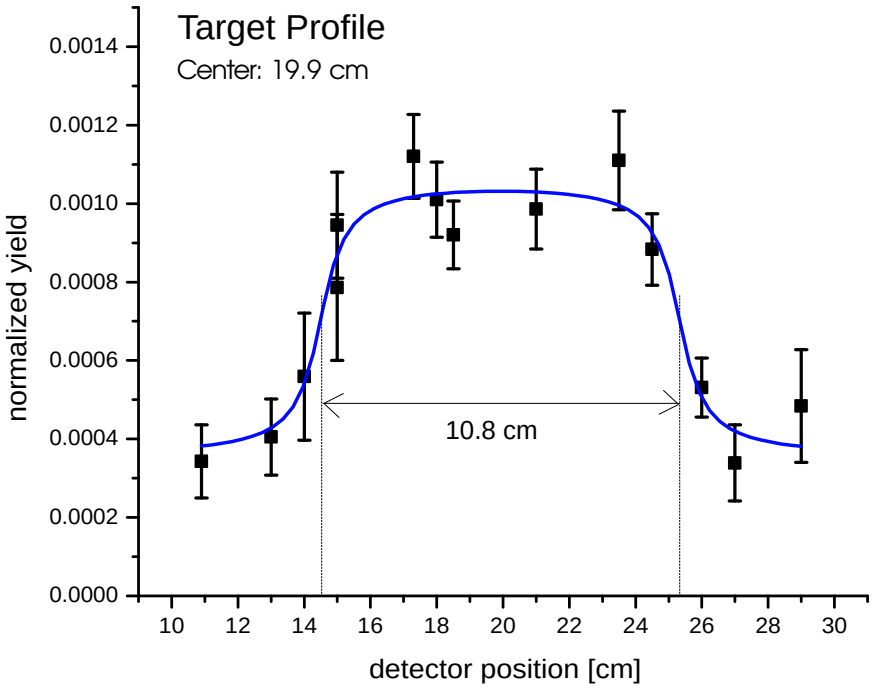

Figure 31: Gas target density profile

7.3.3 Total Target Thickness

In first order, the total amount of target material is linearly related to the energy loss within the target. Most of the target material should be confined within the inner target cell, enclosed with two collimators of 6 mm diameter on the upstream side and 8 mm downstream of the center. However, some gas is leaking out into the adjacent pumping stages. The total energy loss, and therefore the total amount of target material, can be measured by using the energy calibration of the first magnetic bender. Yet, more interesting with regard to the density distribution is the energy loss, or amount of target material, confined within the inner cell. To determine that fraction the energy of the outgoing beam relative to the target pressure was measured with a ^{21}Ne beam at 275 keV/u for two different set-ups (fig. 32): first with the normal set-up within a pressure range from 0 to 4.65 Torr, and then again, in a range from 0 to 9.95 Torr, with the two confining collimators of 6 and 8 mm replaced by smaller apertures of only 1.5 mm diameter each. This reduced the open aperture area to 4.5 % of the original size.

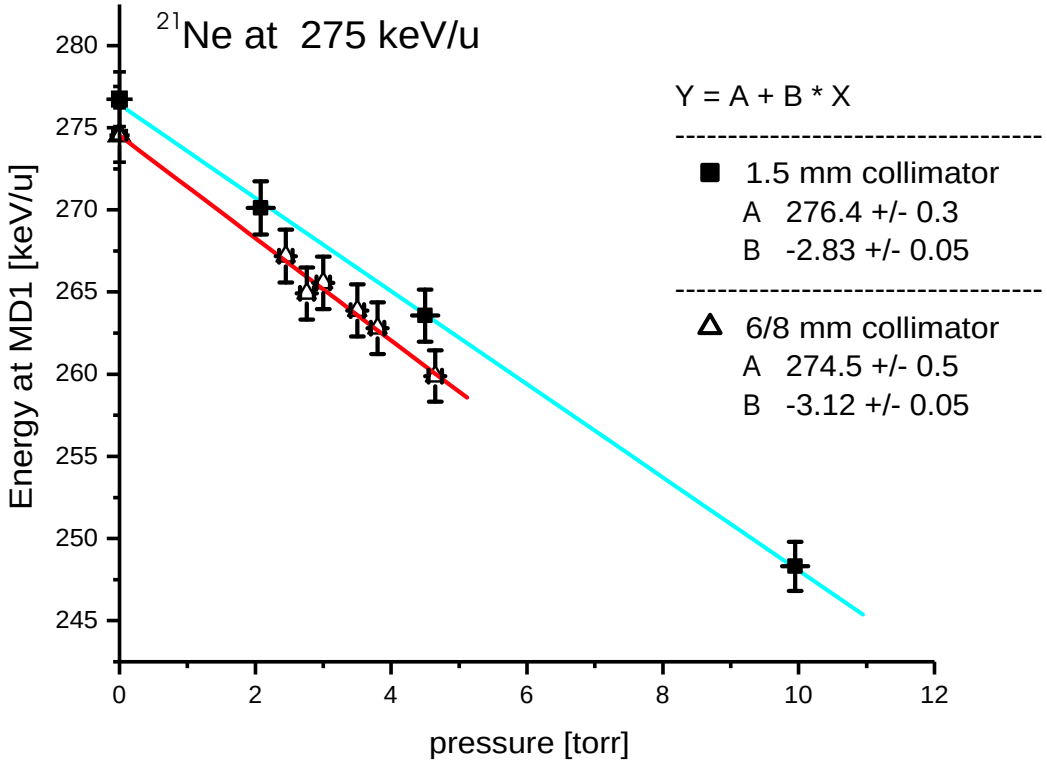

Figure 32: Measurement of total target thickness

The total energy loss ΔE within the target may be understood as the sum of energy loss inside the inner cell ΔE_c and the energy loss due to rest gas leaking out of the cell ΔE_l

$$\Delta E \;=\; \Delta E_c + \Delta E_l. \tag{54}$$

Though it may not be assumed that ΔE_c is independent of the aperture, it can be argued that the effective width of the energy loss in the inner target cell is. This means that the steepness of the edges in figure 31 changes with the size of the confining collimators; however, the effective length does not. Thus, the total energy loss remains the sum of both, the energy loss within the central target material plus contributions from the gas leaking further into the differential pumping system. The first, ΔE_c, is the same in either set-up, while the latter, ΔE_l, is proportional to the open area of the aperture, in first order approximation.

$$\Delta E_l(6/8) \;=\; \Delta E_l(1.5) \cdot \frac{(6^2 + 8^2)}{2 \cdot 1.5^2} \;=\; 22.22 \cdot \Delta E_l(1.5) \tag{55}$$

As indicated in figure 32 the total energy loss ΔE is 3.12 ± 0.5 keV/(u Torr) and 2.83 ± 0.5 keV/(u Torr) for the regular set-up and the variation with the 1.5 mm collimator, respectively. Therefore, from equations (54) and (55) it may be concluded that the difference in energy loss is due to the much higher amount of gas leaking out of the target cell in the regular set-up and only 2.82 ± 0.5 keV/(u Torr) is lost in the actual cell.

7.3.4 Target Gas Distribution

As shown in figure 31 the target density distribution has a flat plateau in the center with a half maximum width (10.8 ± 0.6 cm) corresponding to the geometrical width of 11.0 cm. The amount of target material in an area of 11.0 cm length and approximately constant pressure may be calculated according to formula (31). Thus, for typical pressures of 4.5 Torr and target temperatures of 300 K, the amount of target atoms is n = $3.19 \cdot 10^{18}$ at/cm^2 in the plateau region. However, additional contribution comes from target material outside the inner apertures, where the pressure might change drastically over a short range. Important is the total amount of target material. Therefore, it has proven convenient to calculate an effective target length. This is the length of a step-function like density profile, with a height equal to the central density, and a length that covers also the contributions from the outer edges. The effective target length is then

$$l \;=\; \frac{3.12}{2.82} \cdot 11.0 \quad or \quad l \;=\; 12.2 \pm 0.2 \quad cm.$$

With respect to the target profile it may be concluded that the gas outside the target cell contributes with

$$1 - \frac{2.82}{3.12}\% \quad or \quad 9.6 \pm 2.2 \quad \%$$

to the total amount of target material.

Given the fact that the pressure profile measurement indicated that the pressure drops less rapidly than assumed, most of the rest gas should exist in close geometry with the inner cell. Figure 15 shows that at the adjacent pumping stages are each connected through extended collimators, starting at 8 cm upstream and downstream of the center. Here, at 11.9 cm and 27.9 cm, respectively, on the arbitrary scale of the moving cart, the target profile (fig. 31) shows a pressure of roughly 30 % of the central value, which might be due to jet like gas flows out of the cell. However, since the orientation of inner collimators is inclined towards the beam axis, this flow should be deflected from the adjacent pumping tube, so that the pressure should cease rapidly after this point.
Accordingly, it may be assumed that the target is confined within an 16 cm long range in between to two inner pumping tubes with a plateau region of maximal pressure and an effective width of 11 cm, containing 90.4 ± 2.2 % of the total gas.

7.4 Transmission through the Pumping Stages

Due to the prompt de-excitation gamma, the recoiling ions leave the target at a slight angle to the beam axis (eq. 36). Therefore, the DRAGON experiment was designed to accept ion angles up to ±20 mrad. The limiting factors are the tubes of the differential pumping system of the gas target, designed as small as possible to obtain optimal pressure reduction. Assembly problems and heavy construction work outside the experimental hall were suspected to cause misalignment of the tubes, leading to a reduced angular acceptance. Therefore, it was decided to measure the transmission from the target through the pumping tubes into the DRAGON separator.

7.4.1 Experimental Set-Up

The tests of the optical properties of the DRAGON recoil separator were done with a ^{20}Ne beam of charge state 4^+ and an energy of 200 keV/u. To confine the incoming beam, the gas target box was replaced by a single 3x3 mm^2 aperture, sitting in the center of the former inner cell. Two sets of magnetic steerers mounted on the outside made it possible to introduce an angle a or b to the outgoing beam of up to 20 mrad in each of x and y direction (fig. 33). 50 A current in the steerer corresponded to an angular deviation of 10 mrad.
Then the beam intensity compared to FC4 was measured as a function of a and b at various Faraday cups along the DRAGON beam line, starting with FCCH (fig 17). A beam monitor following the first two quadrupoles Q_1 and Q_2, in a straight line from the gas target, was used to check for significant beam intensity losses ahead of the bender. Yet, exact current measurement was only possible at Faraday cup FCCH, subsequent to the first magnetic bender MD_1, since the beam monitor had no electron suppression.

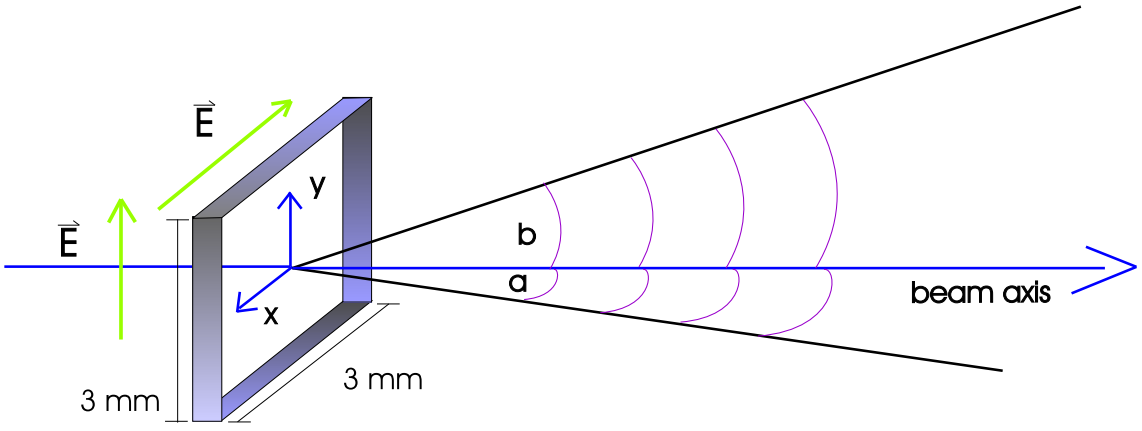

Figure 33: Sketch of the 3x3 mm^2 aperture and the deflection of the outgoing beam

7.4.2 Angular Acceptance

The measured angular acceptance is shown in figure 34. As expected the acceptance curve displays a plateau region with almost full transmission over ± 17 mrad. From here, steep edges indicate a sudden drop to zero transmission over a few mrad. Apparently, during the tests, the incoming beam showed a small angular offset of +2.6 mrad for angle a and +4.3 mrad in angle b. This is due to the fact that the beam angle was only confined by the pumping tubes and the 3x3 mm^2 aperture in the target center. This effect should, in principle, simply shift the acceptance curve and was therefore accounted for.

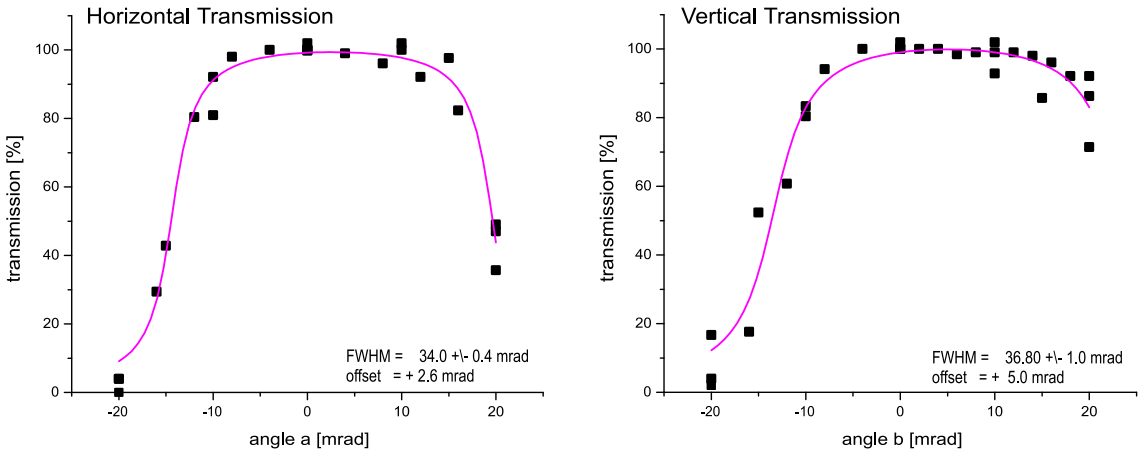

Figure 34: Transmission through the pumping tubes of the gas target

The transmission curve was fitted with a double arctangent function (table 6):

$$t_{a,b} \;=\; P1 \cdot [\, atan\,(\,\frac{x - P2}{P4}\,) - atan\,(\,\frac{x - P2 - P3}{P4}\,)\,] \;+ P5\,. \tag{56}$$

Table 6: Fitting Parameters for Angular Transmission

Parameter	Transmission a	Transmission b	Units
P1	33.9 ± 0.6	35.3 ± 1.0	%
P2	-14.4 ± 0.3	-13.4 ± 0.4	mrad
P3	34.0 ± 0.4	36.8 ± 1.0	mrad
P4	1.8 ± 0.3	2.9 ± 0.5	mrad
P5	0	0	%

Though the pumping tubes were designed for a 20 mrad half angle, it can be seen that the full width of half maximum allows only 34.0 ± 0.4 mrad or 17.0 ± 0.2 half angle in the

horizontal plane and 36.8 ± 1.0 or 18.4 ± 0.5 mrad in the vertical plane. For angle a, the transmission curve rises from 25 to 75% over 3.3 mrad, while in b the rise from 25 to 75% expands to over 5.1 mrad. 95% transmission or more is obtained for half angles of $\pm$ 11.0 mrad in a and $\pm$ 10.6 mrad in b.

It should be noticed that the unexpectedly low angular acceptance should not be related to the emittance of the incoming beam. Any deviation from a "pencil" beam causes the edges of the acceptance curve to smear out. However, this should not affect the plateau significantly. The reason, here, is most likely related to misalignment. Since the first scientific experiments did not require the full angular acceptance, it was left to future plans to re-align the pumping tubes or to consider replacements.

7.4.3 Calculated Transmission

For recoils from reactions with wider opening angles due to the prompt gamma emission, folded with straggling in the target and the emittance of the incoming beam, the transmission has to be calculated individually. Apart from the total excitation energy that is released via a γ-emission, especially the angular distribution of the prompt gammas and their apportionment among possible cascades will influence the combined transmission probability. Further simulations are particularly required if the recoils should be measured in coincidence with the gamma de-excitation. In this case the gamma detection efficiency in the BGO array is correlated with the recoil transmission probability and may not be regarded as an independent normalization parameter.

For the simple case of a single 100% gamma branch to the ground state the transmission probability will be discussed. It shall be assumed that the incoming beam ions do not have any initial angular or energetic deviation from the central value. The ion energy at the resonance E_{lab} is given in keV/u, the energy of the emitted gamma is E_γ given in keV and the de-excitation gammas are emitted under an isotropic angular distribution. Figure 8 shows the dependence of the recoil cone angles a and b on the direction of the emitted gamma.

The maximum recoil angle may be calculated according to equation 36 for a gamma emission in the direction of the x or y axis. For all other possible emission angles, the projection of the gamma momentum p_γ to both x and y axis is the relevant factor (fig. 35):

$$p_\gamma(x\ pro) \ = \ p_\gamma\ cos(\theta)\ cos(\phi) \tag{57}$$

$$p_\gamma(y\ pro) \ = \ p_\gamma\ cos(\theta)\ sin(\phi) \tag{58}$$

Therefore the recoil angles a and b may be parameterized as

$$a \;=\; 0.733\,\frac{E_\gamma\; sin(\theta)\; cos(\phi)}{\sqrt{E_{lab}\; m_p}} \tag{59}$$

$$b \;=\; 0.733\,\frac{E_\gamma\; sin(\theta)\; sin(\phi)}{\sqrt{E_{lab}\; m_p}}\;. \tag{60}$$

Thus, the transmission probability $T_{a,b}$ through the pumping tubes is simply the double integral of the recoil angles a and b multiplied by their individual transmission functions $t_{a,b}$ over all possible gamma emission angles θ and ϕ:

$$T_{a,b} \;=\; \frac{1}{\frac{3}{4}\pi^2}\int_0^{2\pi}\int_0^{\pi} t_{a,b}\;\; sin(\phi) d\phi\, d\theta \tag{61}$$

and, assuming that there is no correlation between a and b acceptance,

$$T \;=\; T_a\; T_b. \tag{62}$$

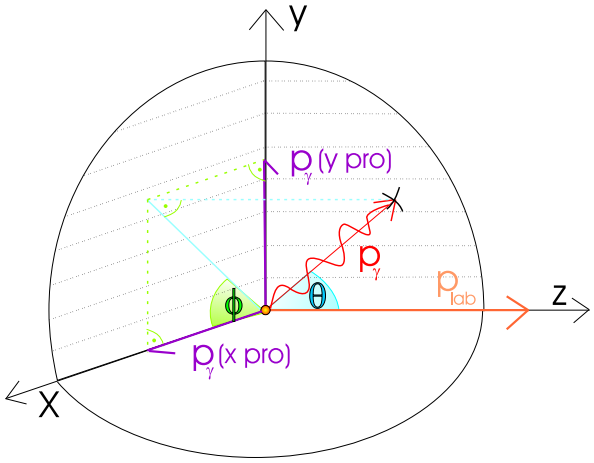

Figure 35: Projection of gamma ray momentum onto x and y axis

The above integral was solved numerically and, in the following, the average transmission for all possible recoil angles, weighted by their distribution, was taken into account in the data analysis. For all studied reactions the transmission was calculated to be better than 99%, except for the $^{21}Ne(p,\gamma)^{22}Na$ reaction at $E_{cm} = 258.6$ keV, which had a recoil cone half angle of almost 15 mrad.
The possible error due to the angular distribution of the beam, decreasing the transmission, was estimated by calculating the transmission for a 5 mrad wider opening cone. This effect was marginal and less then 1% for most of the runs discussed in the following, which, except for this one case, had recoil cone angles smaller than 10 mrad. Cascades in the de-excitation would have the opposite effect, increasing the transmission.

7.5 DRAGON Ion Optics

The DRAGON recoil separator was designed using elaborate ion optical calculations, such as GIOS [WOL87] and simulations like Raytrace [KOW87] and GEANT [BRU94]. While GIOS is an optimization program describing the transport of the ions from one point to the next using Taylor expansion up to the third order from a central trajectory, Raytrace and GEANT are Monte Carlo based programs that follow the trajectories of single ions through an optical system. All bending and focussing elements were carefully calculated, fabricated and their fields mapped before mounted in the DRAGON set-up. Thus, the effective length and fringe fields derived from measurements could be taken into account for the calculations. Still, it seemed reasonable to measure the most important properties directly.

The DRAGON recoil mass separator is characterized by its focus properties at the image points following the magnetic and electrostatic dipoles. Therefore, the aim was to compare the properties of the beam at three ion optical image points along the DRAGON separator with the expected values obtained from theoretical calculations.

7.5.1 Experimental Set-Up

For comparison of realistic beam optics and theoretical calculations the position of the beam centroid was measured at three different image points (fig. 17) along the DRAGON recoil mass separator. With the set-up described in the previous section (fig. 33) additional angles were introduced to the outgoing beam at the target center, varying from -15 to 15 mrad. Also, the energy of the beam was changed in the accelerator, covering deviations from the central energy in steps of 1% from -3 % to +3 %. The moveable charge, mass, and final slits were employed to scan the transverse beam profile both in the vertical and horizontal direction, while measuring the current in the subsequent Faraday cup. Thus, the dependence of the centroid position in horizontal and vertical dimension was studied for all combinations of angle and energy deviation. For the measurements the slit width was set to 1 or 2 mm, while the slits were stepping through the beam in both transverse directions in steps of 1 or 2 mm, respectively. From the measurements first and second order matrix elements for all three image points could be deduced and compared to the GIOS predictions.

7.5.2 GIOS Predictions & Comparison with Reality

Focal planes, where characteristically the beam centroid position is independent of the outgoing angle from the gas target, are expected at the position of each slit pair in x-direction. In the y-direction only small dispersion is expected at the charge slits, while an image is designed for the final slits. Apart from higher order aberration effects energy dispersion

should, in first order, only affect the horizontal x position. The results obtained from the tests are summarized in table 7 and listed together with the calculated GIOS predictions. As it turned out during these tests, the first quadrupole Q_1 was slightly mistuned in the beginning. Increasing its value by 10% improved the focus properties at all subsequent image points. Therefore both, the old and the improved DRAGON tune are shown in table 7.

Table 7: Measured Ion Optics Matrix Elements Compared to Calculated Values

		Old Tune	New Tune	GIOS Tune
Q-slits	$(x\|a)$	-0.175	-0.005	0.000
	$(x\|d)$	0.255	0.250	0.302
	$(x\|aa)$	-15.610	-15.5	-14.488
	$(x\|bb)$	-2.126		0.493
	$(x\|da)$	0.000	2.344	0.302
	$(y\|b)$	0.695	-0.085	0.018
M-slits	$(x\|a)$	0.309	0.006	0.000
	$(x\|d)$	-0.002	0.002	0.000
	$(x\|g)$	-0.489	-0.489	-0.472
	$(x\|aa)$	2.740	0.110	0.180
	$(x\|bb)$	5.894	0.236	-0.412
	$(x\|da)$	0.000	0.000	-0.425
	$(y\|b)$	-0.697	-0.139	-0.430
F-slits	$(x\|a)$	0.602	0.545	0.000
	$(x\|d)$	0.042	-0.006	0.000
	$(x\|g)$	0.000	0.000	-1.828
	$(x\|aa)$	10.878	9.100	4.007
	$(x\|bb)$	1.400	0.977	-0.029
	$(x\|da)$	0.000	6.925	-0.731
	$(x\|dd)$		0.593	-3.548
	$(y\|b)$	0.182	-0.060	0.000

Since the table does not provide an intuitive picture, the obtained results are illustrated in the following: For an ion beam with a round cross section of 4 mm diameter in the center of the gas target and an opening cone of 10 mrad the xy-projections were calculated according to GIOS and compared with measured data. In addition, the effect of the relative energy deviation d from the central value by ±2% was graphically emphasized. Effects of linear magnification were not yet experimentally verified, but included in the figures for a more realistic picture. If the energy spread is kinematically related to the angular distribution, the plotted ions would lie on an ellipsoid described by $(a^2 + b^2 + d^2/4)^{1/2} = 0.01$. Yet here, all angles in the range of 0 to 10 mrad were allowed in combination with all energy

variations. The outline of the resulting spots at the charge, mass and final slits are plotted in figures 37, 38, 39.
As can be seen, the agreement of prediction and measurement is quite satisfying. At all image points, it becomes obvious that the improved tune shows much better properties than the earlier version. For the foci at the charge slits (fig. 37), following the first magnetic bender MD_1, the energy dispersion is quite similar. At the first electric dipole ED_1, the position of the mass slits, the predicted and measured focus properties agree within 1 mm in x (fig. 38). For y the dispersion is even smaller than expected, which helps to minimize additional abberation. At the final slits (fig. 39), following the second electric dipole ED_2, the tune, especially with an extension of 9 mm in x direction, is much broader then predicted ($\leq$ 1 mm). Here, the tune of the last quadrupole doublet defining the focus parameters at the final slits and the following detector were empirically changed during earlier tests to move the focus position farther downstream, thus minimizing the spot size on the detector. Therefore, the observed disagreement at the final slits is well understood. In total, the separation of beam and recoils at the mass slits is quite satisfying and agrees very well with the predictions as can be seen in figure 36.

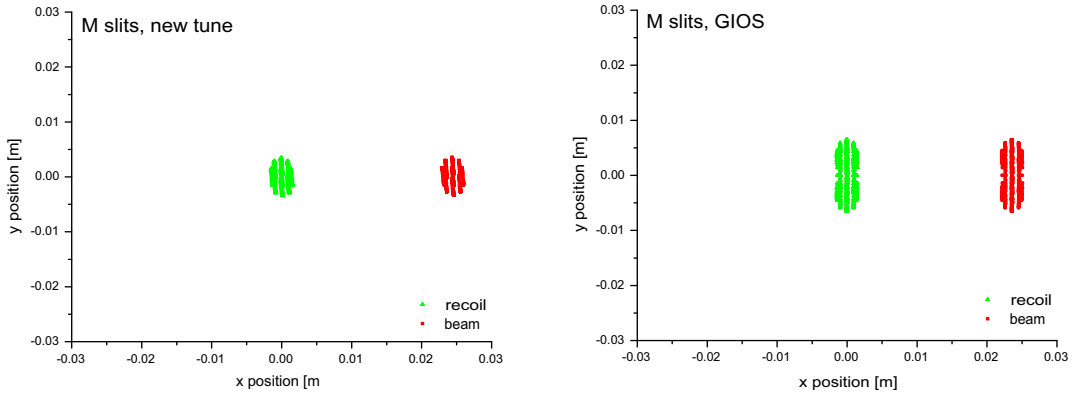

Figure 36: Separation of recoils and beam ions in projection onto the xy-plane at the mass slits for the improved and the calculated tune

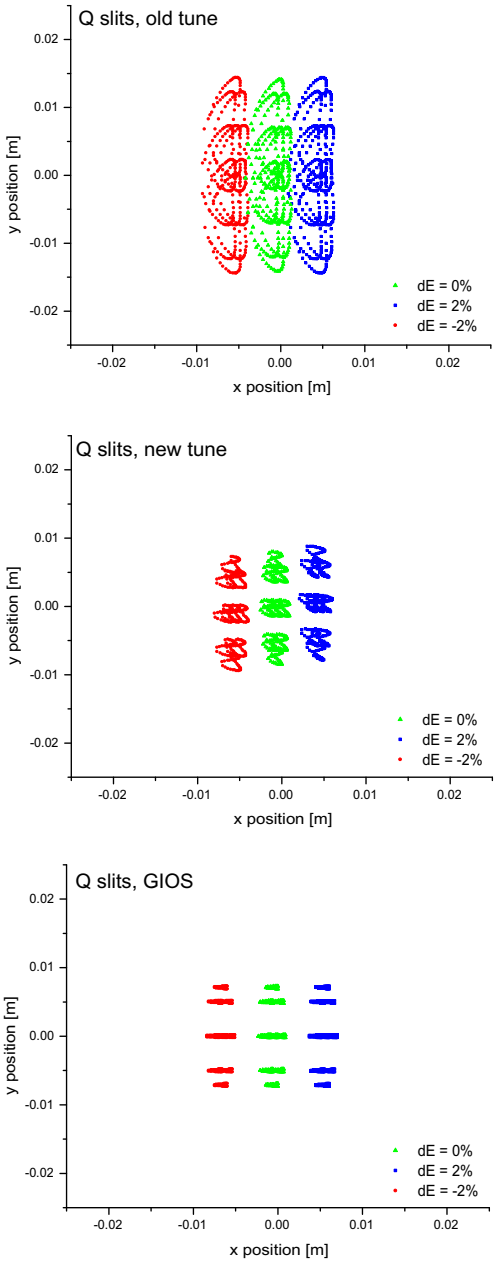

Figure 37: Focus properties of the DRAGON Recoil Separator at the charge slits for the old, the improved and the calculated tune

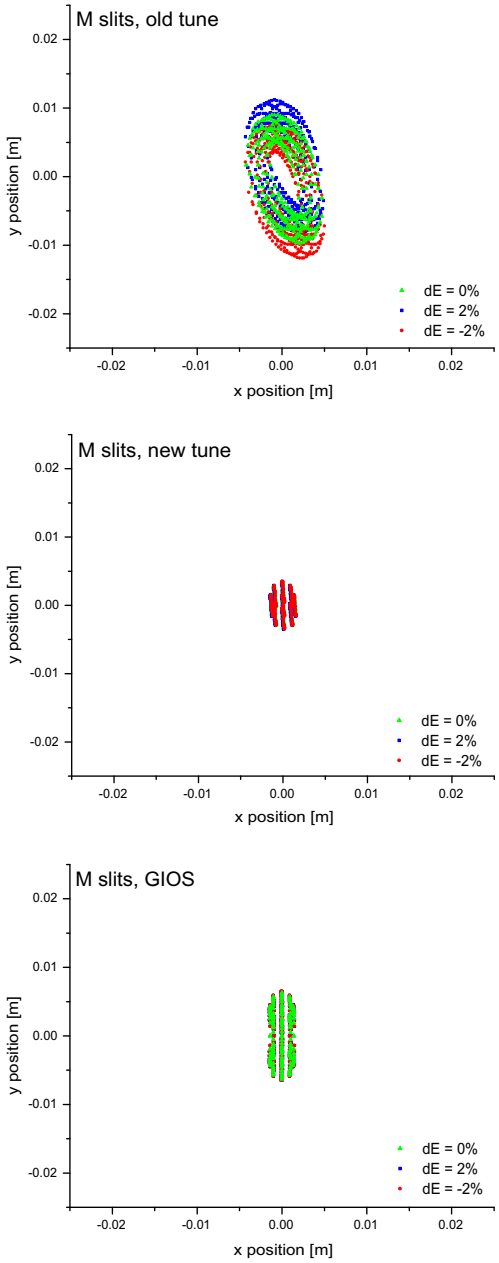

Figure 38: Focus properties of the DRAGON Recoil Separator at the mass slits for the old, the improved and the calculated tune

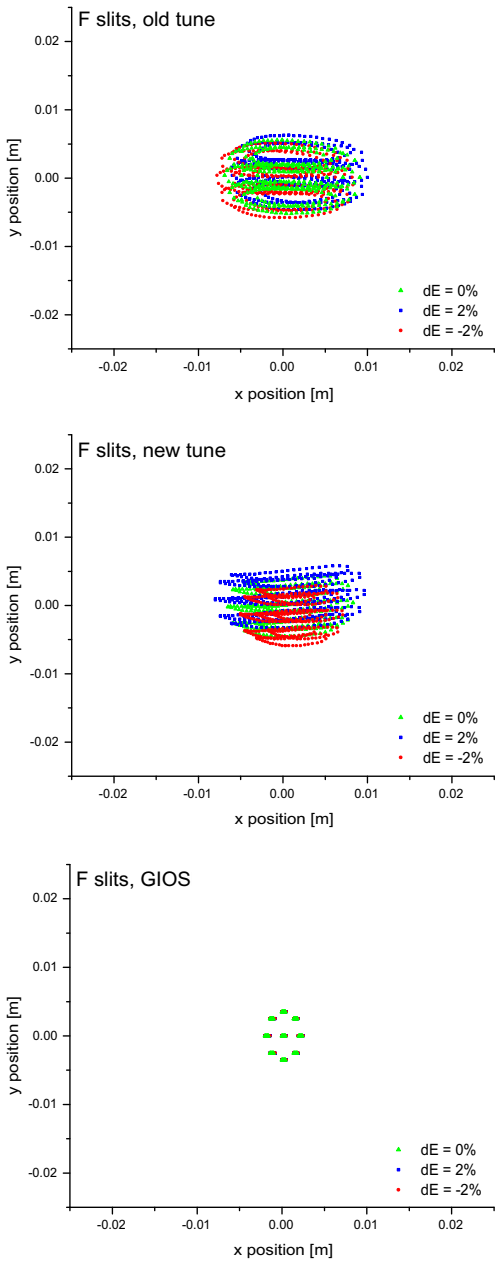

Figure 39: Focus properties of the DRAGON Recoil Separator at the final slits for the old, the improved and the calculated tune

8 Studies of Nuclear Reactions with Stable Beam

As a final test of the DRAGON set-up, a set of previously measured reactions involving stable nuclei was studied. While the aim was mainly to measure the cross sections of a number of reactions with different energies, strengths and widths and to compare the results to the published values, for some reactions the full excitation curve was observed. Thus, the agreement with the energy calibration could also be deduced. In addition, the energy loss in the target was measured and compared to SRIM values [BIE00]. Also upper limits for the beam suppression were derived from the data. When possible, the charge state distribution for the outgoing recoils was measured and the BGO detection efficiency over the length of the target was estimated.
Table 8 gives a list of the stable beam reactions employed with their Q-values, reaction energies [END98], resonance widths and strengths [ANG99] and [POW99], as well as recoil opening cone angles.

Table 8: Stable Beam Reactions Measured at DRAGON

Reaction	Q-Value	E_{cm}	Γ_{cm}	$\omega\gamma$	$\Phi_{1/2}$	m_p	m_t
	keV	keV	eV	eV	mrad	amu	amu
$^{20}Ne(p,\gamma)^{21}Na$	2431.4	1112.6	15.5	1.13	3.8	19.992	1.007
$^{21}Ne(p,\gamma)^{22}Na$	6739.4	258.6	100	0.0825	14.9	20.994	1.007
$^{21}Ne(p,\gamma)^{22}Na$	6739.4	731.5	4000	3.95	9.4	20.994	1.007
$^{24}Mg(p,\gamma)^{25}Al$	2271.3	214.0	< 32	0.0127	5.1	23.985	1.007
$^{24}Mg(p,\gamma)^{25}Al$	2271.3	402.2	0.19	0.042	4.0	23.985	1.007
$^{24}Mg(p,\gamma)^{25}Al$	2271.3	790.4	1300	0.64	3.3	23.985	1.007

It should be noted at this point that, contrary to initial intentions, the high beta buncher in the HEBT accelerator line was not always used for the following runs. Therefore, it has to be assumed that the beam properties were still as measured before, with beam energy spreads of the order of 2 keV/u for a good tune. However, it should be remembered that the beam energy spread can be up to 7 keV/u. For future records it should be mentioned that in later tests, not considered in the present work, it was observed that the buncher decreased the energy spread, but also increased the beam energy significantly compared to the value claimed by the ISAC operators, as they measure the beam energy upstream of the buncher. Since the DRAGON is situated downstream of the high beta buncher, the energy measurement with MD_1 is not affected.

8.1 DRAGON Tuning Procedure

Once the desired beam was delivered by the ISAC operation team, the properties of the beam were checked. Normally, if the magnetic rigidity $\frac{mv}{q}$ was within the acceptance of the first magnetic bender, MD_1 was used to measure the incoming beam energy with an empty target. In particular, the angular properties of the incoming beam were evaluated to exclude incoming angles larger than 1 mrad. For this purpose the first leg of the DRAGON separator was tuned by adjusting the first two quadrupoles to the nominal magnetic rigidity, while MD_1 was fine tuned, so that the beam was centered on the charge slits. Switching the first two quadrupoles off and on, the beam position on the charge slits was not allowed to move by more than 3 mm. This limited possible steering effects of Q_1 and Q_2, and therefore, significant deviation of the beam trajectory from the central axis. Subsequently, all magnetic elements were scaled relative to MD_1, applying the calculated and experimentally reviewed ratio of field strengths. A computer based program called EPICS [KEI01] allowed to automatically scale all electric and magnetic elements according to a saved reference file, thus, guaranteeing comparable tunes for all runs. For further fine tuning the steerers and the consecutive magnetic and electric benders were adjusted such that the beam was centered on the following monitors and slits up to the focal planes. The settings of all power supplies and both NMR probes were recorded. Finally, the appropriate tune for the recoils could be adapted by scaling the electric dipoles according to the mass ratio of beam and recoils.

The above beam tuning procedure has been proven to be a fairly easy and straight forward approach, even with the use of radioactive ion beams supplied so far, since the sensitivity of the devices was sufficient for the observed beam intensities. In the future, using less intense radioactive beams, stable pilot beams of similar mass and energy but higher current might be used to pre-tune the optical system.

For typical runs, the slits were set to guarantee full transmission of the recoils according to the tests described in the previous chapter. That meant at least 25 mm opening at the charge slits (QX and QY), 15 mm at MX for a sufficient leaky beam suppression, but 25 mm in MY, and almost open slits of 45 mm width in FX and FY just ahead of the final focus. With the final focus shifted downstream from the final slits onto the end detector and the final slits wide open, the second stage of the mass separator was more used for ion transport than for leaky beam suppression. If desired in the future, a more careful tune of the second stage would provide room for further improvement of the overall beam suppression.

8.2 Data Normalization and Systematic Errors

The largest errors involved were in the normalization of the detected events. For the purpose of data normalization, it was intended to measure the beam intensity immediately ahead of every run either at FC4, just ahead of the DRAGON gas target, or at FCCH, subsequent to MD_1, preferably at both. These values were used later as a reference to the elastic monitor count rate. Thus, without knowing initially the exact effective target length observed by the monitor, the beam could be integrated over the course of a run avoiding normalization errors due to fluctuations in the beam intensity or deviations from pure Rutherford scattering.
For each beam energy the rate of elastically scattered protons of the first 300 seconds R_0 was assumed to correspond to the Faraday cup reading just ahead of the run $FC4_0$, normalized to the charge state of the beam. Then the mean beam intensity $FC4_{eff}$ over the full run time t was calculated from the average rate of protons R_{tot} over the run:

$$FC4_{eff} \;=\; FC4_0 \,\frac{R_{tot} \cdot 300}{R_0 \cdot t} \tag{63}$$

For reactions with a weak elastic (p, p') channel, an overall relation of elastics rate to Faraday cup current was obtained. Thus, the error in the normalization was reduced.

The charge state distribution of the recoils leaving the gas target was either measured or calculated according to [LIU02]. While for the measured charge state fraction, the error was purely statistical, for the calculated values an error of 10% was assigned. Besides the selectivity in charge state, the transmission through the separator should be close to 100%, except for losses within the pumping tubes. For the double sided silicon strip detector a total efficiency of $99 \pm 1\%$ [WRE02] was assumed. Therefore, all runs were normalized to the charge state probability, the transmission efficiency, the efficiency of the DSSSD, the dead time in the data acquisition and, if applicable, the BGO detection efficiency. Then, the systematic contribution to the error of the resonance strength was the sum of all uncertainties $\Delta_i = \frac{\delta i}{i}$ in the instrumental errors, plus the error in the energy loss within the target and charge state fraction summed in quadrature. Here Δ_{FC} is the error on the reading of FC4, with δi approximately $\pm$ 10 epA.

$$\Delta\,\omega\gamma \;=\; \sqrt{\Delta^2_{BGO} + \Delta^2_{ch} + \Delta^2_{trans} + \Delta^2_{DSSSD} + \Delta^2_{dE} + \Delta^2_{FC}} \tag{64}$$

The statistical errors are displayed as an error bar for each individual run in the plots and listed separately. Taken into account were the statistical error due to the number of good events $1/\sqrt{N}$ and the normalization of elastics rate to FC4, when done for each individual run. Thus, the statistical error of the measured yield is simply given by the scatter of the data around the fitted or calculated mean value.

If not stated otherwise, the units in the following figures are in channel and counts.

8.3 The $^{20}Ne(p,\gamma)^{21}Na$ Reaction at E_{cm} = 1112.6 keV

For calibration purposes, the full excitation curve around $E_{cm} = 1112.6$ keV [END98] of the $^{20}Ne(p,\gamma)^{21}Na$ [BLO69] reaction was measured at 4.7 Torr target gas pressure with beam currents ranging between 0.6 and 1.3 particle nano Ampere (pnA). The reaction parameters are listed in table 8. For this resonance the recoil cone angle was very small, so that the transmission was calculated to be 99.9 $^{+0.1}_{-0.2}$ %.

As can be seen in figure 40 the recoil energy spectrum in the final DSSSD detector was almost free of leaky beam ions. Except for the reduced efficiency, both recoil energy spectra, in singles mode and in coincidence with a gamma event, were comparable in width and position. Energy degenerated counts at slightly lower energies were observed in both spectra and were most likely due to events measured between two strips in the detector. Therefore, in the analysis, the number of total counts was derived by integration over the energy spectrum, including these points down to channel 10000. Cuts on the energy spectrum were applied such as to integrate over energy degenerated events above the alpha contamination energy and to exclude possible leaky beam ion events by adjusting the high energy cut according to the recoil peak in the coincidence spectrum individually for each run. Events above the energy cut were assumed to be correlated with leaky beam particles.

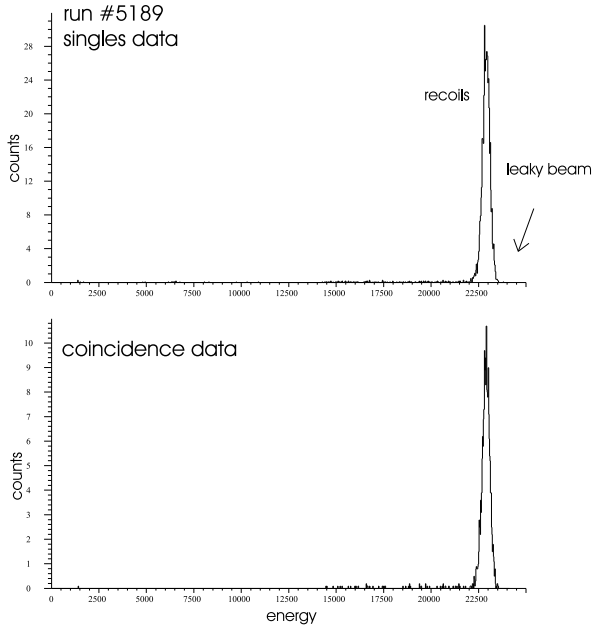

Figure 40: Recoil energy spectra in singles and coincidence mode for $^{20}Ne(p,\gamma)^{21}Na$ at $E_{cm} = 1112.6$ keV

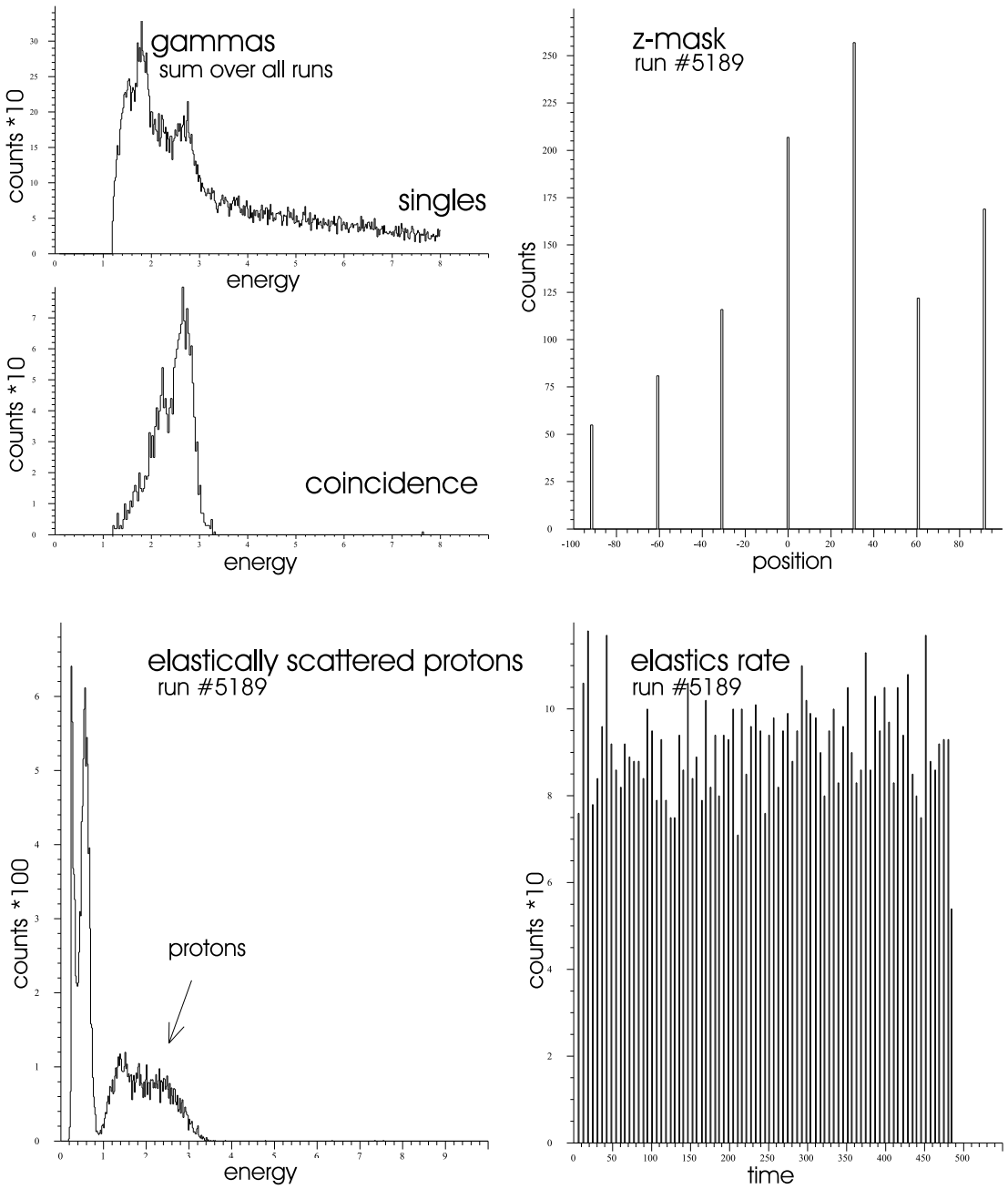

Figure 41: Gamma energy spectrum in singles and coincidence mode with the position distribution of gamma ray events within the target, the elastic energy spectrum and the count rate of the "good" elastics above background for a typical run of $^{20}Ne(p,\gamma)^{21}Na$ at $E_{cm} = 1112.6$ keV

In figure 41 the gamma energy spectrum, summed over all 30 BGO responses, is displayed for single gamma events and for gamma events with recoil coincidence requirements. For the latter, only events with exactly one gamma above a threshold of approximately 1.2 MeV were displayed. The state at 3.54 MeV is known to decay with 96% directly to the ground state (fig. 42) [BLO69]. As expected, the coincidence gamma spectrum clearly shows a strong full energy peak around channel 3000 as well as a second peak about 500 channels lower. The latter so-called single escape peak results from the production of an electron-positron pair in the BGO crystal. If one of the annihilation 511 keV gamma rays escapes from the detector, the recorded energy is reduced accordingly. A small low energy shoulder related to the loss of both particles or Compton scattering can be seen as well. For all runs, the energy spectrum of the elastically scattered protons displayed significant background just below the proton peak, maybe due to a detector failure. But the protons are still clearly distinguishable from the low energy noise. Therefore, intensity fluctuations of the beam were monitored by measuring the rate of the elastic events above noise. This was related to the incoming beam intensity via equation 63.

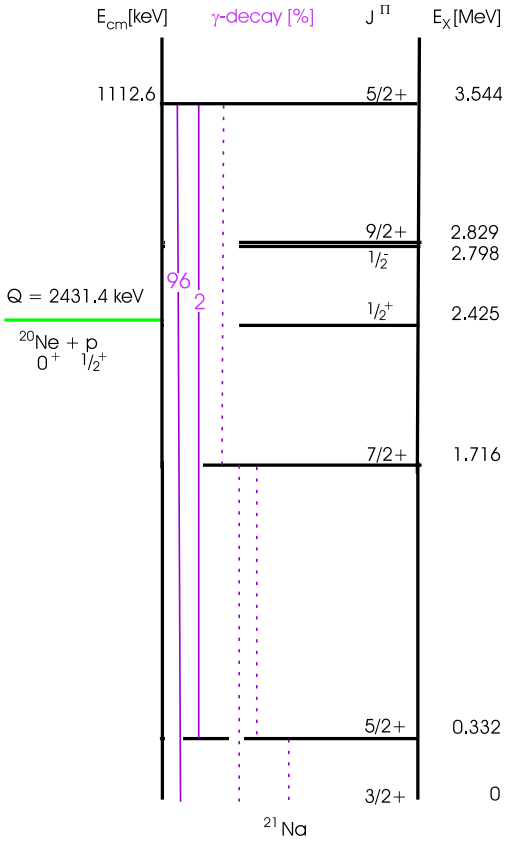

Figure 42: Decay scheme for the ^{21}Na excited state at $E_x = 3.54$ MeV.

From several measurements of the beam energy at various pressures, the beam energy loss was measured as demonstrated with figure 43 to be dE = 2.41 ± 0.29 keV/(u Torr) or

$$dE \;=\; 61.3 \pm 7.5 \quad \frac{eV}{10^{15} at/cm^2} \; .$$

Included in the error is the spread between the individual measurements as well as the uncertainty in the target length. The result agrees with SRIM (56.9 eV/10^{15} at/cm^2) within 9%. The energy loss in the target could also be determined from the width of the excitation curve, which would result in 2.61 keV/(u Torr). However, due to missing data on the falling edge, the beam energy loss measured with MD_1 is presumably more precise.

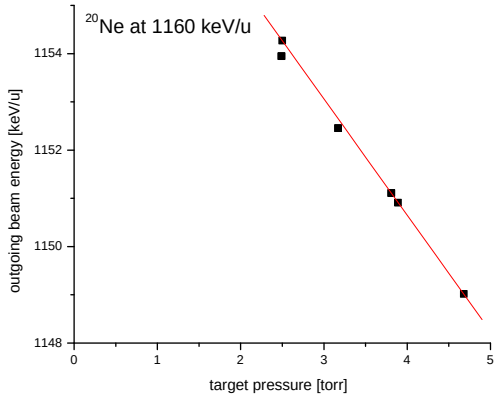

Figure 43: Energy loss measured for the $^{20}Ne(p,\gamma)^{21}Na$ recoils at E_{cm} = 1112.6 keV

For the full excitation curve the number of recoils was normalized to run time, dead time and $FC4_{eff}$ taking into account the 4+ charge state of the incoming beam. The charge state distribution of the outgoing recoils was measured. Varying by more than 10% for several independent measurements, it contributed significantly to the error. Otherwise, the error was only related to the statistical uncertainty of the count rate and a small 5% error in the beam intensity normalization.

Table 9: Charge State Distribution of ^{21}Na recoils at E_{lab} 1100 keV/u

Charge State	Probability	
7+	3 ± 3	%
8+	36 ± 5	%
9+	57 ± 6	%
10+	3 ± 3	%

The full excitation curve is displayed in figure 44. Since the charge state distribution of the recoils may in principle change with the resonance moving towards the end of the target, leaving less and less material for the recoils to undergo charge exchange reactions, the error in the charge state efficiency was taken into account for the fit. The yield was fitted with function 53. Thus, using equation 33 and the measured energy loss, the resonance energy and strength may be calculated.

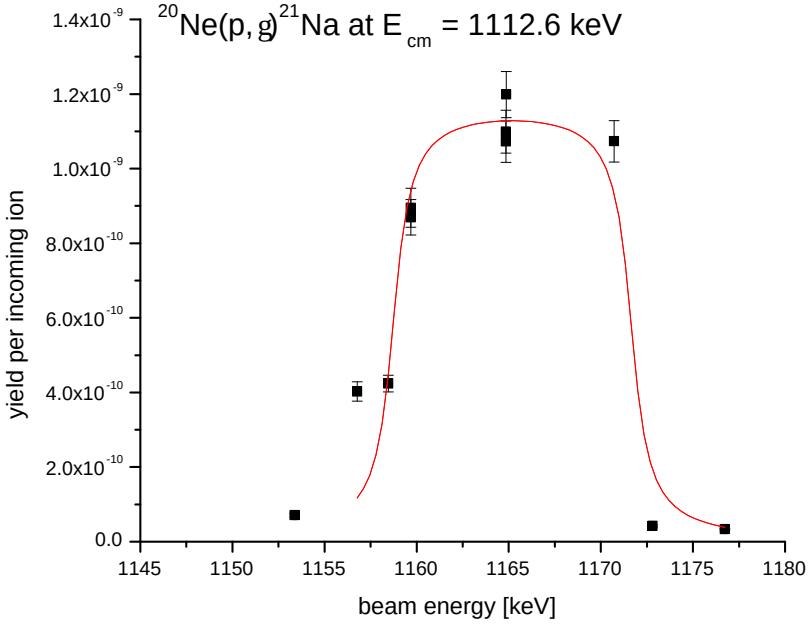

Figure 44: Full excitation curve of the $^{20}Ne(p,\gamma)^{21}Na$ reaction at $E_{cm} = 1112.6$ keV

Table 10: Fitting Parameters of the $^{20}Ne(p,\gamma)^{21}Na$ Yield at $E_{cm} = 1112.6$ keV

Parameter	Value	Units
P1	$(3.87 \pm 0.39) \cdot 10^{-10}$	per particle
P2	1158.8 ± 0.9	keV/u
P3	12.8 ± 1.0	keV/u
P4	0.74 ± 0.34	keV/u
P5	0	

The resonance energy is determined by the inflection point of rising edge of the thick target yield. The value obtained from the fit was transferred into the center-of-mass system.

$$\omega\gamma \;=\; 0.922 \pm 0.090\ (stat.) \pm 0.149\ (sys.) \quad eV$$

$$E_{cm} \;=\; 1110.8 \pm 0.9 \quad keV$$

Also interesting is the performance of the DRAGON recoil mass separator given by the leaky beam suppression. Using the events detected above the recoil energy peak, the suppression was estimated according to

$$S \;=\; \frac{N_{leaky}}{N_{beam} \cdot \varepsilon}. \tag{65}$$

Here, N_{leaky} is the number of leaky beam particles, N_{beam} the total number of incoming beam ions during the period of the run, and ε the overall detection efficiency. In principle the high energy events could also be related to signal pile up. Therefore, the calculated beam suppression factor should be regarded as an upper limit:

$$S \;\leq\; 2.22 \pm 0.05 \cdot 10^{-13}\ .$$

The BGO efficiency for detection of the full energy peak, including the single and double escape peak for a 3.5 MeV gamma, is the ratio of coincidence to singles events. Obviously, it depends on the resonance position within the target and should be plotted compared to the z-mask position (fig. 46) where available. Figure 45 proves that with the current BGO set-up the z-mask feature provides a reasonable measurement of the resonance position as it moves linearly with the beam energy in a range of ± 3 cm from the target center. Because the length of the BGO array (fig. 16) along the beam axis is reduced compared to earlier set-ups (displayed in figure 21), so is the range of the z-mask feature.

At least one of the two events where the position does not agree with the general trend ($E_{lab} = 1156.8$ keV/u) lies also outside the fit of the yield curve. This may be explained by an operator failure to measure the beam energy. Therefore, this point was excluded from the analysis. Thus, the BGO efficiency in the target center was estimated to be

$$\varepsilon_{BGO} \;=\; 42 \pm 4 \quad \%.$$

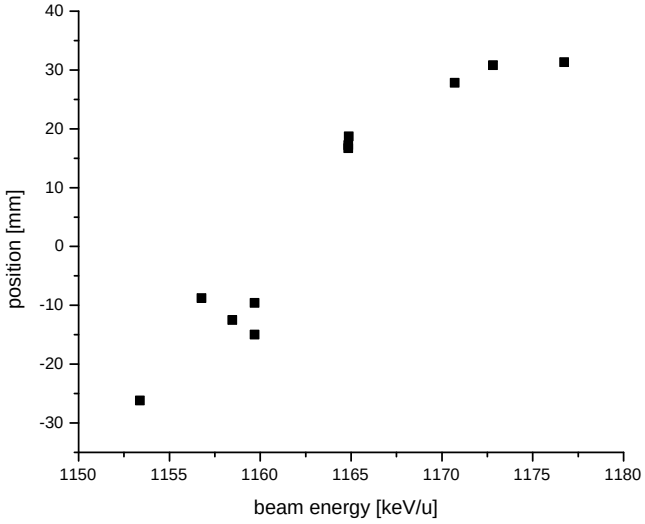

Figure 45: Beam energy versus the position of the resonance (z-mask) for $^{20}Ne(p,\gamma)^{21}Na$ at $E_{cm} = 1112.6$ keV

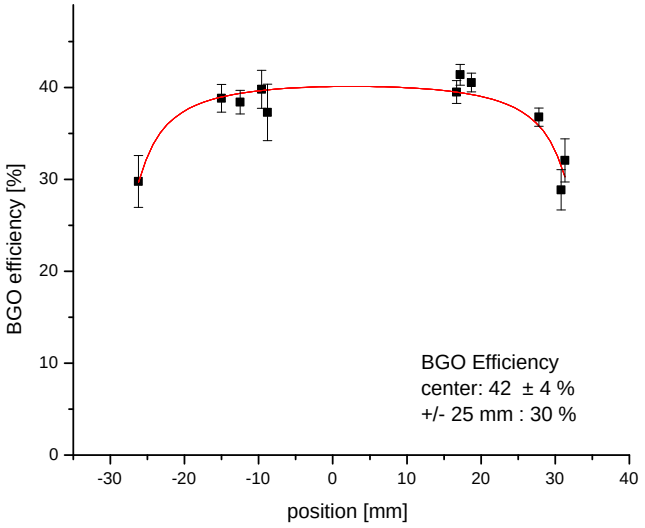

Figure 46: BGO efficiency along the beam axis for 3.5 MeV gammas

8.4 The $^{21}Ne(p,\gamma)^{22}Na$ Reaction at E_{cm} = 258.6 keV

For the $^{21}Ne(p,\gamma)^{22}Na$ reaction at E_{cm} = 258.6 keV [END98] the resonance strength was measured at several different energies without actually mapping the full excitation curve. The pressure was ranging from 4.6 to 4.9 Torr, with typical beam currents of the order of 0.3 to 0.6 pnA. The transmission was calculated to be 97.2 ± 2.5 % and taken into account when the data was normalized and compared to the literature value [GOE82].

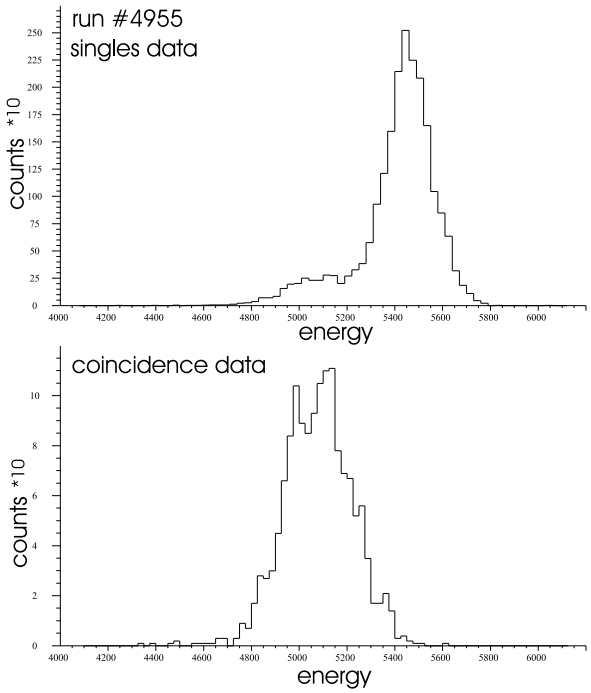

Figure 47: Recoil energy spectra in singles and coincidence mode for $^{21}Ne(p,\gamma)^{22}Na$ at E_{cm} = 258.6 keV

As shown in figure 47, the recoil energy spectrum in the final DSSSD detector was partly covered by a strong leaky beam peak at slightly higher energy. Those leaky beam ions could not be resolved from the recoils of interest in the singles spectrum by a cut on the DSSSD position spectrum or similar attempts. However, the position and expected width of the recoil peak could be obtained from a Gaussian fit to the coincidence recoil energy spectrum. The resulting peak position and width were employed when fitting the weaker peak in the singles event spectrum (fig. 49). Therefore, the singles events could be used and additional systematic error due to uncertainties in the gamma detection efficiency were avoided.

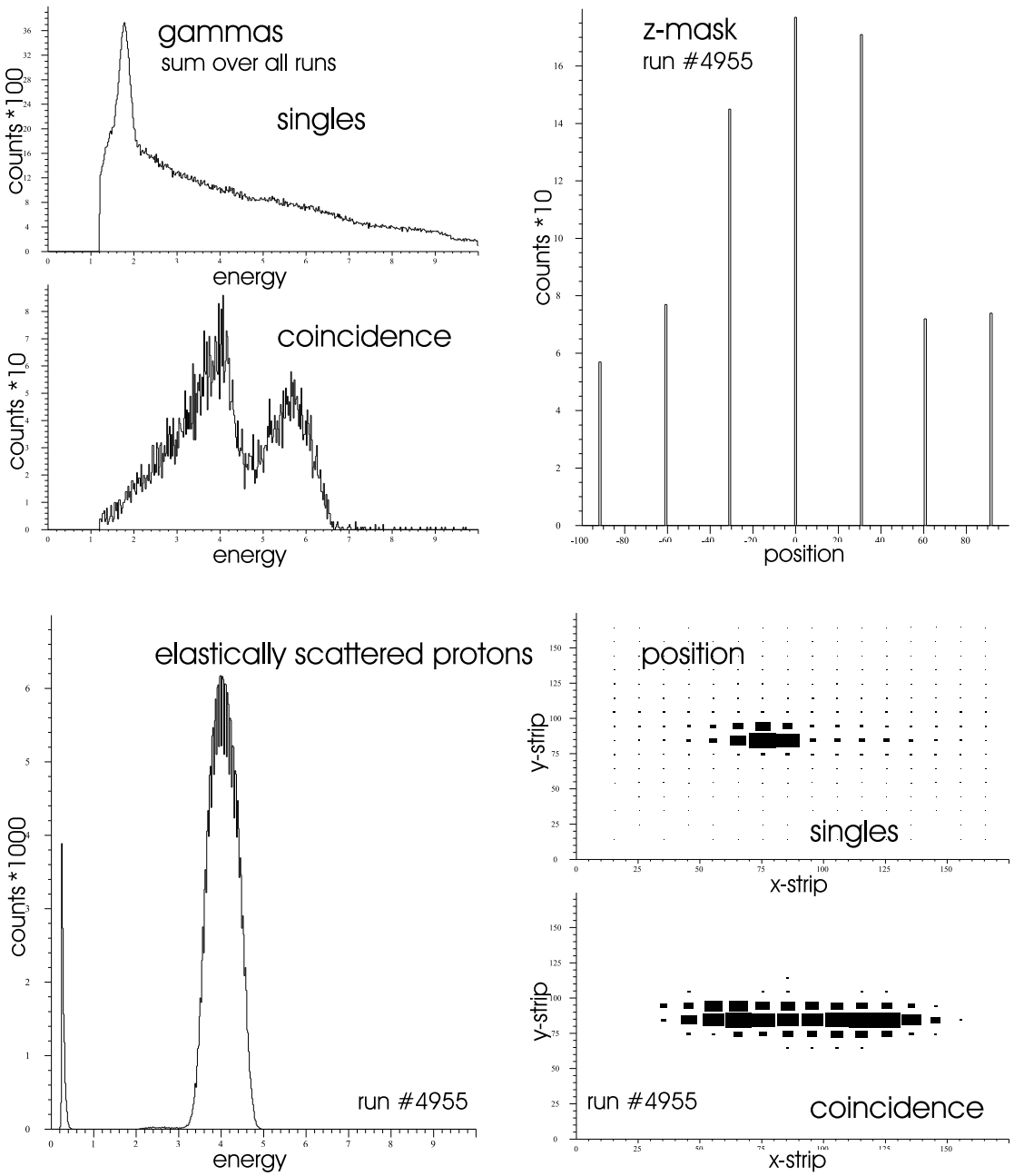

Figure 48: Gamma energy spectrum in singles and coincidence mode with the position distribution of gamma ray events within the target, the elastic energy spectrum and the position distribution of recoils in the DSSSD for a typical run of $^{21}Ne(p,\gamma)^{22}Na$ at E_{cm} = 258.6 keV

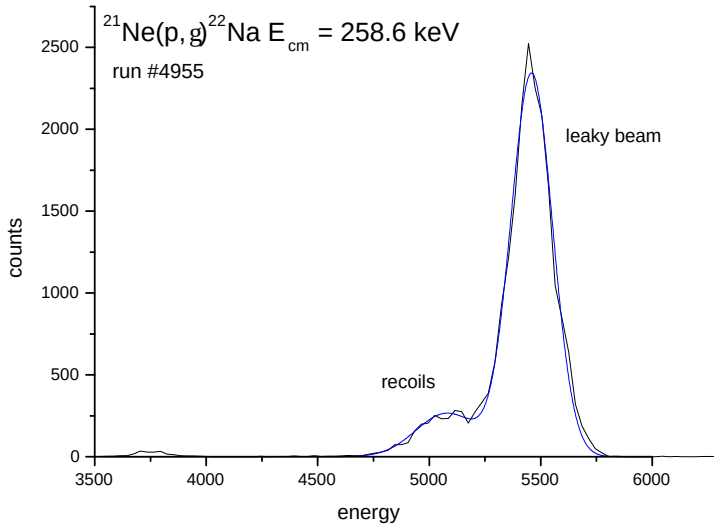

Figure 49: Fit to a typical recoil energy spectrum for $^{21}Ne(p,\gamma)^{22}Na$ at $E_{cm} = 258.6$ keV

Figure 48 displays the sum of all gamma energy spectra for single gamma events and for gamma events with recoil coincidence requirements, both hardware thresholds were set to about 1.9 MeV. For the latter, only events with exactly one gamma above threshold were displayed. The spectrum clearly shows two peaks related to different gamma transitions. Most likely, the high energy peak is related to the ground state transition (branching ration = 51%) observed in [GOE82] leading to a 7 MeV gamma, while the main contribution of the second peak should come from a transition to the excited state at $E_x = 1937$ keV with a 5.1 MeV gamma (29%) (fig. 50). Compared to the gamma energy spectrum in figure 41 both peaks are much broader because of additional weaker branches to other excited states and their cascades which are not resolved here. In total, 95 % of the transitions should have been observable to the BGO array. Yet, a more comprehensive study on the detection efficiency for various gamma ray energies will be part of another thesis [GIG03].

For most of the runs the energy spectrum of the elastically scattered protons was separated from background. Since the resonance was not observable in the elastics channel, an overall relation of elastics count rate towards the current measured at FC4 could be found. Thus, the rate was used for normalization as described in equation 63, together with the run time and dead time.
The charge state distribution was not specifically measured, instead a 35 ± 4% efficiency for a recoil charge state of q = 5+ was derived from [LIU02].

The result of the yield measurements is displayed in figure 51.

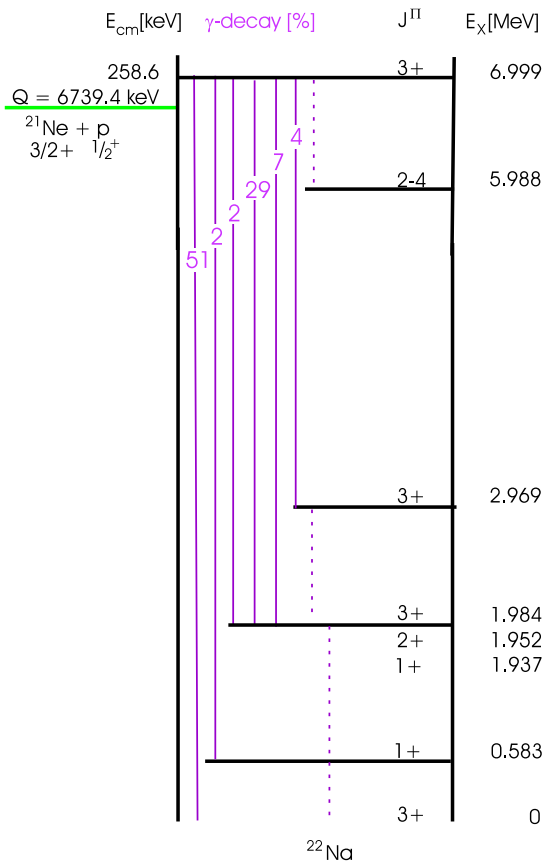

Figure 50: Decay scheme for the ^{22}Na excited state at $E_x = 6.998$ MeV.

In order to obtain a resonance strength, the beam energy was measured, both, with an empty and a gas filled target to determine the beam energy loss in the gas ahead of each run. For two subsequent runs (out of eight in total) the reported beam energies were most likely wrong. Therefore, those runs had to be excluded from analysis. The measured energy loss agreed with SRIM (75.0 eV/10^{15} at/cm^2) within 9%:

$$dE \;=\; 83.0 \pm 3.44 \quad \frac{eV}{10^{15} at/cm^2} \; .$$

From the weighted average yield of $9.15 \pm 0.86 \cdot 10^{-10}$ the resonance strength was calculated with equation 34 and the measured energy loss:

$$\omega\gamma \;=\; 0.209 \pm 0.020 \; (stat) \pm 0.029 \; (sys) \quad eV.$$

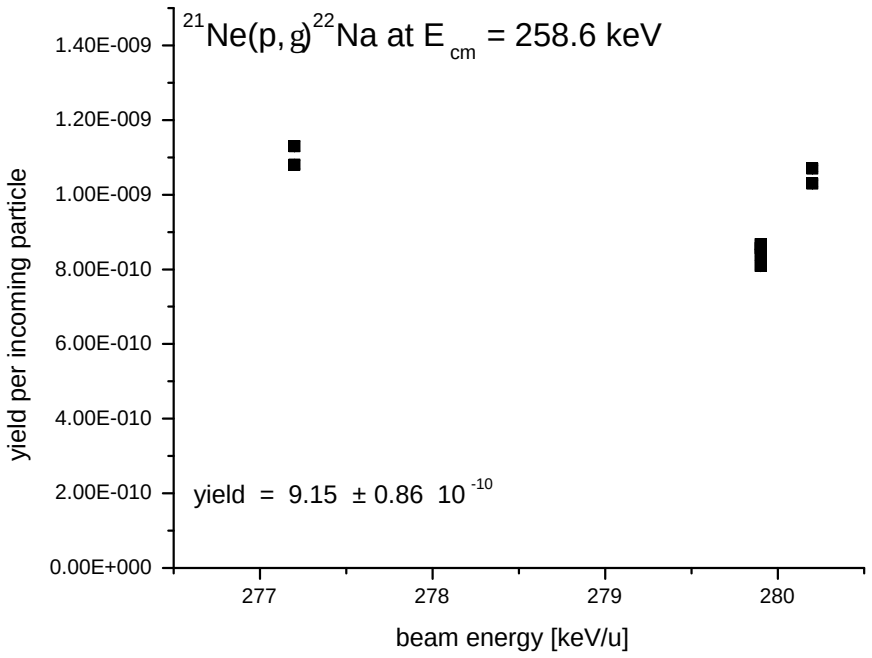

Figure 51: Observed resonance yield for $^{21}Ne(p,\gamma)^{22}Na$ at E_{cm}= 258.6 keV

The leaky beam suppression was estimated according to equation 65 to be

$$S \;=\; 5.71 \pm 0.01 \cdot 10^{-9}\;.$$

For completeness and future reference, the BGO efficiency was measured by the ratio of coincidence to singles events and averaged for the runs that placed the resonance into the target center. But it should be mentioned that the observed value requires further extensive studies on the BGO detection efficiency, since it is merely a convolution of detection efficiencies at various energies and the branching ratio of the excited state in the compound nucleus.

$$\varepsilon_{BGO} \;=\; 38.8 \pm 0.02 \quad \%$$

8.5 The $^{21}Ne(p,\gamma)^{22}Na$ Reaction at E_{cm} = 731.5 keV

The $^{21}Ne(p,\gamma)^{22}Na$ reaction at $E_{cm} = 731.5$ keV played an important role in the commissioning of the DRAGON. It was the first resonance, having a total width of 4 keV, where the thick target approximation could not be applied. Therefore, the full excitation curve was mapped at 4.6 Torr. Thus, all resonance parameters, resonance strength, energy, and width could be compared with the literature values [ANG99] and [END98]. Even though the resonance was spread over the full target, because of the narrow recoil cone angle, the transmission due to the reaction kinematics was still expected to be 99.2 $\pm$ 0.7 %. Beam currents ranged between 0.2 and 0.35 pnA.
Since the heavy ion background in the DSSSD energy spectrum was comparatively small, as shown in figure 52, the singles data as well as the coincidence data were taken into account in the data analysis. Here, in order to minimize any possible contamination, two cuts were applied on the heavy ion spectra: one concerning the energy of the recoils of interest in the DSSSD, the other their time of detection compared to the rf-pulse of the pre-buncher in the accelerator. The first cut covered the full range above channel 7000 up to and including the peak observed in the coincidence mode. The time cut, was chosen to contain the full peak shown in figure 53 or roughly 50% of the full timing spectrum.

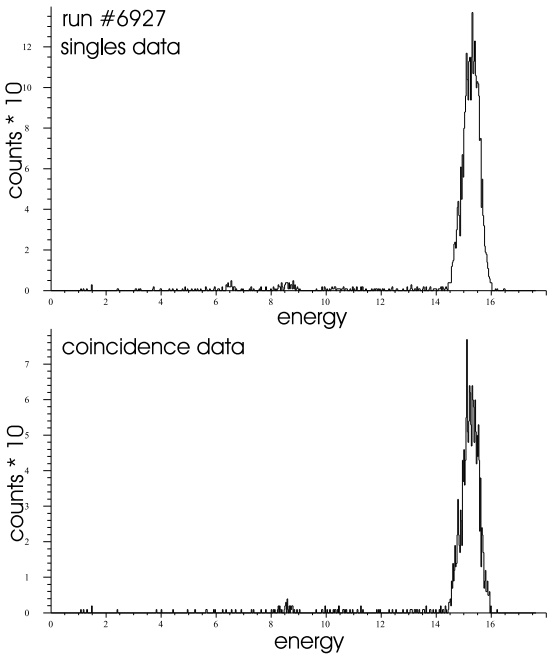

Figure 52: Recoil energy spectrum in singles and coincidence mode for $^{21}Ne(p,\gamma)^{22}Na$ at $E_{cm} = 731.5$ keV

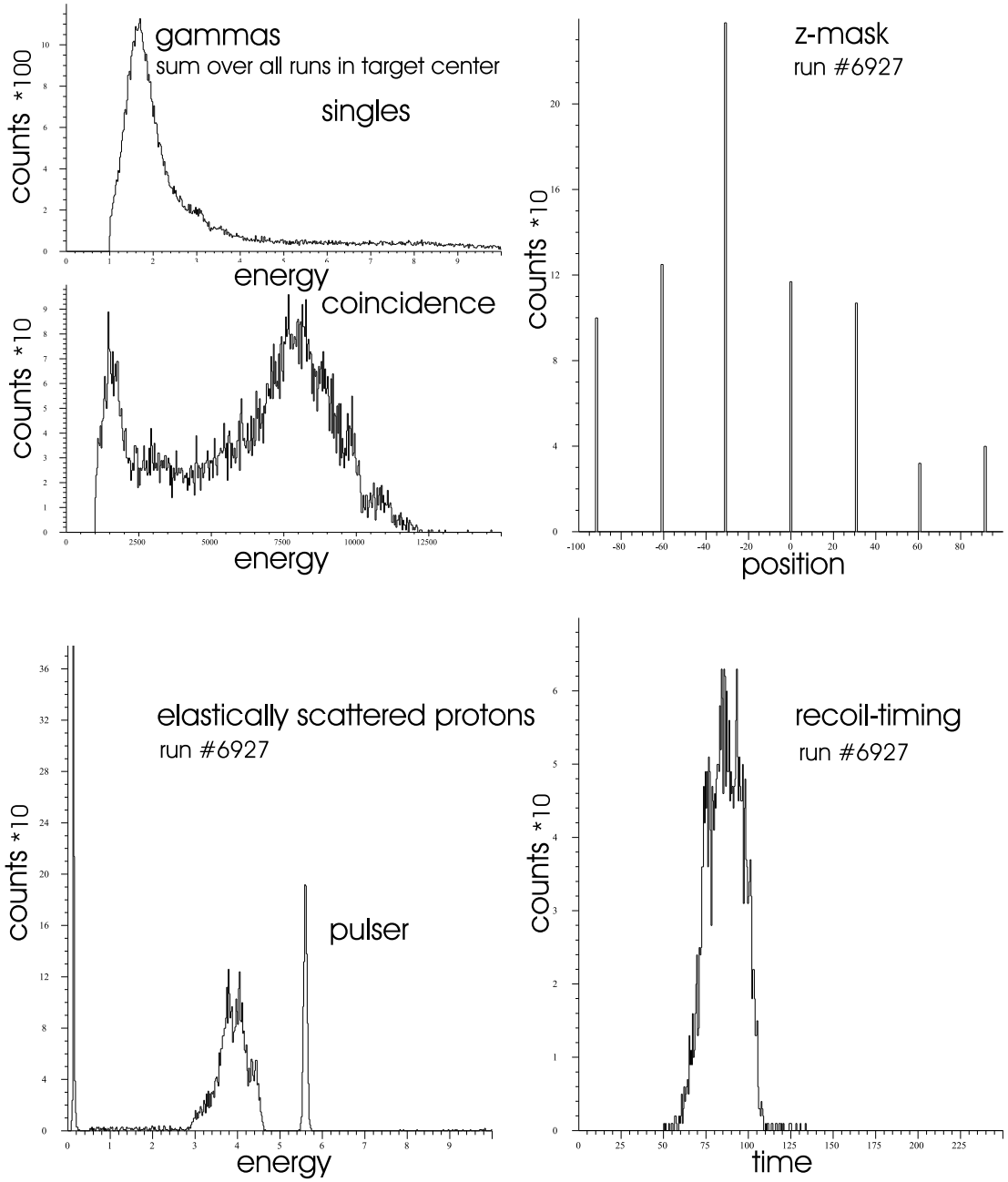

Figure 53: Gamma energy spectrum in singles and coincidence mode with the z-mask gamma distribution, the elastic energy spectrum and the correlation of ion detection time in the end detector with the rf-phase of the accelerator for a typical run of $^{21}Ne(p,\gamma)^{22}Na$ at $E_{cm} = 731.5$ keV

Because of the high count rate, the normalization of FC4 was done using only the first 60 sec of each run.
Since both, the energy of the beam with an empty target and the energy of the beam leaving the target was measured at MD_1 for each run, the energy loss in the target was well studied:

$$dE = 86.9 \pm 5.6 \quad \frac{eV}{10^{15} at/cm^2} .$$

The energy loss measured at DRAGON was 35% higher than suggested by the SRIM database (63.7 eV/10^{15} at/cm^2). Though this large discrepancy is not fully understood, the measured energy loss was used as in the following.

While for most of the runs the DRAGON was tuned on charge state 8+, the charge state distribution of the recoils was measured in four subsequent runs at a beam energy of 770 keV, by re-scaling the DRAGON ion optics according to the charge state ratio. The observed recoils were normalized to the elastically scattered protons such that the error in the charge state distribution was only of statistical nature. A complete list is shown in table 11. The obtained charge state distribution shows an unexpected asymmetry, that might indicate a loss of recoils, when the DRAGON was tuned on charge state 9+. Therefore, compared to [LIU02], the distribution width appears significantly narrower. A more detailed discussion is provided later within this thesis. However, to account for the resulting uncertainty a systematic error of ±5% was added in the analysis.

Table 11: Charge State Distribution for ^{22}Na recoils at E_{lab} 730 keV/u

Charge State	Probability	
6+	5.9 ± 0.2	%
7+	33.4 ± 0.1	%
8+	59.9 ± 0.1	%
9+	0.8± 0.3	%

The resulting full excitation curve, displayed in figure 54, was fitted with equation 33 and the resonance parameters were determined:

$$\omega\gamma = 3.85 \pm 0.42\ (stat) \pm 0.32; (sys) \quad eV$$

$$E_{cm} = 732.1 \pm 0.5 \quad keV.$$

The fitting value for the total width of the excitation curve was 6.26 ± 2.1 keV/u. Yet, the total resonance width is a convolution of the natural width with the energy spread of the beam (equation 45), assuming full detection efficiency for the recoils over the complete

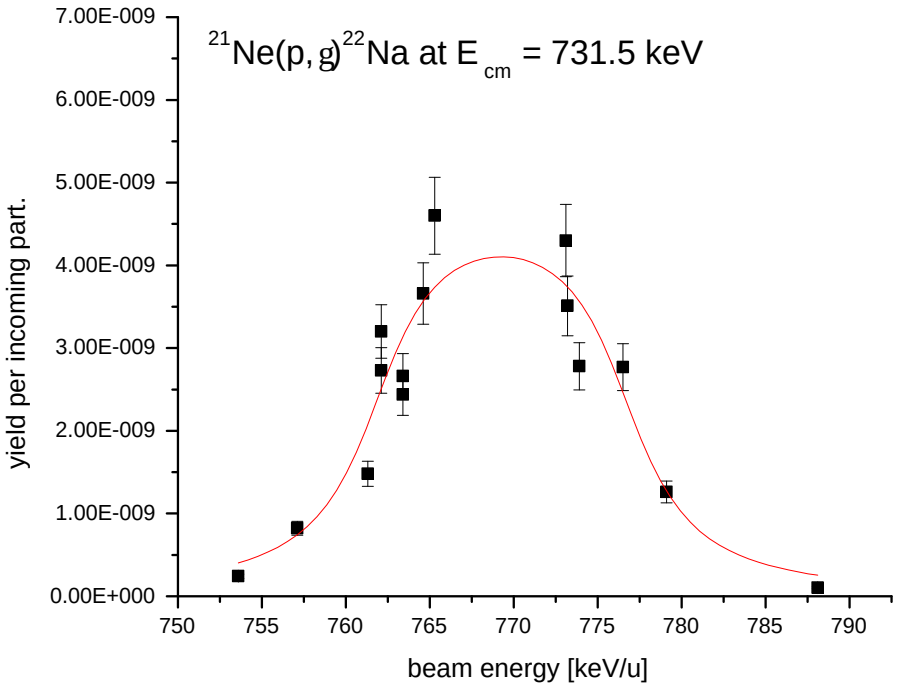

Figure 54: Yield for $^{21}Ne(p,\gamma)^{22}Na$ resonance at $E_{cm} = 731.5$ keV

target length. The energy spread of the beam is due to Doppler broadening because of the zero-point motion of the gas molecules (eq. 48), straggling in the target (eq. 49), and a distribution within the accelerated beam (tab. 3). With a Doppler spread of 0.64 ± 0.01 keV/u, energy straggling of 0.59 keV/u and a spread of the incoming beam of at least 3 ± 1 keV/u, this leads to a total resonance width of 3.1 ± 2.1 keV/u or, in the center of mass frame,

$$\Gamma_{tot} \;=\; 3.0 \pm 2 \quad keV$$

which agrees with previously published data.
This way, not only good agreement with the literature values could be found for the measured resonance strength and energy, but also for the resonance width. This demonstrated that the DRAGON can be used to study broad resonances with a width comparable to the target thickness.

The beam suppression per incoming ion at this energy was measured to be

$$S \;=\; (1.37 \pm 0.05) \cdot 10^{-12}\ .$$

According to [BER77] 80% of the de-excitation of the ^{22}Na nucleus goes through either a ground state transition via a 7.5 MeV gamma, or with 7 MeV to the first excited state (fig. 55). 10% branching ratio is predicted for a cascade to a state at 1937 keV with a 5.5 MeV gamma. The energy threshold was set so that the second gamma of 1.9 MeV would have not been detected. The remaining 10% de-excite through different cascades involving more than two gammas. Most of those cascades have two gammas above threshold.
Figure 53 shows the singles and the coincidence gamma energy distribution. For the latter only events with exactly one gamma above threshold were evaluated. Both spectra were summed over all runs. As can be seen in figure 56, some coincidence gamma events were detected with very low energies. Comparison of the expected gamma yields to the measured gamma spectrum clearly linked the low energy events to beam induced background, which showed a peak at roughly 2 MeV in the singles spectrum. Conclusively, a small amount of recoil events was detected in coincidence with a background gamma. Because this connection was of accidental character, those events were excluded from analysis.

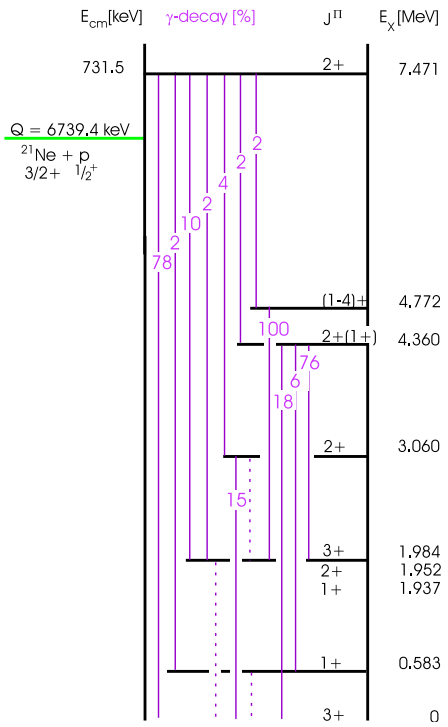

Figure 55: Decay scheme for the ^{22}Na excited state at $E_x = 7.47$ MeV.

In the present work the BGO efficiency was only estimated; a more complex study of the BGO efficiency will be part of another thesis [GIG03].

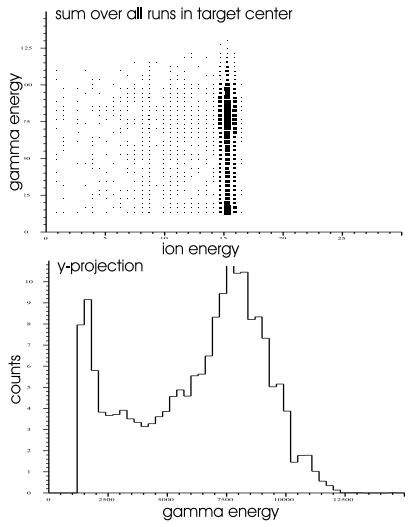

Figure 56: Coincidence recoils versus γ-energy and projection to the γ-energy axis for $^{21}Ne(p,\gamma)$ at $E_{cm} = 731.5$ keV.

Since a fit of the data did not seem to be possible, the amount of "good" coincidence events with a gamma above 7 MeV was estimated by integrating over the high energy shoulder of the peak (channel 7800-12500), where low energy background contribution should have been negligible. The result was multiplied by two. Thus, the BGO efficiency was roughly the number of good recoils, normalized to the 80% of visible transitions, divided by the sum of all single recoil events. A 10% error was employed in order to account for the crudeness of this method. It should be noted that only events with exactly one gamma above threshold were evaluated. Thus, the obtained BGO efficiency BGO_{7MeV} is slightly lower than would be observed by the coincidence to singles ratio, which also accounts for events in which the gamma energy is spread over several detectors.

$$\varepsilon_{BGO7MeV} \; = \; 39 \pm 4 \quad \%.$$

The dependence BGO efficiency for the detection of any gamma depending on the position may be seen in figure 57. The indicated line is to guide the eye, but it may be estimated that the efficiency will drop by roughly 20% outside the inner 25 mm, which is comparable to the results obtained earlier with $^{20}Ne(p,\gamma)^{21}Na$. Also shown is the BGO efficiency obtained from the simple coincidence to singles ratio.
The z-mask distribution led to reasonable results in the relation of beam energy versus position of gamma activity. The range within which the z-mask feature may be used to determine the resonance center is given by the linear region of the s-shape function in figure 58. It shows the linear correlation of position and energy in a range of 762 to 776 keV/u or the central 4 cm. The region of linear response is reduced because of the natural width of the resonance.

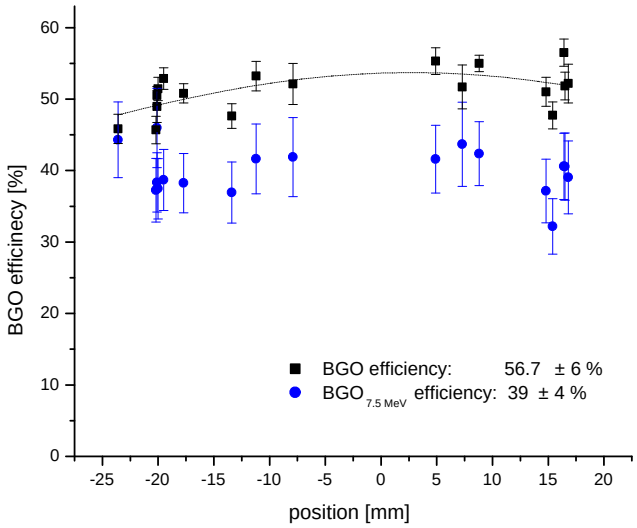

Figure 57: Efficiency of BGO array versus position for the $^{21}Ne(p,\gamma)^{22}Na$ resonance at $E_{cm} = 731.5$ keV

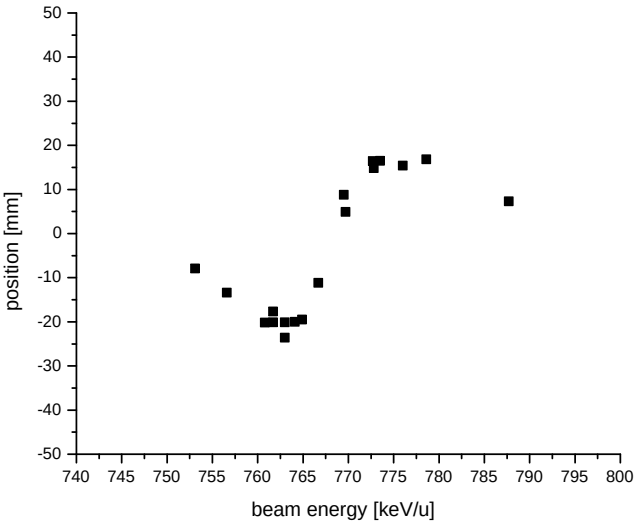

Figure 58: Beam energy versus resonance position within target for $^{21}Ne(p,\gamma)^{22}Na$ at $E_{cm} = 731.5$ keV

8.6 The $^{24}Mg(p,\gamma)^{25}Al$ Reaction at $E_{cm} = 214.0$ keV

The resonance in the $^{24}Mg(p,\gamma)^{25}Al$ reaction at $E_{cm} = 214.0$ keV was just recently re-measured with an accuracy of 7% [POW99]. It is energetically close to the resonance in $^{21}Na(p,\gamma)^{22}Mg$ at $E_{cm} = 212$ keV, which was one of the first milestones of the initial scientific program. Good transmission of 99.8 $^{+0.2}_{-0.3}$ % was expected. Therefore, besides reproducing the published cross section, the focus was on measuring the resonance energy. Thus, discrepancies between the literature values and the new DRAGON results for $^{21}Na(p,\gamma)^{22}Mg$ [BIS03] were to be ruled out. At 4.5 Torr, the rising edge of the thick target yield curve was mapped up to the plateau region, with some runs additionally conducted at lower pressures. Typical beam currents ranged between 0.2 and 1 pnA.
As can be seen in figure 59, the recoil energy spectrum in the DSSSD for a typical run was dominated by a strong peak of leaky beam ions. Even in coincidence with a gamma event, recoils could not easily be distinguished from beam ions. Therefore, additional requirements were applied on the time-of-flight through the DRAGON separator. Shown in figure 60 is a two dimensional spectrum, displaying the time relation of heavy ions and gamma events. One axis shows the t-o-f using the DSSSD as the start and the BGO array as the stop detector, the other axis the inverse. The recoils of interest form a cluster, while accidental coincidence events of gammas and a leaky beam ions show up as a constant background.

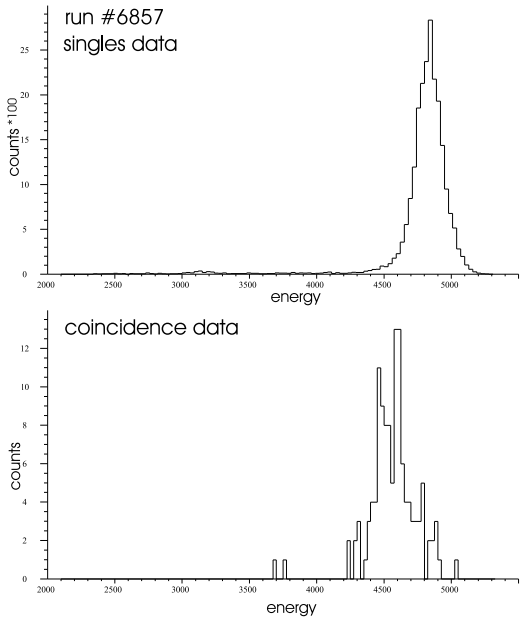

Figure 59: Recoil energy spectra in singles and coincidence mode for the $^{24}Mg(p,\gamma)^{25}Al$ reaction at $E_{cm} = 214.0$ keV

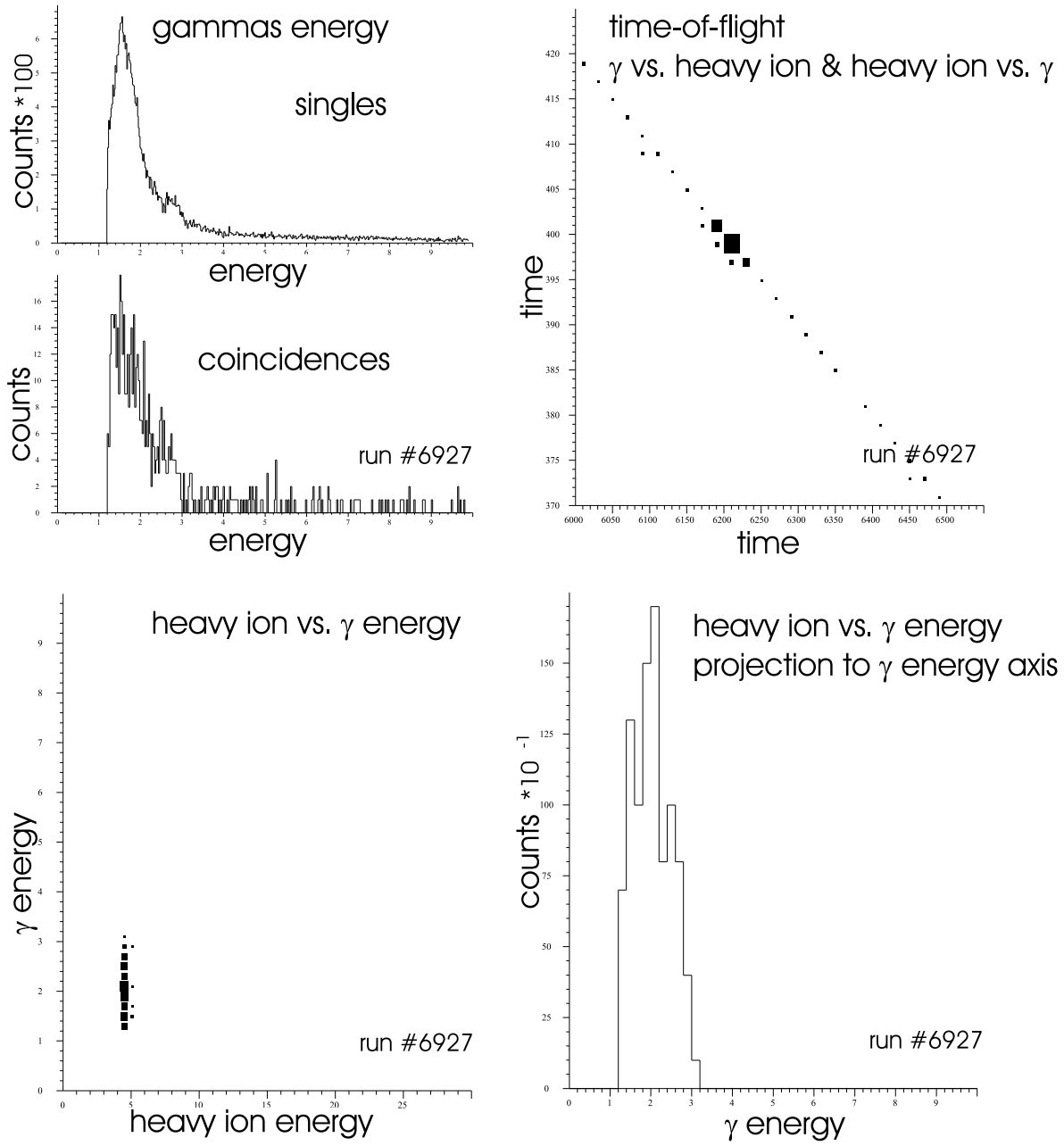

Figure 60: Gamma energy spectrum in singles and coincidence mode with a two dimensional time-of flight graph showing γ versus heavy ion time and heavy ion versus γ time, a two dimensional plot showing the relation of γ and heavy ion energy as well as its projection on the y(γ energy)-axis for a typical run of $^{24}Mg(p,\gamma)^{25}Al$ at $E_{cm} = 214.0$ keV

The effect of both cuts, a 200 ns window in the flight time through the separator and an additional gamma energy cut, reduced the background in the DSSSD energy spectrum significantly (fig. 61). Though the time-of-flight spectrum shows a significant background contribution, most of these events were related to noise in the DSSSD, with energies less then 10 keV. Thus, the background below the recoil energy peak was less than 0.01% for all runs, except for two off-resonance measurements where background contributions were slightly higher and of the order of 0.2 %. The coincidence gamma energy spectrum resulting from cuts on the time-of-flight is displayed in figure 62.

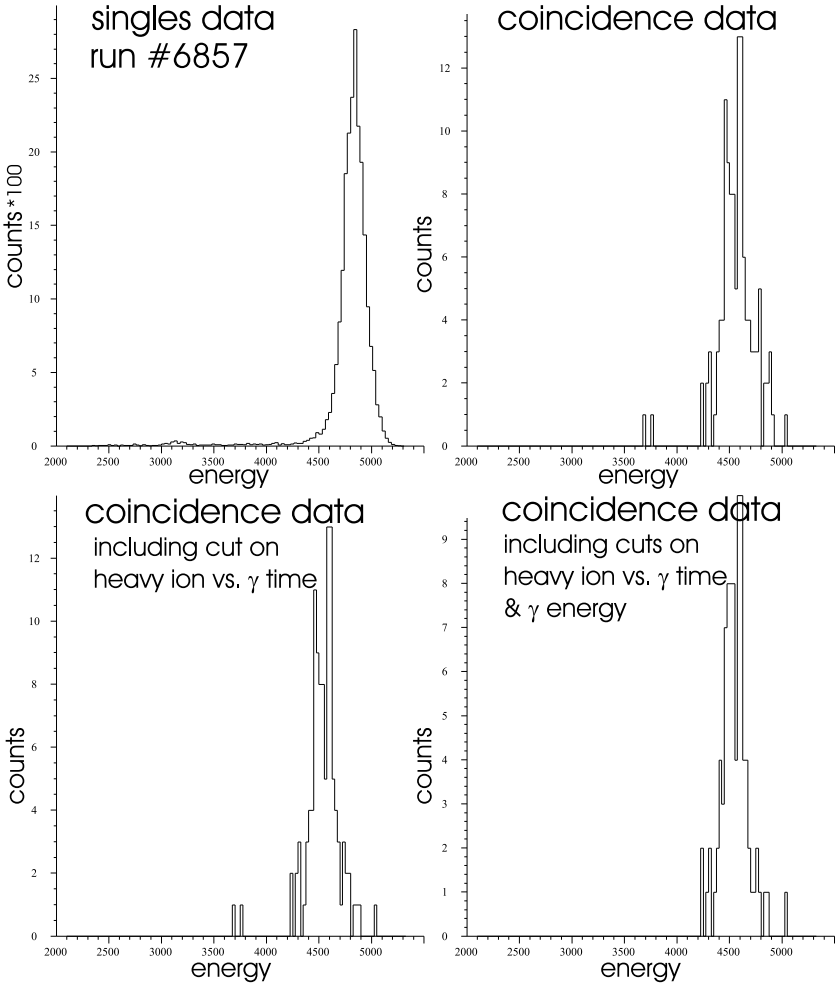

Figure 61: Recoil energy spectra in singles and coincidence mode with various cuts on the t-o-f and γ-energy for $^{24}Mg(p,\gamma)^{25}Al$ at $E_{cm} = 214.0$ keV

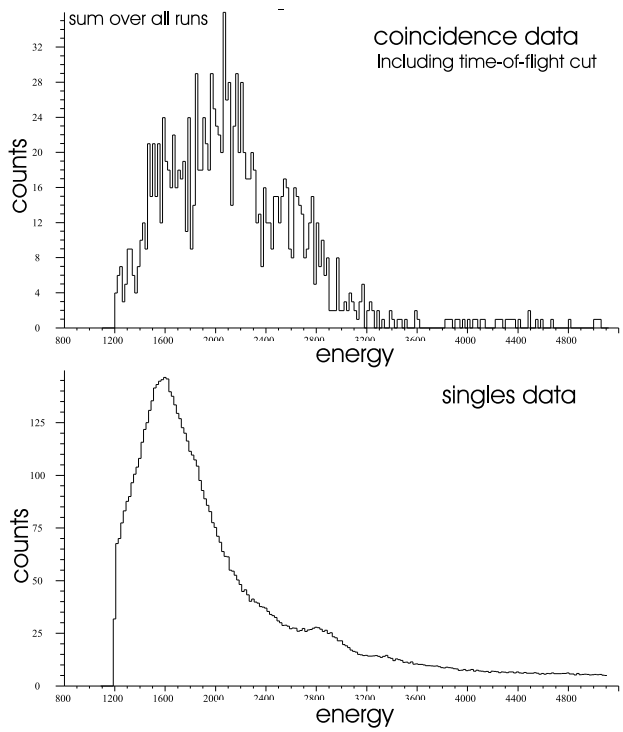

Figure 62: Gamma energy spectrum for the highest energy gamma detected in coincidence, compared to the sum of all singles gammas for the $^{24}Mg(p,\gamma)^{25}Al$ reaction at $E_{cm} = 214.0$ keV, summed over all runs

Accepting only coincidence events for the data analysis, the count rate had to be normalized to the BGO efficiency. 78% of the gamma rays were expected to have an energy of 2 MeV [FIR96], corresponding to a cascade to the first excited state in ^{25}Al. The subsequent decay to the ground state would be expected below the 1.2 MeV software threshold (fig. 63). Those, as well as the 4% 2.5 MeV gammas decaying to the ground state, were the only gammas observable. Other cascade gammas, expected from the de-excitation of the excited state $E_x = 2.485$ MeV, should have energies below threshold. As expected, the two dimensional spectrum of heavy ion versus gamma energy showed an accumulation around channels 2000 and 2500, clearly displayed in the projection onto the gamma energy axis in figure 60 and in the gamma coincidence spectrum in figure 62. It should be mentioned, that the soft hardware threshold might cut into the comparatively low energetic gammas of 2 MeV. Yet, threshold effects should be negligible, because the peak to total ratio for a 2 MeV gamma should be significantly better than 50%. According to the experience from earlier measurements, a 40% efficiency was assumed with an error of $\pm$ 4 % and the yield additionally normalized to the 82% fraction of observable gammas rays.

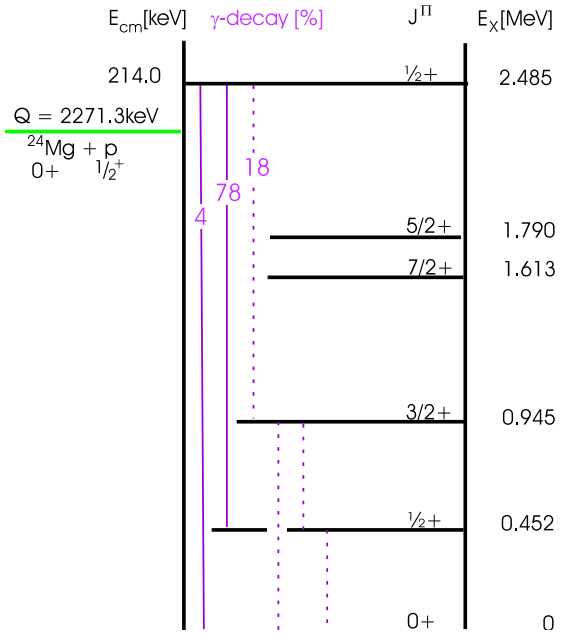

Figure 63: Decay scheme for the ^{25}Al excited state at $E_x = 2.49$ MeV.

The charge state probability for the chosen $q = 4+$ recoils was not measured. Instead, the semi-empirical approach from [LIU02] was employed to calculate the charge state fraction of the $4+$ ^{25}Al recoils, which turned out to be 41%. A 10% error was assigned. The coincidence counts were further normalized to the incoming beam according to equation 63. Here, an overall normalization of beam intensity to elastically scattered protons could be found to reduce the statistical error.
The energy loss was measured several times to be close to the SRIM value of 88.3 $\frac{eV}{10^{15}at/cm^2}$:

$$dE \ = 83.4 \ \pm 3.06 \quad \frac{eV}{10^{15}at/cm^2} \ .$$

Finally, the full excitation curve was fitted with function 33 and is displayed in figure 64. The corresponding fit parameters are listed in table 12.

The measured resonance parameters agree well with the published values of 12.7 meV [POW99] and 214.0 keV [END98]:

$$\omega\gamma \ = \ 11.7 \pm 1.0 \ (stat) \pm 1.2 \ (sys) \quad meV$$

$$E_{cm} \ = \ 214.5 \pm 0.5 \quad keV.$$

Table 12: Fitting Parameters for the $^{24}Mg(p,\gamma)^{25}Al$ Yield at $E_{cm} = 214$ keV

Parameter	Value	Units
P1	$(2.20 \pm 0.18) \cdot 10^{-11}$	per particle
P2	221.9 ± 0.4	keV/u
P3	13 fixed	keV/u
P4	0.42 ± 0.30	keV/u
P5	0	

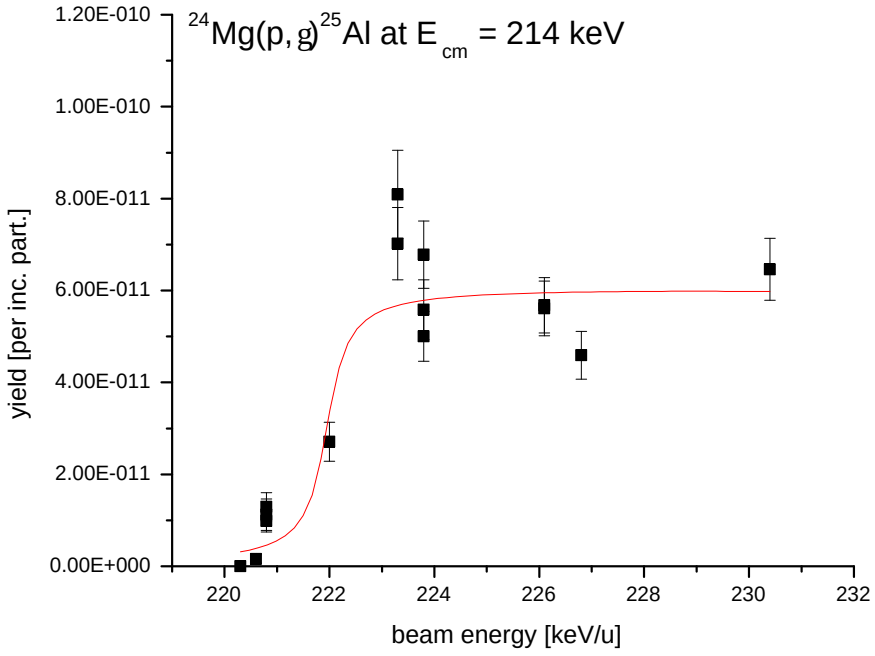

Figure 64: Yield curve measured for the $^{24}Mg(p,\gamma)^{25}Al$ resonance at $E_{cm} = 214.0$ keV

In order to estimate the beam suppression factor in a manner comparable to the values previously calculated for other reactions, both, the factor without coincidence requirements as well as the factor due to additional cuts on the time-of-flight and the recoil energy were calculated:

$$S_{sgl} = (3.83 \pm 0.1) \cdot 10^{-9} ,$$

$$S_{coin} = (8.80 \pm 0.11) \cdot 10^{-12} .$$

8.7 The $^{24}Mg(p,\gamma)^{25}Al$ Reaction at $E_{cm} = 402.2$ keV

The $^{24}Mg(p,\gamma)^{25}Al$ reaction at $E_{cm} = 402.2$ keV was also chosen, because of its well studied cross section [POW99]. The goal was to determine the resonance strength. Therefore, only a few points at various energies were taken to demonstrate the thick target yield at 4.7 Torr without mapping the full excitation curve. Typical beam currents were of the order of 0.05 to 1 pnA. Beforehand, the transmission was calculated to be 99.9 $^{+0.1}_{-0.3}$ %. As can be seen in figure 65 the recoil energy spectrum was hidden below the low energy tail of a massive leaky beam peak. Thus, coincidence requirements with the prompt de-excitation gamma were necessary to suppress any background contribution.

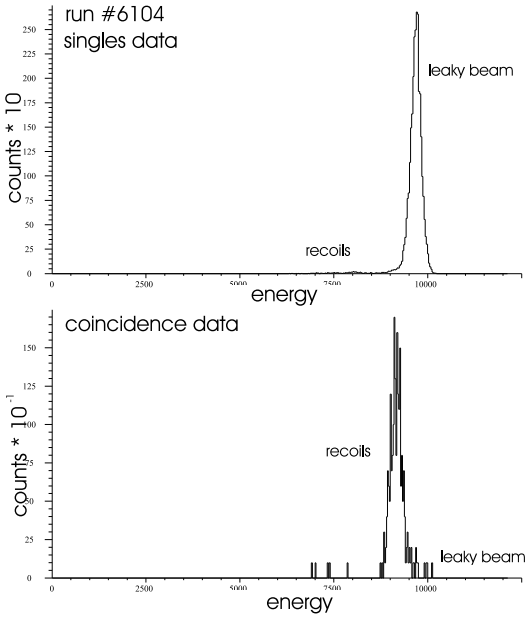

Figure 65: Recoil energy spectrum in singles and coincidence mode for $^{24}Mg(p,\gamma)^{25}Al$ at $E_{cm} = 402.2$ keV

The $E_x = 2674$ keV state in ^{25}Al ($E_{cm} = 402.2$ keV) decays through different branches (fig. 67). According to [FIR96], three branches to the ground and the first two excited states cover 70% of the de-excitation. Here, all first gamma rays were well above the 1.2 MeV threshold of each individual detector and, therefore, visible to the BGO array. In addition, 62% of the secondary gammas of the cascade to the state at 1.8 MeV were above threshold. Thus combined, 89% of the decay was observable to the BGO array, with each one gamma above threshold. As expected, the gamma energy spectrum in figure 66 indicates a structure around 2.5 MeV.

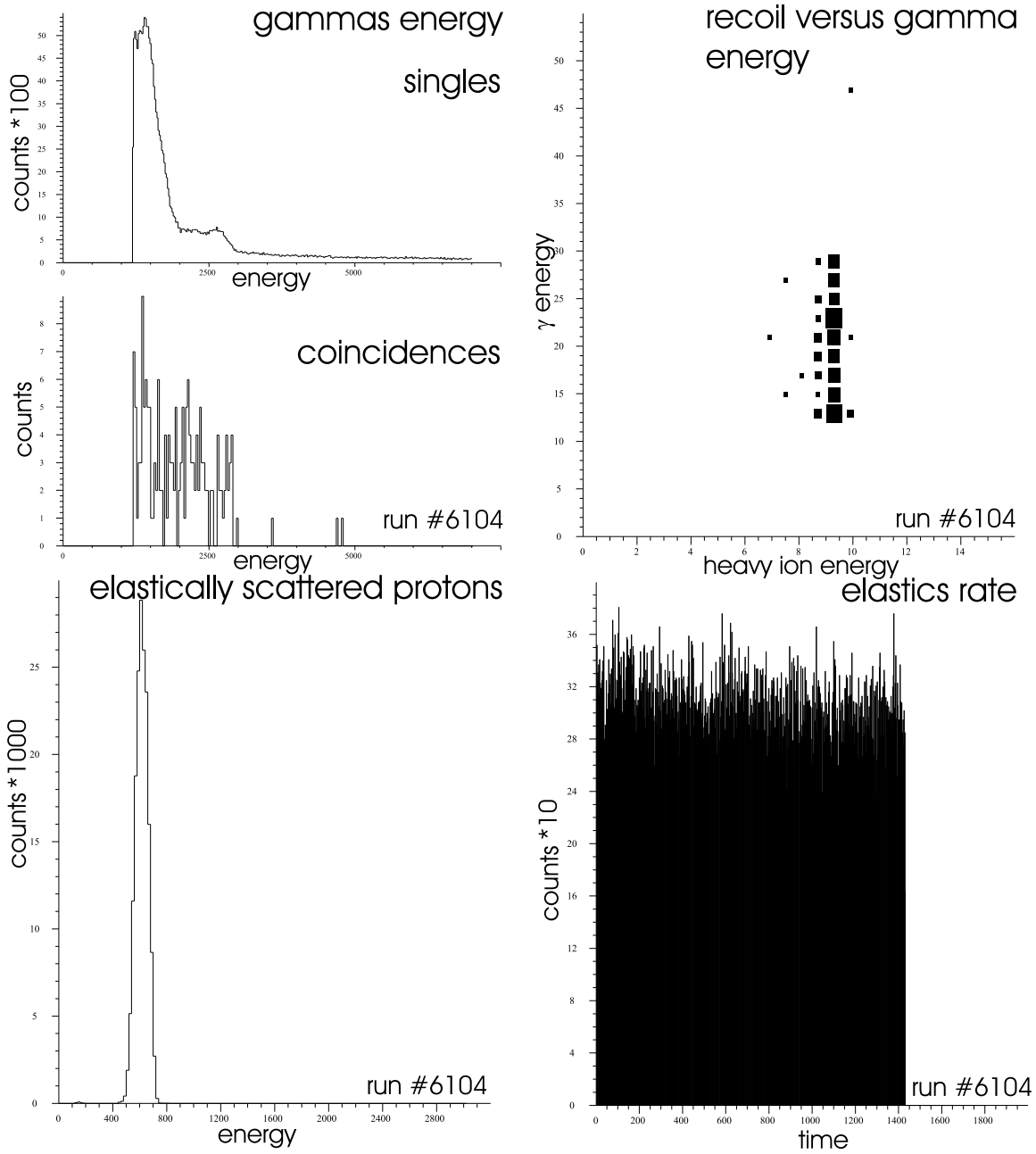

Figure 66: Gamma energy spectrum in singles and coincidence mode with a two dimensional graph showing γ versus heavy ion energy, the spectrum of the elastically scattered protons and their rate versus run time for a typical run of $^{24}Mg(p,\gamma)^{25}Al$ at $E_{cm} = 402.2$ keV

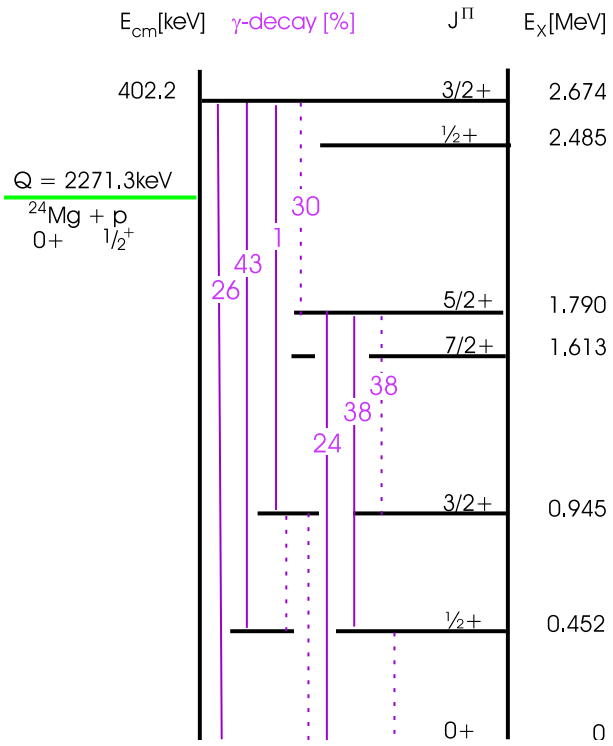

Figure 67: Decay scheme for the ^{25}Al excited state at $E_x = 2.67$ MeV.

Since the resonance was not observable in the scattering channel, a general normalization for beam current on FC4 compared to the rate measured in the elastic monitor was found, as described above.
The charge state distribution was measured for the recoils and is listed in table 13.

Table 13: Charge State Distribution for the ^{25}Al recoils at $E_{lab} = 400$ keV/u

Charge State	Probability	
5+	15.7 ± 1.7	%
6+	29.3 ± 2.9	%
7+	50.6 ± 6.9	%
8+	4.4 ± 1.7	%

The accepted events were normalized to the incoming current, the run time, dead times of heavy ion and gamma acquisition, charge state fraction, DSSSD efficiency and transmission. The BGO efficiency was estimated to be 40 ± 4 % and the fraction of observable

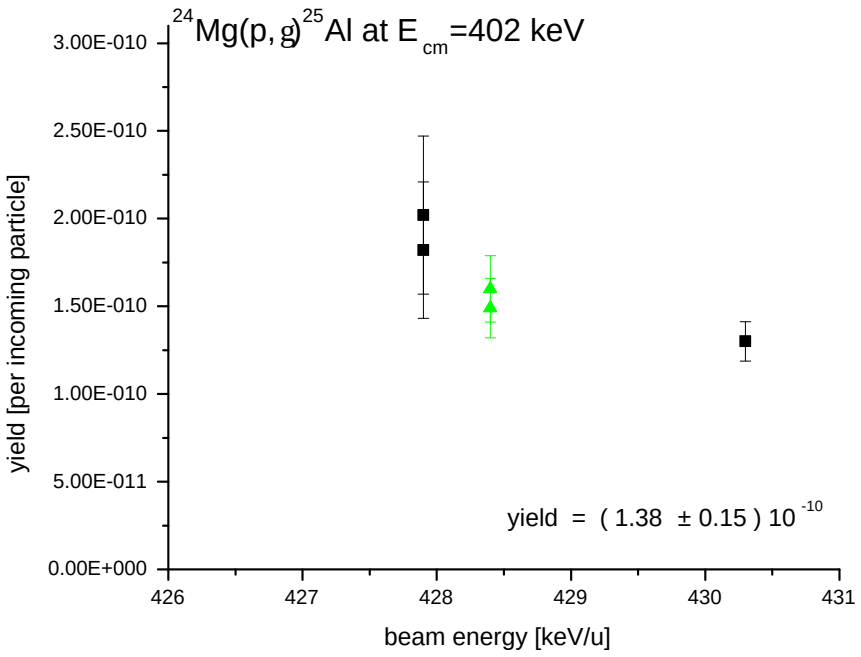

Figure 68: Yield measured at various energies for $^{24}Mg(p,\gamma)^{25}Al$ at $E_{cm} = 402.2$ keV

gammas was taken into account. The thick target yield in figure 68 is plotted for runs at charge states q=6+ (black squares) and 5+ (green triangles), both corrected for their individual population probability.
With a measured energy loss of

$$dE \ = 110 \ \pm 4.7 \quad \frac{eV}{10^{15} at/cm^2}$$

which is 23% higher than the SRIM value of 89.3 $\frac{eV}{10^{15} at/cm^2}$ the resonance strength is

$$\omega\gamma \ = \ 57.4 \pm 6.0 \ (stat) \pm 6.2 \ (sys) \quad meV$$

and agrees within the error with the published value of 42 meV [POW99].

The average values for both suppression factors are:

$$S_{sgl} \ = \ (7.54 \pm 0.62) \cdot 10^{-10} \ ,$$
$$S_{coin} \ = \ (2.61 \pm 0.59) \cdot 10^{-12} \ .$$

8.8 The $^{24}Mg(p,\gamma)^{25}Al$ Reaction at $E_{cm} = 790.4$ keV

The $^{24}Mg(p,\gamma)^{25}Al$ reaction at $E_{cm} = 790.4$ keV does not strictly qualify as a calibration reaction. In the past, there has been some disagreement on its resonance strength. According to [ANG99] the adopted value is 532 ± 41 meV, with the publications varying between 220 and 580 meV. Recently, [POW99] has published the value of 640 meV, rescaling the results from [TRA75], originally 490 ± 70, to their disagreement on the lower resonances at 214 and 402.2 keV. Using the high intensity ^{24}Mg beam of 0.1 to 0.4 pnA, this resonance strength was measured again at pressures of 4.4 to 4.7 Torr and several beam energies between 815 and 827 keV/u. Time constraints prevented a scan over the full excitation curve.
For the given reaction kinematics, the transmission was 99.9 $^{+0.1}_{-0.2}$ %. The BGO array was not working properly at the time of the measurements, but because of the good properties of the incoming beam, for most of the runs, the recoils of interest could easily be distinguished from leaky beam ions in the energy spectrum of the DSSSD as shown in figure 69. The recoils of interest showed both, good timing versus the rf-signal of the pre-buncher and a small spot size on the DSSSD (fig. 70).

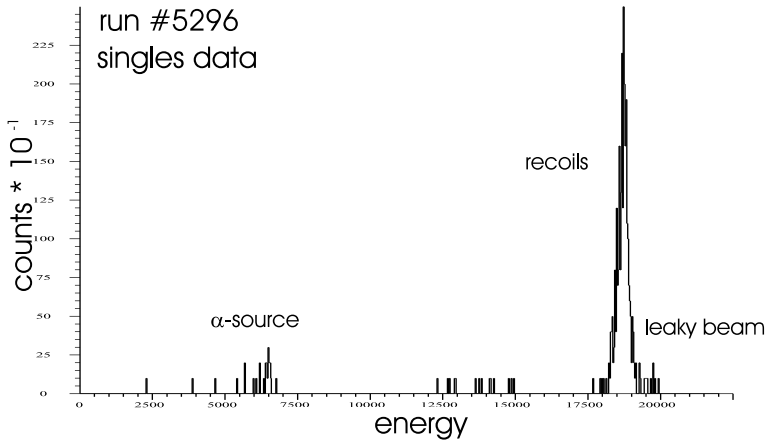

Figure 69: Recoil energy spectrum in singles mode for $^{24}Mg(p,\gamma)^{25}Al$ at E_{cm} =790.4 keV

The charge state distribution was measured for the ^{25}Al recoils, and the results with the related statistical errors are listed in table 14. As before, a general ratio of elastic proton rate to beam current was determined.
The accepted events were normalized to the incoming current, run time, dead time, charge state fraction, DSSSD efficiency and transmission. The yield in figure 71 is plotted for runs at charge state q = 9+.
The measured energy loss was 28% higher than the SRIM value of 81.8 $\frac{eV}{10^{15}at/cm^2}$:

$$dE = 105 \pm 3.7 \quad \frac{eV}{10^{15}at/cm^2} .$$

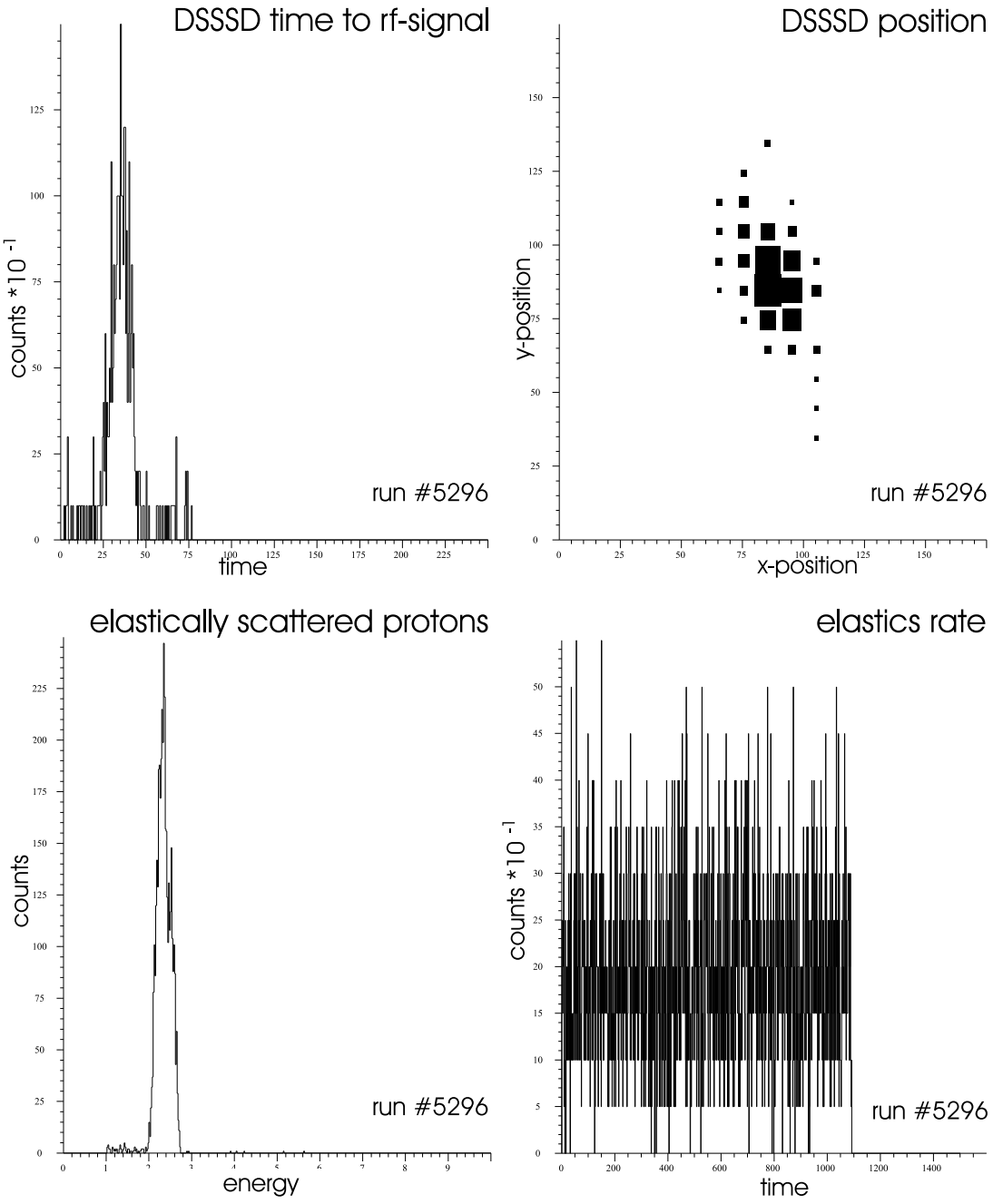

Figure 70: Recoil time versus rf-signal peak and position distribution on the DSSSD, as well as the elastically scattered proton energy and rate for a typical run of $^{24}Mg(p,\gamma)^{25}Al$ at $E_{cm} = 790.4$ keV

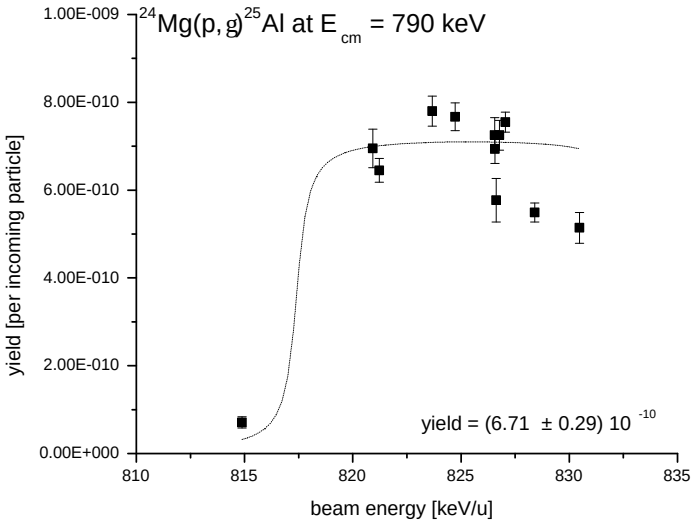

Figure 71: Yield measured at various energies for $^{24}Mg(p,\gamma)^{25}Al$ at $E_{cm} = 790.4$ keV

Thus, the resonance strength was measured to be

$$\omega\gamma \;=\; 576 \pm 25\;(stat) \pm 31\;(sys) \quad meV.$$

This agrees with the recently suggested value in [POW99], but is much closer to the result of [KEI80], who measured 580 ± 60 meV. The latter is already included in the NACRE compilation [ANG99].
No value for the resonance energy was obtained. However, from figure 71 it is clear that the resonance energy lied between 815 and 820 keV/u, which would agree with literature. The average value for the suppression factor was

$$S \;=\; (1.82 \pm 0.16) \cdot 10^{-11}\;.$$

Table 14: Charge State Distribution for the ^{25}Al recoils at $E_{lab} = 780$ keV/u

Charge State	Probability	
7+	5.5 ± 0.3	%
8+	23.5 ± 1.0	%
9+	41.4 ± 1.6	%
10+	25.4 ± 1.0	%
11+	4.2 ± 0.2	%

8.9 Results

In the following, the results obtained from measuring six different stable beam induced nuclear resonances are summarized and evaluated. To prove that the DRAGON facility is working reliably and the systematics are sufficiently understood, the measured yields and resonance energies will be compared to the literature values. Important for the calculation of the resonance strength is also the beam energy loss in the target material. Commonly, in other publications, the SRIM program is utilized as the only available data base. However, in the course of the experiments, deviations from the SRIM values were observed and will be discussed. The achieved beam suppression factors and therefore the potential of the DRAGON recoil mass separator to eliminate beam effects will be summarized. The measured charge state distributions will also be compared to a recently published semi-empirical approach, followed by a brief discussion on the BGO gamma array efficiency.

8.9.1 Comparison of the Measured Resonance Strengths

The resonance strength of 6 different resonances in $^{20}Ne(p,\gamma)^{21}Na$, $^{21}Ne(p,\gamma)^{22}Na$ and $^{24}Mg(p,\gamma)^{25}Al$ were measured independently and absolutely. Figure 72 and table 15 compare the measured strengths to the values published in [ANG99] and, for the lower two $^{24}Mg(p,\gamma)^{25}Al$ states, in [POW99]. In the latter publication, the resonance strengths were deduced from measurements of the gamma branching ratios and gamma widths of the excited states at $E_x = 2485$ and 2674 keV, so that the published results are independent of target properties. In the following, the deviation of the parameter X shall be defined as

$$dev \;=\; \frac{X_{DRA} - X_{pub}}{X_{pub}} \; .$$

The measured results do not indicate any trends, but scatter normally around the expected values, except for the lower state in $^{21}Ne(p,\gamma)^{22}Na$. Here, the charge state distribution was calculated, and the assumed 35%, based on a semi-empirical approach [LIU02], might be inaccurate. In addition, the resonance strength measured previously by [GOE82] used TRIM, a precursor version of SRIM [BIE00], to convert measured yield into resonance strength. The actual applied value is not mentioned in the paper, therefore, the discrepancy might also be related to differences in the energy loss.
Summarizing it may be assumed that the systematic errors are mainly due to uncertainties in the charge state distribution of the outgoing recoils and the accuracy in measuring the energy loss in the gas target which depends linearly on the knowledge of the effective target length. Yet, a systematic error in the target length would result into a systematic deviation from the literature values. This is not observed. It may be concluded that the systematic uncertainties of the DRAGON are well estimated and truly of the order of the statistical and instrumental errors.

Table 15: Measured Resonance Strength

Reaction	E_{cm} [keV]	$\omega\gamma_{pub}$	$\omega\gamma_{meas}$	$\frac{\omega\gamma_{meas}}{\omega\gamma_{pub}}$
$^{20}Ne(p,\gamma)^{21}Na$	1112.6	1.13 ± 0.07 eV	0.92 ± 0.17 eV	0.81
$^{21}Ne(p,\gamma)^{22}Na$	258.6	82.5 ± 12.5 meV	209 ± 35 meV	2.27
$^{21}Ne(p,\gamma)^{22}Na$	731.5	3.95 ± 0.79 eV	3.85 ± 0.53 eV	0.97
$^{24}Mg(p,\gamma)^{25}Al$	214.0	12.7 ± 0.09 meV	11.7 ± 1.6 meV	0.92
$^{24}Mg(p,\gamma)^{25}Al$	402.2	41.6 ± 2.6 meV	57.4 ± 8.7 meV	1.36
$^{24}Mg(p,\gamma)^{25}Al$	790.4	532 ± 41 meV	576 ± 39.3 meV	1.08

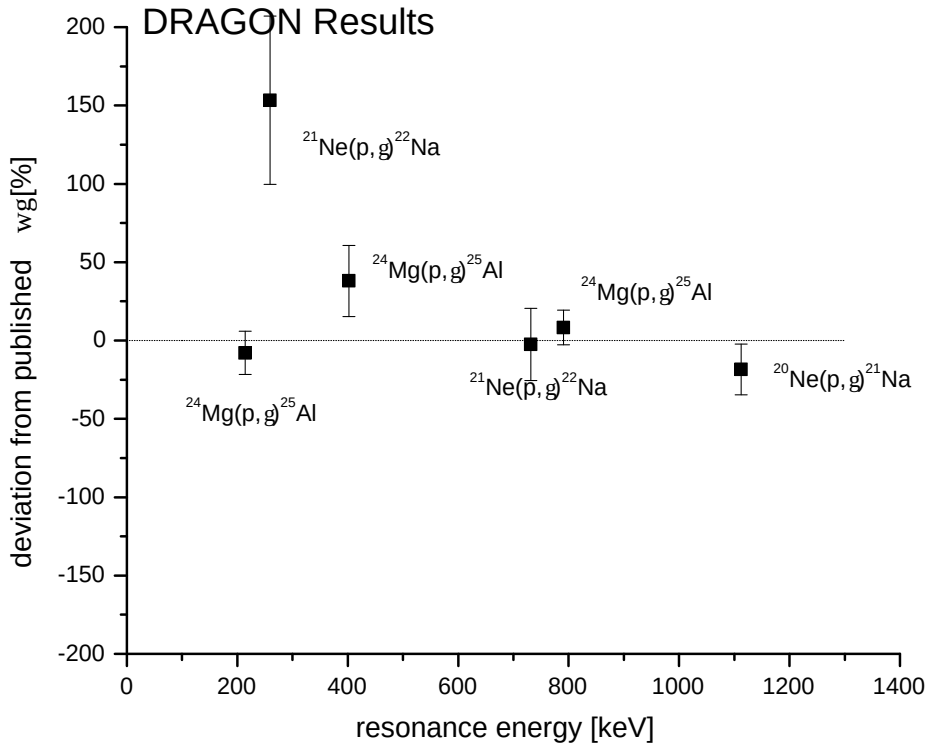

Figure 72: Agreement of resonance strengths measured with DRAGON compared to the literature values

8.9.2 Agreement with the Energy Calibration

The energy was measured for three different stable beam reactions, namely, $^{20}Ne(p,\gamma)^{21}Na$ at E_{cm} 1112.6 keV, $^{21}Ne(p,\gamma)^{22}Na$ at 731.5 keV, and $^{24}Mg(p,\gamma)^{25}Al$ at 214.0 keV. Within the DRAGON uncertainty of 0.2% the obtained deviations scatter around zero as shown in figure 73 and table 16.
The DRAGON is not a precision instrument to determine resonance energies. The mass excess to obtain the reaction Q-values in combination with a careful observation of the de-excitation gamma energies might be more accurate. But using MD_1 as an instrument to easily measure the beam energy at the end of the accelerator, after the beam has passed all HEBT bunchers, has proven to be a convenient tool during the experiments.
The agreement with literature was within error, thus, acceptable for the commissioning studies. A list of measured resonance energies versus literature values is given in table 16.

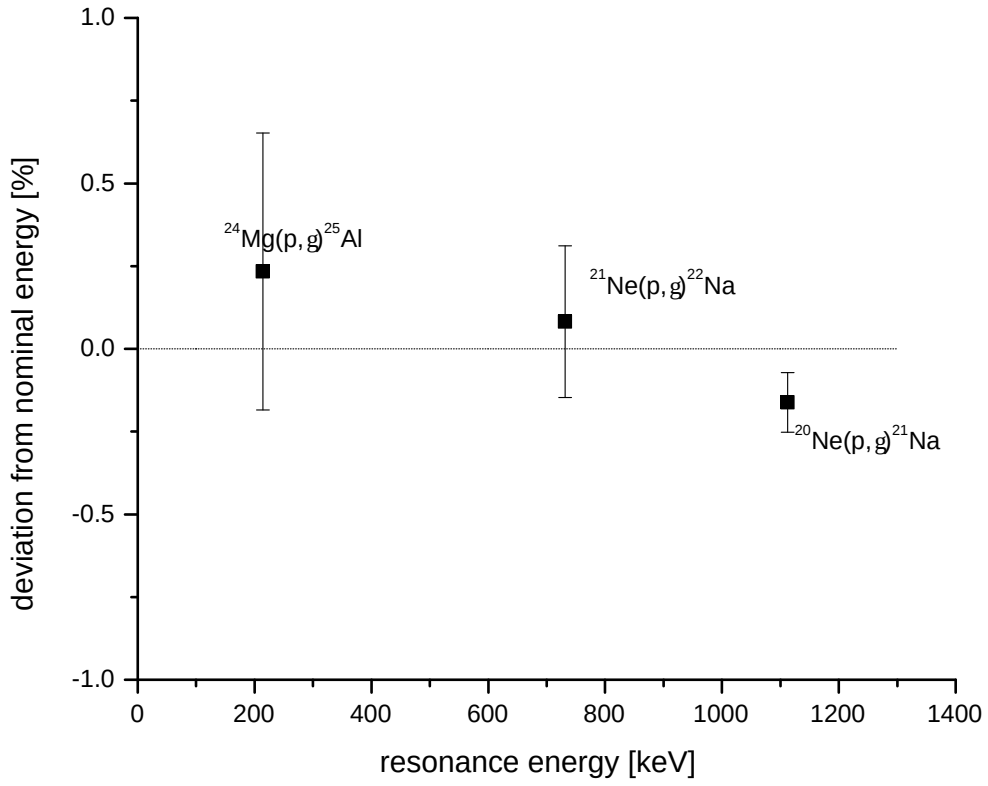

Figure 73: Comparison of measured resonance energies to the literature values

Table 16: Measured Resonance Energies

Reaction	E_{pub} [keV]	E_{meas} [keV]	$\frac{E_{meas}}{E_{pub}}$
$^{20}Ne(p,\gamma)^{21}Na$	1112.6 ± 0.6	1110.9 ± 0.8	0.998
$^{21}Ne(p,\gamma)^{22}Na$	731.5 ± 1.6	732.1 ± 0.5	1.001
$^{24}Mg(p,\gamma)^{25}Al$	214.0 ± 0.8	214.5 ± 0.4	1.002

Based on these measurements, the resonance energy has been measured for several states in the $^{21}Na(p,\gamma)^{22}Mg$ environment. The new state at $E_{cm} = 821$ keV will be discussed in more detail in the present work. But it should be mentioned here that some discrepancy to other publications was observed in measuring E_{cm} required to populate the excited state at $E_x = 5713$ keV in ^{22}Mg. With the published Q-Value of 5501 keV it was expected to be at 212 keV, yet found at 205.7 keV [BIS02] and [BIS03]. Its consequences will be discussed within the conclusion section of this thesis.

8.9.3 Energy Loss compared to the SRIM Data Base

The SRIM code [BIE00], widely used throughout different fields of physics research, is a program to calculate energy loss of ions in target materials. The semi-empirical code is based mainly on studies of protons impinging on heavy ion solid targets using a quantum mechanical treatment for ion-atom collisions in a statistical algorithm. It has to be mentioned that, especially at low energies, little experimental data is available to test the code for heavy ions traversing a hydrogen or helium target.

As induced in equation 34, the derived resonance strength is inversely proportional to the energy loss. Thus, the latter contributes significantly to the statistical error. Tests with DRAGON equipment on the accuracy of SRIM calculations, quoted to be of the order of 20%, have been reported previously [GRE02]. Listed in table 17 are further results gained within the present work.

Table 17: Measured Energy Loss

Isotope	E_{lab} [keV]	dE_{SRIM} $[eV/10^{15}at/cm^2]$	dE_{meas} $[eV/10^{15}at/cm^2]$	$\frac{dE_{meas}}{dE_{SRIM}}$
^{20}Ne	1160	56.9	61.3 ± 7.5	1.08
^{21}Ne	270	75.0	83.0 ± 3.4	1.11
^{21}Ne	760	63.7	86.9 ± 5.6	1.36
^{24}Mg	220	88.3	83.8 ± 3.1	0.95
^{24}Mg	420	89.3	110.0 ± 4.7	1.23
^{24}Mg	820	81.8	105.0 ± 3.7	1.28

To a first approximation, there seems to be a tendency of measuring a higher energy loss than expected from the SRIM data base, which could hint to a systematic error in the calculated value of the target thickness. Yet, it has to be taken into account that the presented data cannot be counted as 6 independent comparisons. Only three different isotopes are observed. Since the energy loss is dependent on chemical properties, strictly speaking, data on two different elements was evaluated. The presented data essentially agrees with SRIM within the uncertainties quoted for the individual measurements. An energy dependent deviation was not observed. But it is clearly shown that more experimental data is needed to improve the code and study possible systematic deviations to achieve an accuracy required for studies in nuclear astrophysics.

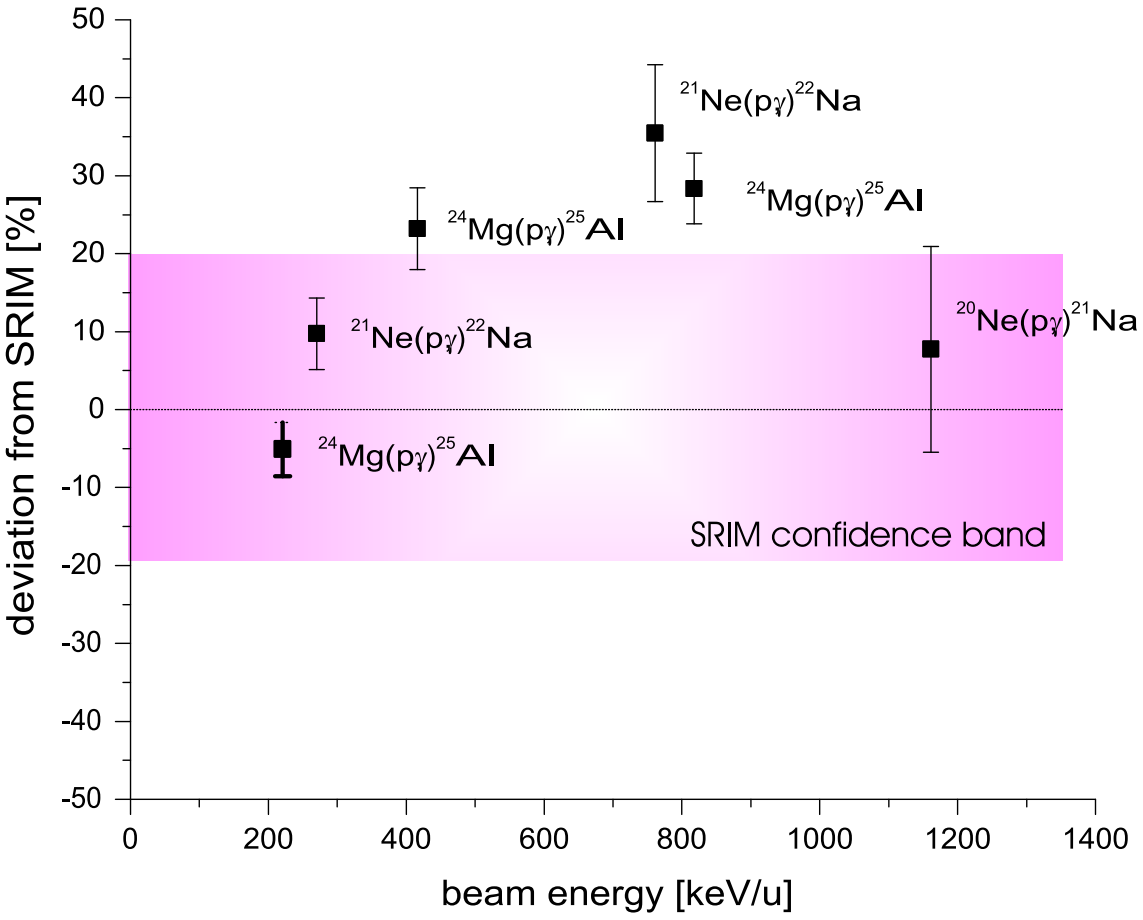

Figure 74: Comparison of measured energy losses with predictions of the SRIM code

8.9.4 Beam Suppression

The main source of leaky beam background is expected to arise from scattered beam particles or ions that went through charge-exchange processes with the residual gas along the full length separator. Simulations have shown that single collisions should not lead to beam particle transport through the final slits. At least two interactions would be necessary, like a double charge exchange. However, methods to simulate "unplanned" background events are not obvious and therefore not necessarily reliable. According to estimates, leaky beam background would have been expected at slightly reduced energies. In contrary to theory, observations during the experiments have shown the only significant source of background at same energy as observed for transmitted beam particles.

The beam suppression achieved in the stable beam tests is shown in figure 75 and table 18. While the black squares indicate the suppression of leaky beam using the DRAGON separator alone, the green triangle suggest an improvement of at least two to three orders of magnitude when requiring recoil-gamma coincidences. It should be remembered that so far the second stage of the recoil separator was merely used for ion transport, not beam suppression. The final slits were usually set wide open, thus offering room for improvements if needed in the future scientific program. Already, the results were sufficient for the experiments conducted so far.

Table 18: Measured Beam Suppression

Reaction	E_{cm} [keV]	E_{lab} [keV/u]	Suppression in Sgls	Suppression in Coin
$^{20}Ne(p,\gamma)^{21}Na$	1112.6	1161	$(2.22 \pm 0.53)\ 10^{-13}$	
$^{21}Ne(p,\gamma)^{22}Na$	258.6	270	$(5.71 \pm 0.01)\ 10^{-9}$	
$^{21}Ne(p,\gamma)^{22}Na$	731.5	761	$(1.37 \pm 0.05)\ 10^{-12}$	
$^{24}Mg(p,\gamma)^{25}Al$	214.0	221	$(3.83 \pm 0.10)\ 10^{-9}$	$(8.80 \pm 1.13)\ 10^{-12}$
$^{24}Mg(p,\gamma)^{25}Al$	402.2	416	$(7.54 \pm 0.62)\ 10^{-10}$	$(2.61 \pm 0.69)\ 10^{-13}$
$^{24}Mg(p,\gamma)^{25}Al$	790.4	818	$(1.82 \pm 0.16)\ 10^{-11}$	

The suppression factor of the separator varies for different energies, which partly arises from beam property changes. Highly energetic beams coming from ISAC show a smaller fractional beam energy spread. Besides, charge exchange and Rutherford cross sections decrease with increasing beam energy, and thus, straggling within the gas target. Therefore, if the low and high energy tails are reduced, the beam suppression should increase. From figure 75 it may be estimated that, within the observed energy range, the suppression increases by almost an order of magnitude with every 200 keV/u. At 1160 keV/u the suppression is above 10^{-12} without coincidence requirements.

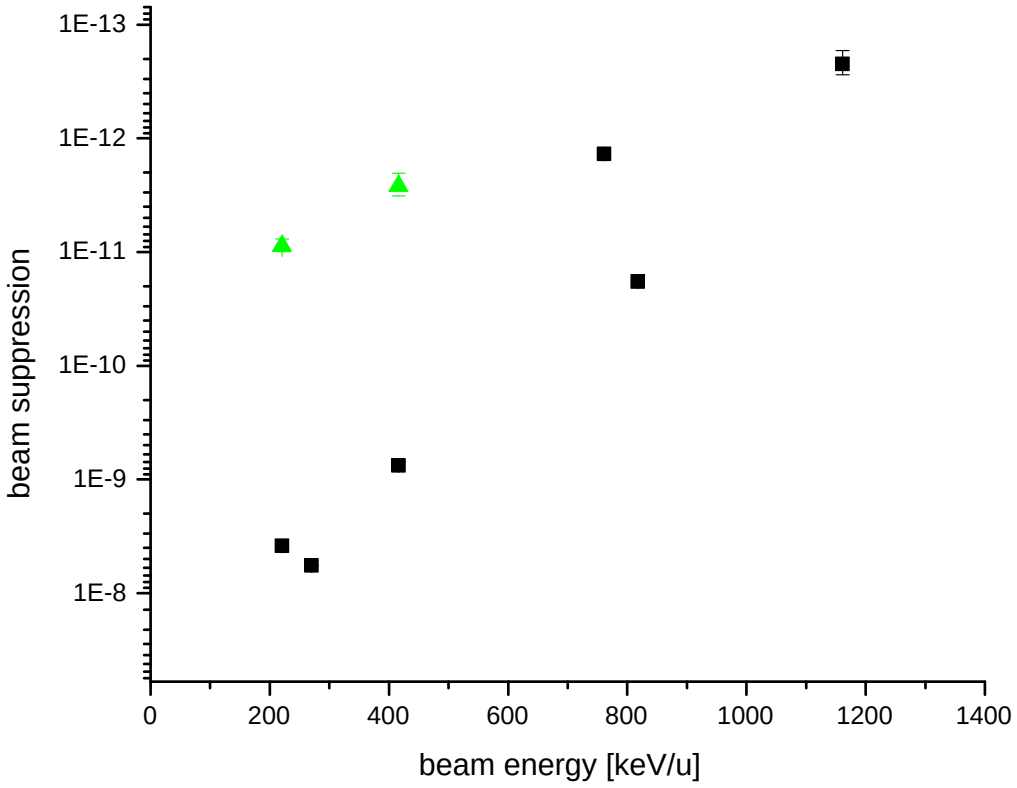

Figure 75: Leaky beam suppression for various stable beam reactions

The goal is to reach a suppression factor of 10^{-15} for the measurement of $^{15}O(\alpha,\gamma)^{19}Ne$ at E_{cm} 150 keV/u. Though the mass difference is 25%, the recoil mass separation from the beam ions is not necessarily enhanced. Strictly speaking it depends on the mass to charge ratio $\Delta\frac{m}{q}$. In the case of $^{24}Mg(p,\gamma)^{25}Al$ the difference is at least 4.2%. Yet for $^{15}O(\alpha,\gamma)^{19}Ne$, $\Delta\frac{m}{q}$ strongly depends on the chosen charge state: When tuning the separator on ^{19}Ne with q = 3+, the next state is ^{15}O at q = 2+ with $\Delta\frac{m}{q}$ = 15%, but tuning on 5+ leads to a difference of only 1.3% to ^{15}O at 4+. Thus, if the charge state distribution allows to chose q = 3+, beam suppression should be enhanced. In any case, a local time-of-flight measurement at the final detector is planned for future experiments. Thus, especially for low energy reactions, the leaky beam suppression will be increased. With the use of a gas ionization chamber for a $\Delta E - E$ measurement, the improved end detector will further discriminate recoils from leaky beam, especially for (α,γ) reactions. Hence, the beam suppression will be increased by a few more orders of magnitude.

8.9.5 Charge State Distribution

The charge state distribution has been measured on four different occasions in the present work, namely, for the ^{21}Na isotope at approximately 1100 keV/u, ^{22}Na at 730 keV/u and ^{25}Al at 430 and 780 keV/u. Since the charge state distribution depends on atomic effects, there should not be a significant difference between different isotopes of the same element at the same energy per unit mass. Studies on the charge state distribution and equilibrium conditions have been conducted previously and are reported elsewhere [LIU02]. To estimate the reliability of theoretical predictions, measured values were compared to the semi-empirical calculations.

It was shown in [LIU02] that the equilibrium charge state distribution follows a Gaussian function, which is characterized by its central point $\bar{q}$ and its width d. $\bar{q}$ may be described by the semi-empirical formula

$$\bar{q} \;=\; Z_p \;\left(1 - \exp(\frac{A}{Z_p^{\gamma}}\sqrt{\frac{E}{\varepsilon}} + B)\right). \tag{66}$$

Here Z_p is the atomic number of the projectile, E its energy in MeV/u, $\varepsilon = 0.067635$ MeV/u, and $\gamma = 0.44515$. For hydrogen targets A is 1.4211 and B = 0.4495.
The charge state distribution width, or standard deviation d, is reported to be not understood, yet. However, it was suggested that, for the reduced charge $\bar{q}/Z_p$ being within the range of 0.3 to 0.7, d should be close to

$$d \;=\; d_1 Z_p^{w}, \tag{67}$$

with $d_1 = 0.23675$ and $w = 0.54772$.

Except for the ^{21}Na isotope at 1100 keV/u, where the reduced charge is 0.78, this assumption was true. Thus, the charge state distribution could be calculated with a Gaussian approach. The parameters obtained by fitting the measured data, displayed in figure 76, were compared to the calculated values in table 19.

Table 19: Fit to the Measured Charge State Distributions

Isotope	E_{lab} [keV/u]	$\bar{q}_{pub}$	d_{pub}	$\bar{q}_{meas}$	d_{meas}
^{21}Na	1100	8.60	0.88	8.64± 0.02	0.57 ± 0.03
^{221}Na	730	7.54	0.88	7.60 ± 0.03	0.41 ± 0.06
^{25}Al	400	6.24	0.96	≈ 6.67	≈ 0.75
^{25}Al	790	8.68	0.96	9.02 ± 0.02	0.96 ± 0.02

It should be noted that for ^{25}Al at 400 keV/u the plotted line is used only to guide the eye and does not indicate a fit to the presented data. Figure 77 provides a more intuitive option for comparing the semi-empirical approach in [LIU02] to the values deduced from the fit.

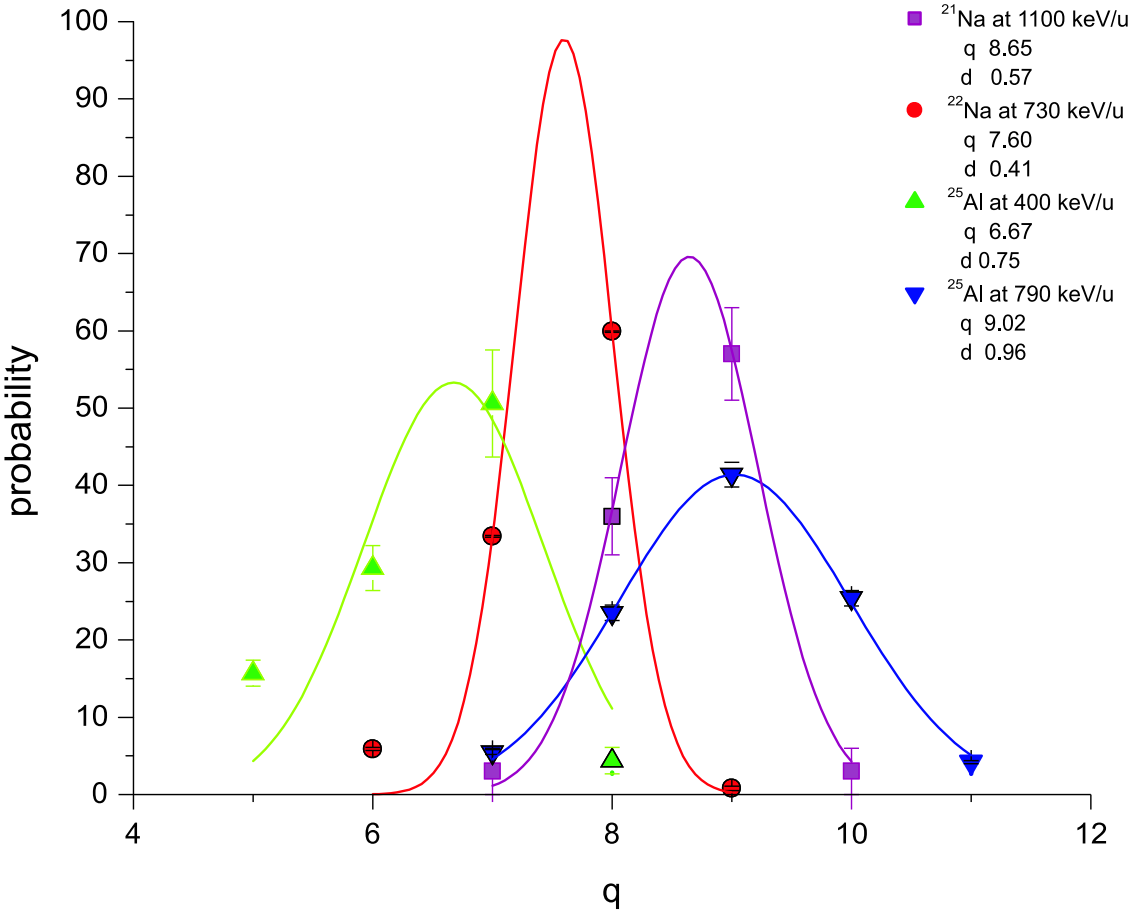

Figure 76: Gaussian fits to the measured charge state distributions

The Gaussian function to describe the charge state distribution in the semi-empirical approach of [LIU02] seems to represent the measured data. Good agreement was also reached for the centroid of the Gaussian distribution. Yet, as already indicated in [LIU02], the width of the distribution remains a source of uncertainty. While the values agree for Al at 790 keV/u, big discrepancies were observed in the case of Na.
The results are listed in table 20. For completeness the last column represents the obtained charge state probability using $\bar{q}$ and d from the Gaussian fit to the measured charge state distribution. Naturally, this value is close to the measured probability.

With the presented results, it becomes obvious that deviations of the measured resonance strength especially in $^{21}Ne(p,\gamma)^{22}Na$ at $E_{cm} = 258.6$ keV might be linked to assumptions made on the charge state probability. It can be concluded that the study to predict charge state distributions offers room for further improvements. In the meantime, for reliable results, the charge state fraction has to be measured and analyzed for each experiment individually.

Table 20: Deviation from Calculated Charge State Probability

Isotope	E_{lab} [keV]	q	p_{calc} [%]	p_{meas} [%]	dev [%]	p_{fit} [%]
^{21}Na	1100	9+	40.8	57 ± 6	42	58.0
^{22}Na	730	8+	39.5	59.9 ± 0.1	53.1	60.5
^{25}Al	400	6+	40.1	29.3 ± 2.9	-10	35.7
^{25}Al	790	9+	39.1	41.4 ± 1.6	6	41.6

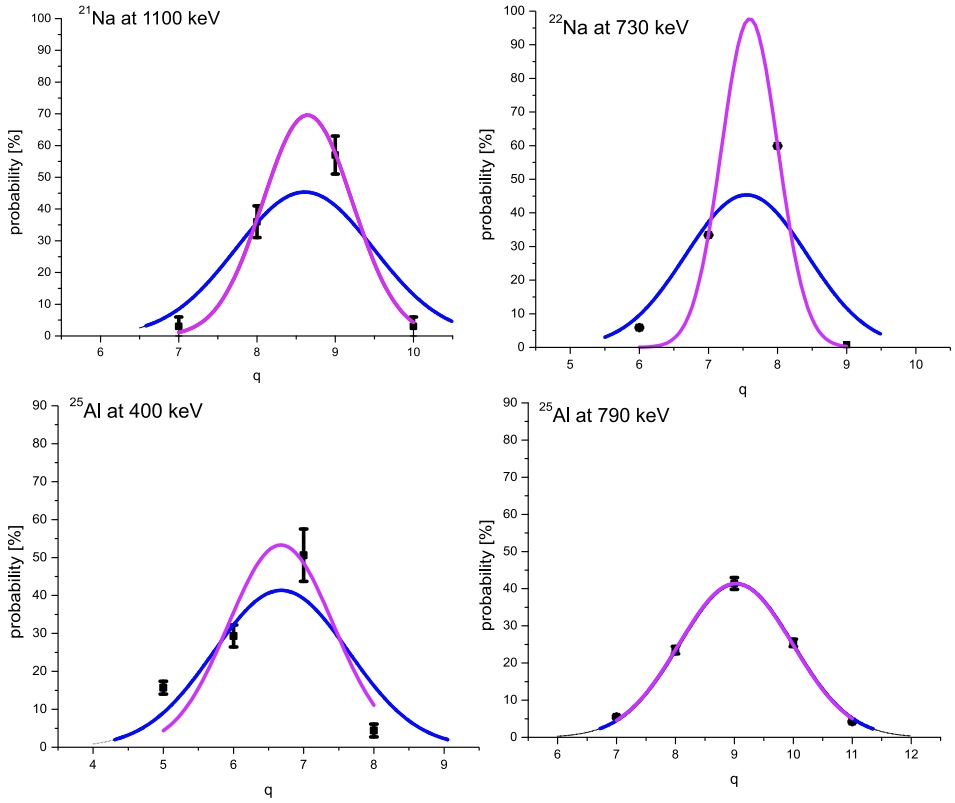

Figure 77: Comparison of predicted (blue) to measured charge state distribution (purple)

8.9.6 BGO efficiency

The BGO efficiency, not strictly part of this thesis, was rather estimated and evaluated for future reference. The easiest data set to try a comparison with GEANT simulations would be resonance at $^{20}Ne(p,\gamma)^{21}Na$ at E_{cm} = 1112.6 keV. Here, a 96% ground state transition is expected with a 3.5 MeV gamma ray and the measured gamma ray spectrum does not show any evidence of background. Thus, the measured 42 ± 4% BGO efficiency is the sum of full, single and double escape in addition to possible Compton scattering events above the threshold of 1.2 MeV.
The comparison with the BGO coincidence spectrum in $^{21}Ne(p,\gamma)^{22}Na$ at E_{cm} 258.6 and 731.5 keV will be tricky, since the observed BGO energy spectrum is a convolution of BGO efficiency for various gamma energies and the distribution of gammas among the different decay branches. Possibly, at E_{cm} = 731.5 keV the full energy peak efficiency for the 78% ground state decay could be compared to the observation. Even though the estimate was done with rather crude methods, it should be good within a 10% uncertainty and definitely allow a rough comparison of reality and simulation.

The second important feature of the BGO array is the function of efficiency versus position that would be worth comparison with a GEANT simulation. As shown in figures 46 and 57 the efficiency drops by approximately 20% from the central value over 25 mm from each side of the target center. Especially when measuring the direct capture or broad resonances in the coincidence mode, this will become an important value for data normalization and has to be further investigated.

The z-mask feature has turned out to be a useful device to track the resonance position roughly within the target. At least within the inner target cell, in the region of ± 30 to 40 mm, it provides a position information of the order of a few mm, as demonstrated for $^{20}Ne(p,\gamma)^{21}Na$ at E_{cm} = 1112.6 keV and $^{21}Ne(p,\gamma)^{22}Na$ at E_{cm} = 731.5 keV and shown in figures 45 and 58. In the case of $^{21}Ne(p,\gamma)^{22}Na$ at E_{cm} = 731.5 keV the range is not quite as wide, because of the natural width of the resonance. However, in order to employ the z-mask feature, decent statistics of about 300 counts are required.
It was suggested to use the z-mask feature to determine the resonance energy for a narrow resonance without mapping at least part of the excitation curve [ROG03]. Once the position is known, the amount of gas up to the center of the resonance could be calculated, and thus, the energy loss within the target material. This method might become useful, when time constraints do not allow the full scan over a resonance. But it should be understood that it cannot be used as an independent energy calibration. Still, the first magnetic bender MD_1 is needed to measure the energy loss, if additional systematic uncertainties of the SRIM data base shall be avoided.

9 Measurement of $^{21}Na(p,\gamma)^{22}Mg$ at E_{cm} = 821 keV

Finally, as a major milestone of the scientific program at ISAC, the $^{21}Na(p,\gamma)^{22}Mg$ reaction was chosen to be the first reaction involving a radioactive beam to be measured at the DRAGON facility. With a reported Q-Value of 5501 keV [END98] and [AUD95], it was planned to populate a strong resonant state at E_x= 6323 keV or at E_{cm} = 821 keV in the ^{22}Mg compound nucleus. Previously, this state had been observed in the $^{24}Mg(p,t)^{22}Mg$ transfer reaction [BAT01], and very recently the TUDA group, also at TRIUMF-ISAC, was able to determine the resonance width by studying the elastic scattering channel in $^{21}Na(p,p')^{21}Na$ at E_{lab} = 863 ± 10 keV/u. The value published was 7^{+4}_{-2} keV in the center of mass frame [RUI02]. The capture reaction parameters are listed in table 21.

Table 21: Parameters of the $^{21}Na(p,\gamma)^{22}Mg$ Reaction

Reaction	Q-Value	E_{cm}	$\Phi_{1/2}$	m_p	m_t
	keV	keV	mrad	amu	amu
$^{21}Na(p,\gamma)^{22}Mg$	5501	≈ 821	7.55	20.998	1.007

9.1 Experimental Procedure

Approximately 1.6 $\cdot 10^{14}$ particles of radioactive ^{21}Na were obtained, integrated over all relevant runs. Beam intensities ranged from 10 to 80 ppA, yet, except for a very few runs, they were usually above 35 ppA. Thus, the normal tuning procedure was followed. Occasionally a stable ^{21}Ne pilot beam from the off-line ion source was employed to tune the separator immediately before the low intensity radioactive beam was delivered.
The resonance excitation curve was mapped over a range of 50 keV/u with typical hydrogen gas target pressures of 4.3 to 4.7 Torr, corresponding to 3.38 to 3.69 $\cdot 10^{18}$ at/cm^2.
Because of the limited bending power of the first magnetic dipole, the beam energy of the incoming q = 5+ beam could not be measured directly. Instead the energy of the outgoing beam was measured for a charge state q = 8+ at different target pressures, thus finding a correspondence of energy loss per pressure unit as shown in figure 78.
The data was fitted with a linear function with a slope of 3.10 ± 0.16 keV/(u Torr), resulting in an energy loss of

$$dE \;=\; (82.8 \pm 4.3) \quad \frac{eV}{10^{15} at/cm^2} \;.$$

This agrees within error with the value calculated by SRIM (72.5 $\frac{eV}{10^{15} at/cm^2}$). Therefore, the total target thickness of 13.4 to 14.6 keV/u was comparable to the total resonance

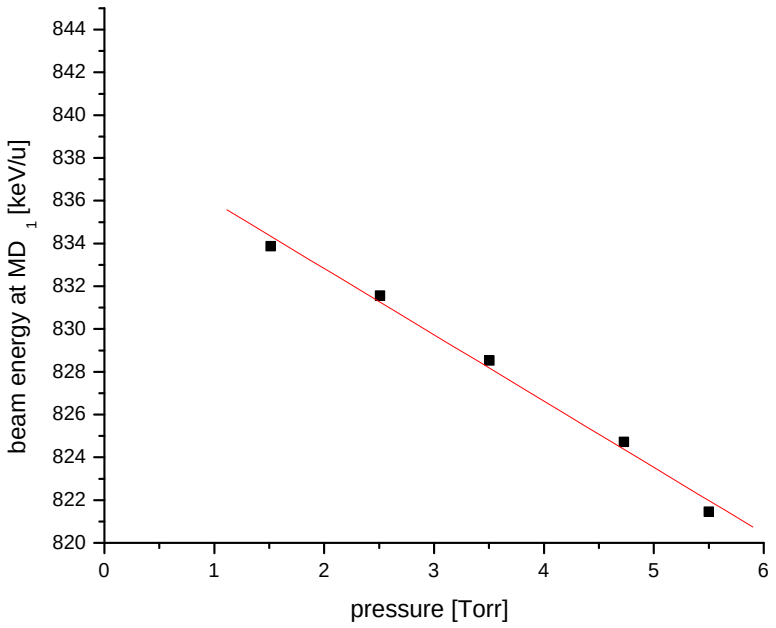

Figure 78: Energy loss in the target for ^{21}Na ions at $E_{lab} \approx 840$ keV/u

width and the thick target yield evaluation could not be applied.

The expected transmission for the recoiling reaction products was calculated based on the commissioning results. Using the reported Q-Value the maximum recoil cone angle $\Phi_{1/2}$ is 7.55 mrad with an energy spread of $\frac{\Delta E}{E} = 1.51\%$ due to the kinematics. This leads to a transmission of 99.5 $\pm$ 0.5 % through the pumping tubes.
The beam spot size at various image points along the DRAGON separator was calculated, employing the results of the previous optics measurements and theoretical values for the linear magnification. A realistic beam diameter of 4 mm diameter in the center of the target with additional angles of 1 mrad in x and y, an additional energy spread of 3.5 keV/u, plus a spread caused by straggling in the gas target (eq. 49). The images are displayed in figure 79. As can be seen, the assumed beam properties lead to a spot size of roughly 12x16 mm^2 at the charge, 4x6 mm^2 at the mass and 16x10 mm^2 at the final slits. Therefore, with the regular slit settings of at least 25 mm opening from the center in QX, QY, and MY, 15 mm for MX and 45 mm in FX and FY, 100% transmission was expected through the DRAGON recoil mass separator.

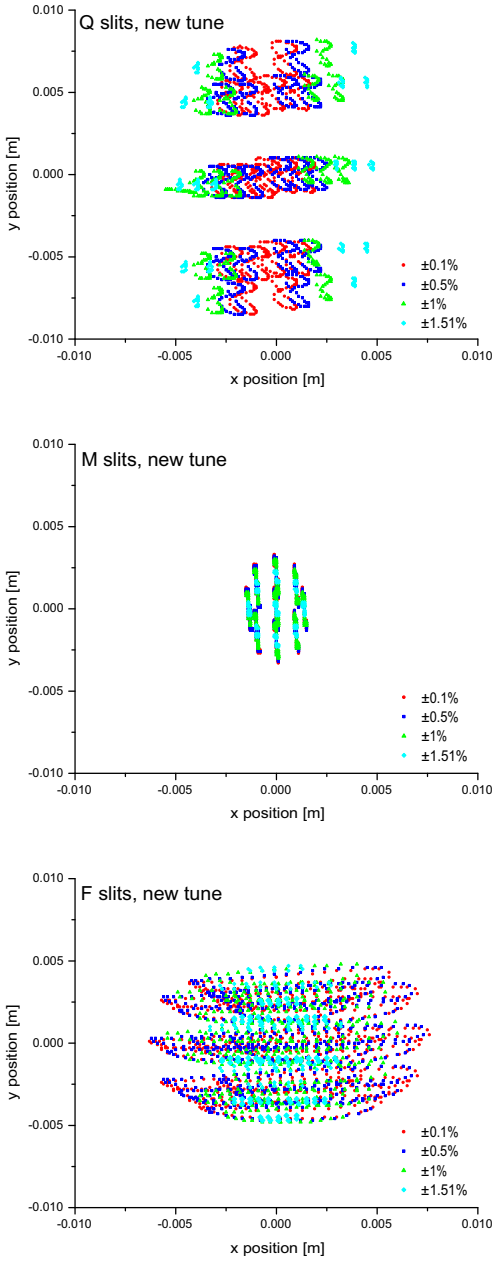

Figure 79: Focus properties of the DRAGON recoil separator at the charge, mass and final slits calculated for a realistic $^{21}Na(p,\gamma)^{22}Mg$ tune at $E_{cm} = 821$ keV

9.2 Exploring the New Resonance

As can be seen from figure 80, the heavy ion energy spectrum in the double sided silicon strip detector was dominated by a strong recoil peak with some contribution of leaky beam background at slightly higher energies. The recoils of interest could easily be distinguished from the leaky beam ions, after applying cuts on the detection time versus the radio frequency of the pre-buncher and the position in the end detector. Upon requiring coincidence with a gamma ray detected in the BGO array, the energy spectrum was essentially free of leaky beam. As before, all events above channel 10000 up to and including the recoil peak, as defined by the coincidence spectrum, were accepted for analysis.

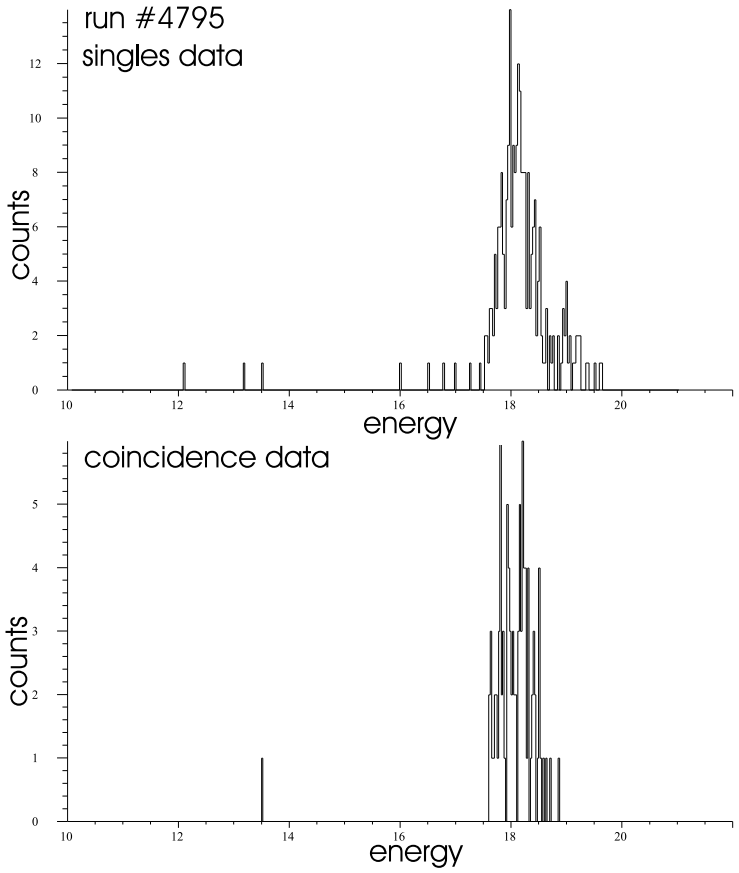

Figure 80: Recoil energy spectrum with and without gamma coincidence requirements for $^{21}Na(p,\gamma)^{22}Mg$ at $E_{cm} = 821$ keV

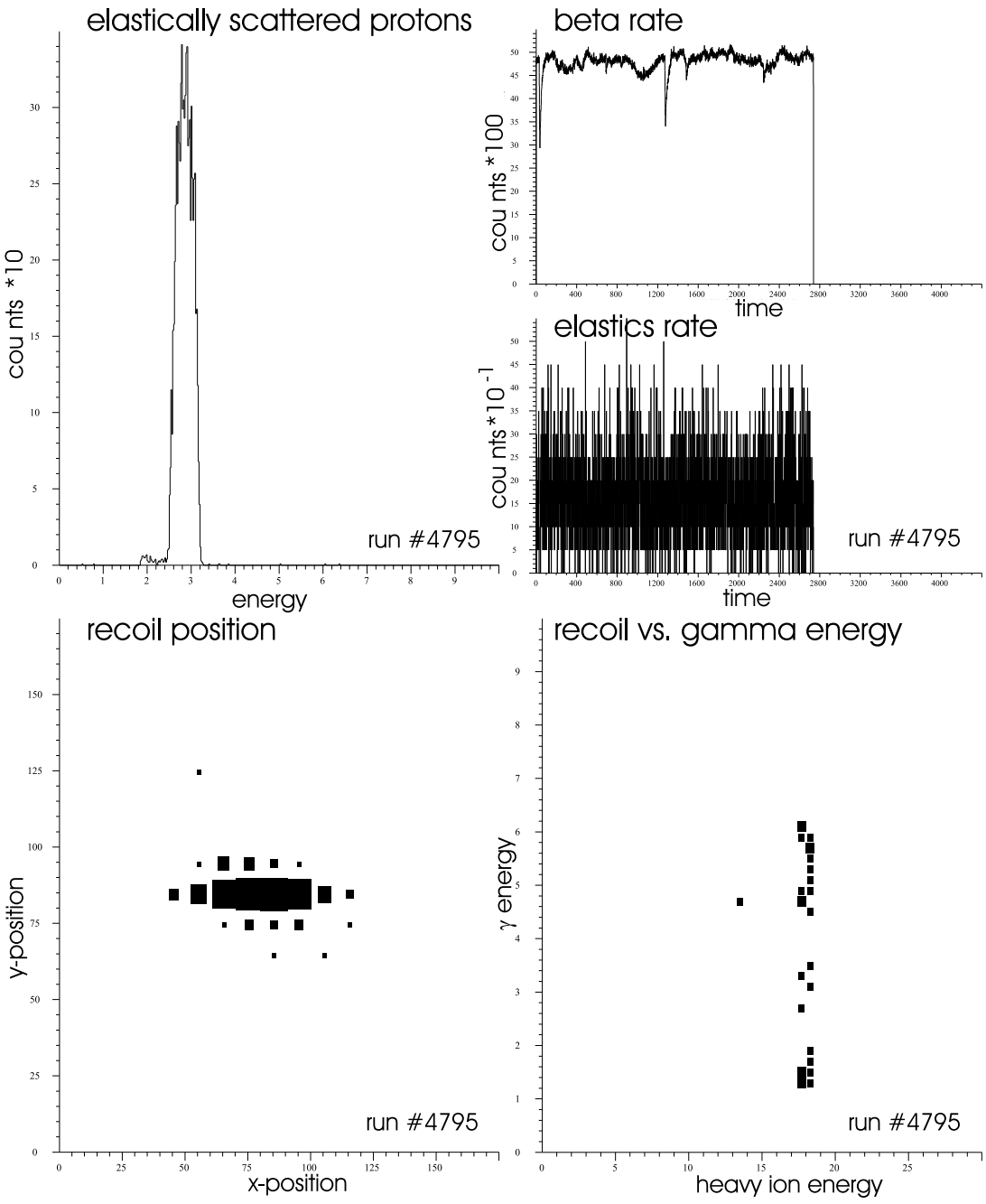

Figure 81: Elastically scattered proton energy spectrum, rates of elastically scattered protons and detected betas over the run time, recoil position in the DSSSD and recoil versus related gamma energy for a typical run of $^{21}Na(p,\gamma)^{22}Mg$ at $E_{cm} = 821$ keV

Radioactive ^{21}Na beam, suppressed at the mass slits, exhibited significant beta activity, that could be observed by the beta monitor positioned after ED_1. The rate in the beta monitor was employed to achieve an overall beam normalization, since at $E_{cm} = 821$ keV the elastic scattering channel $^{21}Na(p, p')$ reaction led to strong deviations from pure Rutherford scattering in the elastic monitor (fig. 82).

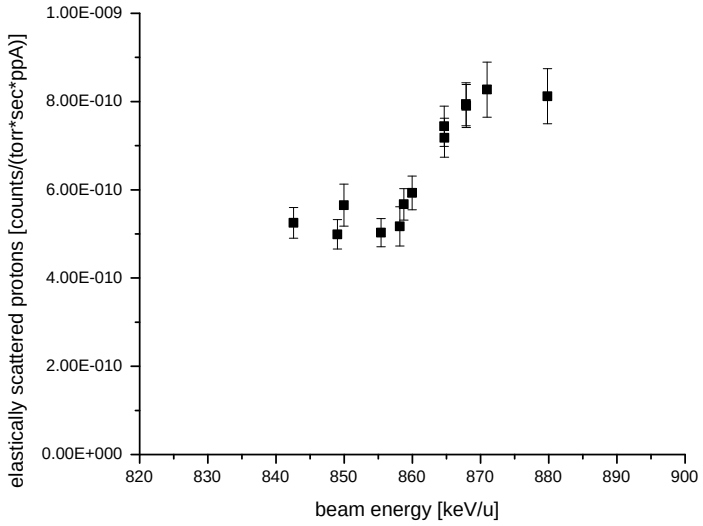

Figure 82: Resonance in the elastic scattering channel $^{21}Na(p, p')$ at $E_{cm} = 821$ keV

In the beta-counter, the 22.5 sec half life of the radioactive ^{21}Na caused an exponential rise of the rate in the beta monitor, which needed at least 180 sec for saturation. Fluctuation in the beam intensity led to similar peaks all through the run (fig. 81). Therefore, it seemed to be unappropriate to average the counts of a certain period after the start of the run to obtain the rate related to the current at the Faradau cup. Instead, the saturation level during the first 20 to 300 sec was chosen as a reference. The good agreement of the current reading at FC4, immediately ahead of the run, compared to the saturation value is shown in figure 83.

To obtain the charge state distribution, the DRAGON was tuned for four different charge states in subsequent runs, each with the same beam energy. Since for some of these runs the beta monitor had not worked properly, the observed recoils were normalized to the total counts in the elastic scattering detector. At a constant beam energy and target pressure, the proton rate in the elastic scattering monitor only dependeds on the beam intensity. The resulting charge state distribution is listed in table 22.

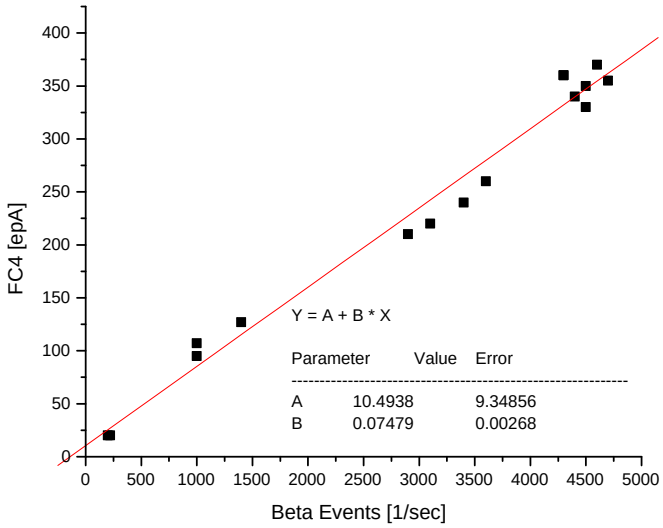

Figure 83: Relation of the current on FC4 to the rate in the beta monitor

Table 22: Charge State Distribution of the ^{22}Mg recoils at E_{lab} 820 keV/u

Charge State	Probability	
7+	7.4 ± 1.3	%
8+	34.0 ± 2.7	%
9+	41.3 ± 3.4	%
10+	17.4 ± 1.9	%

As for stable beam experiments, the recoils were normalized to the effective current, taking into account the 5+ charge state of the incoming beam, run time, dead time, transmission through the pumping tubes, charge state probability for 8+, the efficiency of the DSSSD as well as the loss of good events due to the applied cuts. The latter was normally less than 4 %. Contrary to earlier data analysis, the fit (eq. 33) was performed for two independent variables: pressure and beam energy, while the resonance energy, total width and strength were the resulting parameters. Figure 84 displays the full excitation curve. The χ^2 per degree of freedom was 2.3, not including additional contribution to the individual error bars due to the uncertainty in energy for each run. The resulting resonance parameters are

$$\omega\gamma \ = 555.7 \ \pm 40.7 \ (stat) \pm 65.0; (sys) \quad meV$$

and

$$E_{cm} \ = \ 821.3 \pm 0.9 \quad keV.$$

According to the fit, the total width of the excitation curve is 19.9 ±2.3 keV/u, including the convolution with the energy spread of the incoming beam (tab. 3), zero-point motion or Doppler broadening (eq. 48), and straggling (eq. 49). Assuming $\Gamma_{drv} = 0.67$ keV/u, $\Gamma_{stragg} = 0.3$ keV/u and $\Gamma_{beam} = 3 \pm 1$ keV/u, equation 45 leads to a total measured resonance width of 16.8 ± 2.9 keV/u or, in the center of mass frame,

$$\Gamma_{tot} \;=\; 16.1 \pm 2.8 \quad keV.$$

The determined total width agrees with fits to the elastic scattering data, which are not part of this thesis.

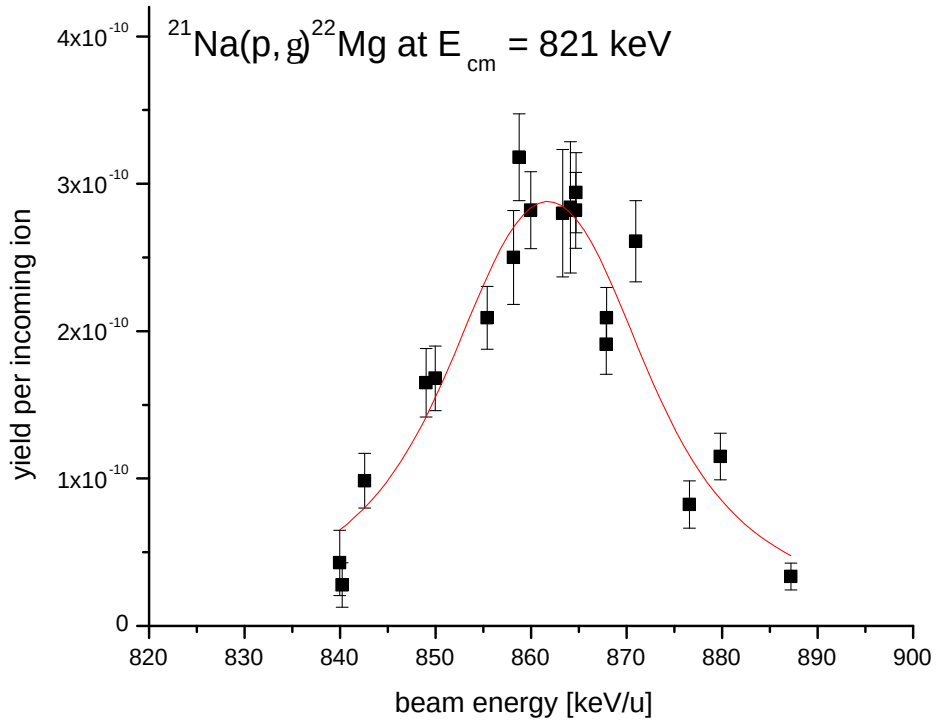

Figure 84: Excitation curve of the $^{21}Na(p,\gamma)^{22}Mg$ reaction at $E_{cm} = 821$ keV

The beam suppression per incoming ion at this energy was measured to be

$$S \;=\; (7.30 \pm 0.89) \cdot 10^{-12}$$

and is comparable to the results obtained with stable beam (fig. 85).

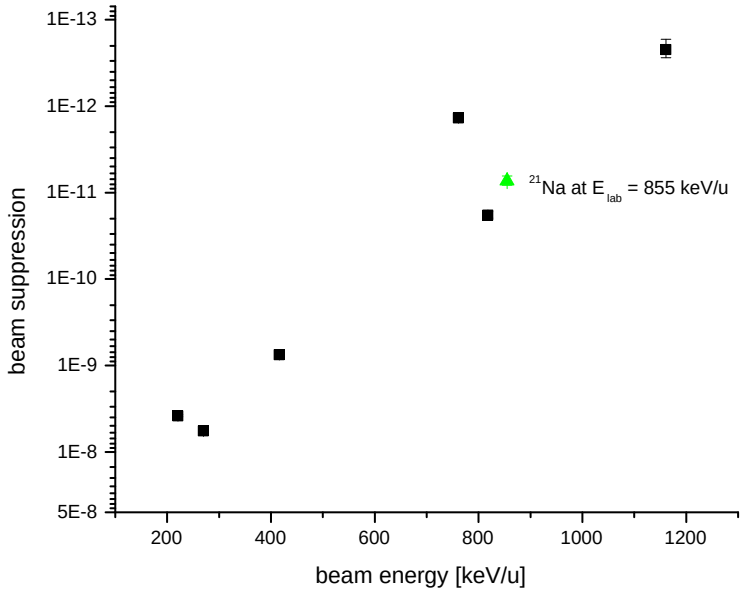

Figure 85: Comparison of beam suppression for stable and unstable beam

9.3 Gamma Branching Ratios

As expected, the BGO gamma array was swamped by 511 keV gamma rays, originating from accumulated radioactive ^{21}Na on collimators and apertures close to the target. Pile-up of the low energy gamma rays in the individual detectors led to events that easily overcame the 0.6 MeV hardware threshold applied to each detector. In the software a threshold of 1.2 MeV was applied, leaving a strong beam-induced peak around 1.5 MeV. Figure 86 displays the sum of several gamma energy spectra, during which the BGO energy calibration remained sufficiently constant. In singles mode, the gammas of interest disappeared in the background. In coincidence mode, when a related recoil event in the DSSSD was required, the gamma energy spectrum showed two separated peaks, well above the background contribution. For the latter, only events with exactly one gamma above threshold were considered.

When comparing the coincidence to the singles events, count rate variation independent of the resonance position appeared. With a resonance width comparable to the target thickness, the gamma yield was not confined to a thin slice within the target material, thus leading to a broader and more complicated efficiency curve. Therefore, no clear relation between efficiency and resonance center position was observed.

The beam induced background was strongly related to the individual accelerator and HEBT tune of each run. Therefore, presumable coincidence events might have originated

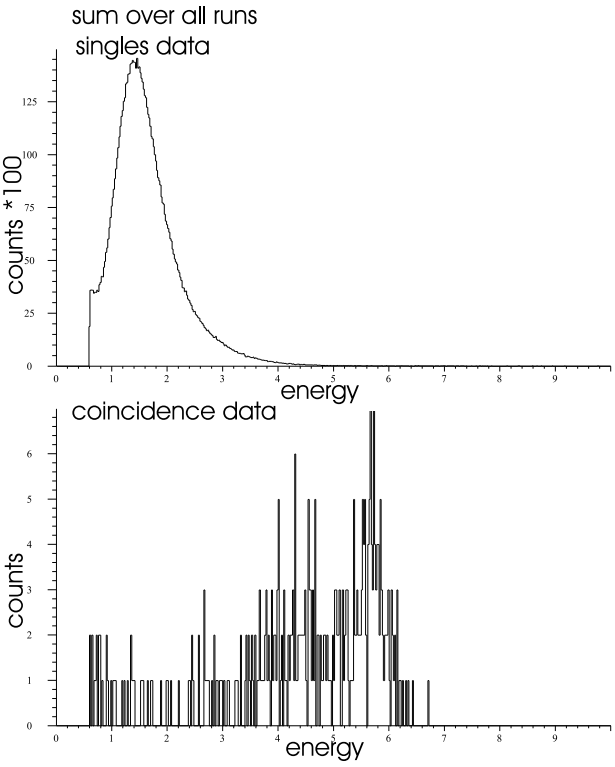

Figure 86: Energy spectrum of the detected gammas with and without coincidence requirements, summed over several runs of $^{21}Na(p,\gamma)^{22}Mg$ at $E_{cm} = 821$ keV

from background gamma events in accidental coincidence with a recoil detection. Those events should cluster just below the background peak and could therefore appear as events in coincidence with a 2 to 3 MeV gamma. To achieve a reliable BGO efficiency with radioactive beam experiments in future experiments, a very careful tuning procedure, possibly in combination with additional gamma energy cuts in the later analysis, may be required. In the case presented, only the recoil singles event were needed for the analysis, and the obtained results are independent of the BGO efficiency.
Despite those difficulties, the gamma energy spectrum may be used for further analysis. Some assumptions can be made in order to confine possible peak positions. Assuming that the higher channel peak around channel 5700 is most likely related to a ground state transition with $E_\gamma = 6.3$ MeV, the lower energy peak around channel 4300 would have an energy of roughly 4.8 MeV. Yet, no state is known in ^{22}Mg at 1.6 MeV. The first excited state is measured to sit significantly lower at 1.3 MeV. A transition to the first excited state would involve a 5.1 MeV gamma, observable in channel 4600, leaving a second peak at channel 4000 or 4.4 MeV open to further interpretation. Since no state is known at 1.9 MeV, the latter can not be related to the first branch of a decay. But populating the state

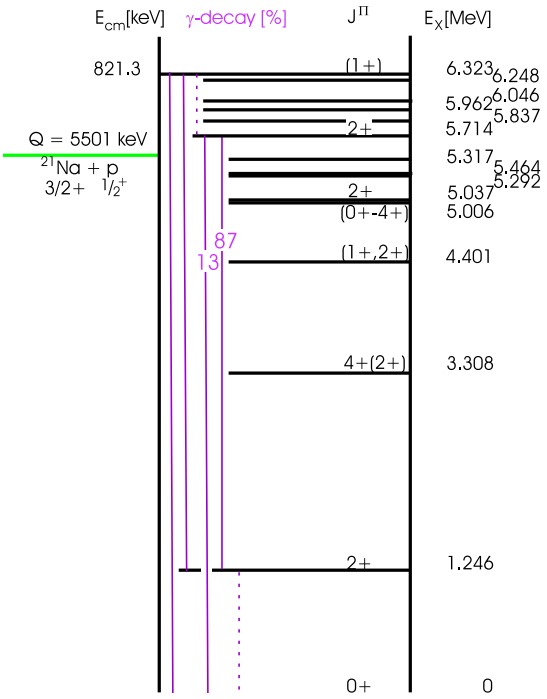

Figure 87: Decay scheme of the ^{22}Mg excited state at $E_x = 6.23$ MeV.

at 5.7 MeV would result in a first gamma well below threshold, while this state is known to decay with a strength of 87% to the first excited state [FIR96], leading to a strong 4.5 MeV gamma line.
Efforts were made to fit the spectrum, starting with three independent Gaussian peaks centered at channels 5700, 4600 and 4000 and requiring the same peak width. The results are shown in figure 88 and listed in table 23, assuming equal detection efficiency for all gamma energies and including a 87% decay probability for the 4.4 MeV transition. It should be mentioned that the given errors for the transition strength only include uncertainties in the fit. Realistic errors need to include transition to hidden branches not observed because of either a low probability or including cascades of gammas below threshold.

Table 23: Branching Ratios for ^{22}Mg at $E_x = 6323$ keV

Peak	Position [ch]	E_γ [MeV]	Area	Strength [%]
1	5663 ± 18	6.3	100 ± 5	50 ± 5
2	4582 ± 44	5.1	55 ± 6	28 ± 4
3	3840 ± 61	4.3	39 ± 6	22 ± 4

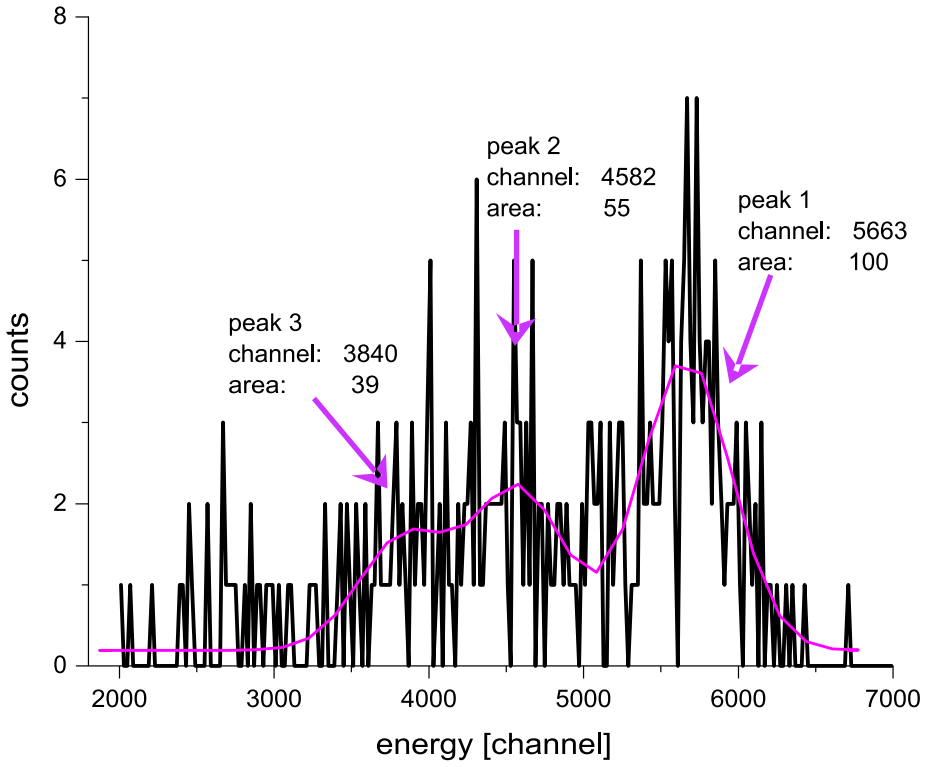

Figure 88: Fit to the coincidence gamma energy spectrum for $^{21}Na(p,\gamma)^{22}Mg$ at E_{cm} = 821 keV

9.4 Influence on Nuclear Astrophysics

As discussed earlier, $^{21}Na(p,\gamma)^{22}Mg$ is assumed to sit on the main path of the nucleosynthesis in X-ray bursts (fig. 4). Thus, the contribution of a single resonance becomes obvious when comparing the lifetime (eq. 19) of ^{21}Na against destruction via proton capture, with and without including that particular resonance in the calculations. In plot 89 the lifetime is calculated for an X-ray burst scenario, assuming a density of 10^5 g/cm^3 and a proton mass fraction of 0.5 [SCH02]. In addition to the calculated non-resonant lifetime, both scenarios with and without the resonance at E_{cm} = 821 keV are indicated. Preliminary values, obtained from measurements with DRAGON on the lower resonances, were included in the calculation (table 24).
It can be seen that the presence of the strong resonance at E_{cm} = 821 keV influences the ^{21}Na lifetime already around 0.8 GK; by 3 GK it reduces the lifetime by one order of magnitude. However, the non-resonant lifetime alone is well below the region of beta decay. Since $\tau_\beta \gg \tau_{non-resonant}$ resonances would not be required to bypass the β-decay of ^{21}Na. If the β-decay would be the only competing path, the reaction could depend solely on the non-resonant proton capture. Thus, in principle, resonances would not be

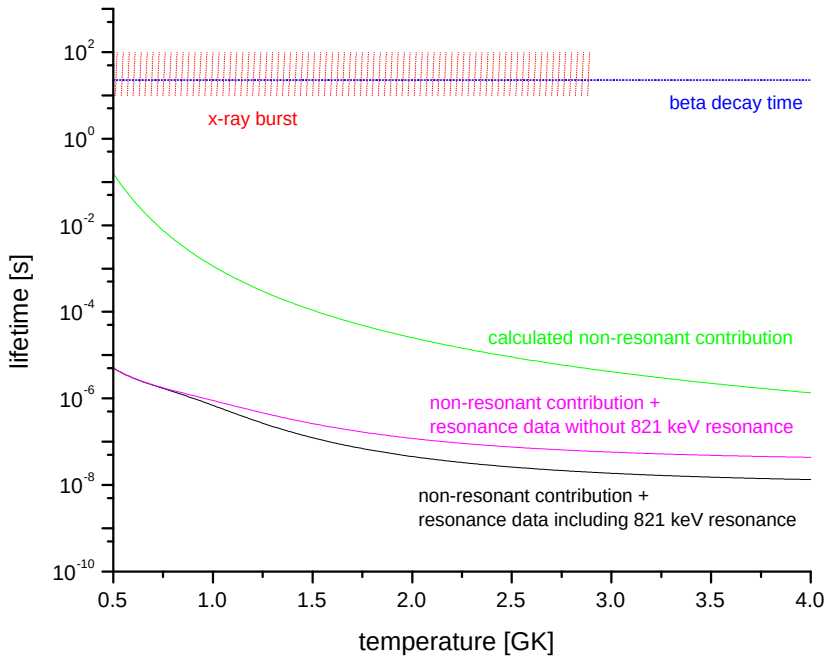

Figure 89: Plot of ^{21}Na lifetime versus temperature under X-ray burst conditions

important to the nucleosynthesis. Yet, concurrent reactions like $^{21}Na(\alpha, p)$ and $^{21}Na(\alpha, \gamma)$ may reduce the ^{21}Na lifetime in addition to the beta-decay. Thus, it is subject to further studies on alternative capture reactions to show the influence of the 821 keV resonance.

Table 24: Preliminary DRAGON Results on $^{21}Na(p, \gamma)^{22}Mg$ Resonances Below E_{cm} = 821 keV [BIS02]

E_{cm} [keV]	$\omega\gamma$ [meV]
205	1
460	0.2
544	8
746	171

10 Discussion and Conclusion

An extensive program for commissioning studies of the new DRAGON experimental set-up was accomplished with stable beams: The properties of the ion beam were determined and an energy measurement of the beam was established. Measurements of the gas target system as well as transmission studies through pumping tubes and the recoil mass separator were completed. Finally, the overall performance of the DRAGON facility was studied with a set of resonant reactions. Thus, the instrumental error was reduced for future experiments, once charge state distribution and energy loss are determined.

New data, taken and analyzed for the $^{24}Mg(p,\gamma)^{25}Al$ reaction at E_{cm} = 790 keV, rather supports earlier studies [KEI80] than the latest values achieved by re-normalization in [POW99]. For the first time, the $^{21}Na(p,\gamma)^{22}Mg$ at E_{cm}= 821 keV was studied directly with a radioactive ion beam and could be assigned a resonance energy, width and strength. This advancement was not only important for nuclear astrophysics where, according to the present understanding, this resonance might contribute to the element synthesis in X-ray bursts. It was also a milestone for the DRAGON facility. Here, for the first time, a resonant capture experiment involving a high intensity radioactive beam was successfully accomplished.

Completing the present work are two unanticipated new results on the $^{21}Na(p,\gamma)^{22}Mg$ reaction. These were achieved from extensive commissioning studies building up a certainty in the data derived from DRAGON experiments. Earlier, the comparatively narrow resonance width studied via $^{21}Na(p,p')^{21}Na$ at E_{cm} = 821 keV [RUI02] showed a significant discrepancy with the DRAGON result. This led to a re-analysis of the TUDA scattering data. A much broader resonance width than originally published was confirmed [RUI03], agreeing now with the DRAGON values analyzed in the present work.
In addition a deviation of 7 keV from the published value of the $^{21}Na(p,\gamma)^{22}Mg$ resonance energy at 212 keV was observed. Although several groups had independently confirmed the excitation energy in the ^{22}Mg nucleus in various transfer studies [ROL72], [BAT01], [CHE01], [VIS02], no error in the DRAGON energy calibration could be found. Though the study of this resonance was not actually part of the present thesis, the energy calibration was. Further investigation showed that the error is likely to be related to a discrepancy of the Q-value from literature [AUD95]. It has been pointed out [HAR02] that this value was obtained from measurements of the ^{22}Mg mass excess [NOL74], [HAR74], which have not been updated to account for recent and significant changes in the calibration reaction energies. An updated Q-value is consistent with the present results and the results of new studies on super-allowed $\beta-$decays of ^{22}Mg [HAR03]. A study at Yale tried to confirm the new results, measuring simultaneously the (p,p'), (p,d) and (p,t) reaction on $^{14,15}N$, ^{12}C, ^{16}O and $^{24,25}Mg$ with the Enge split-pole spectrometer. The analysis is still ongoing. In addition, new measurements on the ^{22}Mg mass are planned for the near future [HAR02].

A List of Run Numbers

Table 25: List of Run Numbers

Study	Run Numbers	Logbook	Pages
Beam Properties	1359 - 1504	2	146 - 189
Energy Calibration	4932 - 4950	5	74 -86
	5131 - 5163	6	99 - 113
Target Profile	1214 - 1252	2	98 - 123
Target Thickness		7	8 - 11
Transmission		6	1 - 12
Separator Optics	18 - 339	6	13 -79
$^{20}Ne(p,\gamma)^{21}Na$ E_{cm} = 1112.6 keV	5170 - 5204	6	119 - 146
$^{21}Ne(p,\gamma)^{22}Na$ E_{cm} = 258.6 keV	4955 -4990	5	89 - 118
	5212 - 5218	6	148 - 158
$^{21}Ne(p,\gamma)^{22}Na$ E_{cm} = 731.5 keV	6911 - 6938	9	18 - 41
$^{24}Mg(p,\gamma)^{25}Al$ E_{cm} = 214.0 keV	6832 - 6883	8	146 - 187
$^{24}Mg(p,\gamma)^{25}Al$ E_{cm} = 402.2 keV	6053 - 6113	7	50 - 82
$^{24}Mg(p,\gamma)^{25}Al$ E_{cm} = 790.4 keV	5268 - 5300	6	172 - 192
$^{21}Na(p,\gamma)^{22}Mg$ E_{cm} = 821 keV	4788 - 4835	4	125 - 155
	5059 - 5060	5	178 - 180
	6211 - 6214	7	142 - 150
	6284 - 6288	8	20 -28

References

[AMA01] S. Amari et al., *Astrophys. J.* 551 (2001) 1065;

[AMA03] P.-A. Amaudruz & S. Ritt, see http://midas.triumf.ca or http://midas.psi.ch for details;

[AMS83] G. Amsel & B. Maurel, *Nucl. Instr. & Meth.* 218 (1983) 183;

[ANG99] C. Angulo et al., *Nucl. Phys.* A 656 (1999) 3, NACRE compilation;

[AUD95] G. Audi & A.H. Wapstra, *Nucl. Phys.* A 595 (1995) vol. 4, 409;

[BAT01] N. Bateman et al., *Phys. Rev.* C 63 (2001) 035803;

[BER77] H.L. Berg et al., *Nucl. Phys.* A 276 (1977) 168;

[BET37] H.A. Bethe & G. Placzek, *Phys. Rev.* 51 (1937) 450;

[BIE00] J.P. Biersack & L. Haggmark, *Nucl. Instr. & Meth.* 174 (1980) 257 and http://www.srim.org SRIM 2000;

[BIS02] Shawn Bishop, PhD thesis, to be submitted to Simon Fraser University, Burnaby, Canada;

[BIS03] S. Bishop et al., *The* $^{21}Na(p,\gamma)^{22}Mg$ *Reaction and Oxygen-Neon Novae*, submitted to Phys. Rev. Letters, 2003;

[BLO69] R. Bloch, T. Knellwolf & R.E. Pixley, *Nucl. Phys.* A 123 (1969) 129;

[BOR99] L. Borucki et al., *Eur. Phys. J.* A 5 (1999) 327;

[BRU94] R. Brun et al., *GEANT3 Users Guide*, CERN Program Library (1994) W5013;

[BUR57] E.M. Burbidge, G.R. Burbidge, W.A. Fowler & F. Hoyle, *Rev. Mod. Phys* 29 (1957) 547;

[CAG02] J.A. Caggiano, et al., *Phys. Rev.* C. 65 (2002) 055801,

[CHE01] A.A. Chen et al., *Phys. Rev.* C 63 (2001) 065807;

[END98] P.M. Endt, *Nucl. Phys.* A 633 (1998) 1;

[FIR96] R.B. Firestone, *Table of Isotopes*, ed. V.S. Shirley, Wiley-Interscience publication, New York (1996);

[GAM28] G. Gamow, *Z. Phys.* 51 (1928) 204;

[GIG03] Dario Gigliotti, *Calibration and Simulation of a Gamma Array for DRAGON at ISAC*, master thesis to be submitted to University of Northern BC, Prince George, Canada

[GLA97] S.A. Glasner, E. Livine & J.W. Truran, *Astrophys. J.* 475 (1997) 754;

[GOE82] J. Görres et al., *Nucl. Phys.* A 385 (1982) 57;

[GRE02] U. Greife et al., *Energy loss of stable and radioactive ions in hydrogen gas*, submitted to Nucl. Instr. & Meth. in Phys. Res. B;

[HAR74] J. Hardy et al., *Phys. Rev.* C 9 (1974) 252;

[HAR02] John Hardy, Texas A&M University, private communication;

[HAR03] J.C. Hardy et al., *High Precision Measurement of Superallowed* $0^+ \rightarrow 0^+ \beta$ *Deacy of* ^{22}Mg, to be published in Phys. Rev. Let.;

[HOR88] K.M. Horn & W.A. Lanford, *Nucl. Instr. & Meth. in Phys. Res.* B 29 (1988) 609;

[HUT02] D. Hutcheon et al., *Nucl. Instr. & Meth. in Phys. Res.* A 498/1-3 (2003) 190;

[ILI02] C. Iliadis et al., *Astrophys. J. Suppl.* 142 (2002) 105;

[IYU95] A.F. Iyudin et al., *Astro. Astrophys.*, 300 (1995) 422;

[JOS99] J. José, A. Coc & M. Hernanz, *Astrophys. J.* 520 (1999) 437;

[KEI80] J. Keinonen & S. Brandenburg, *Nucl. Phys.* A 341 (1980) 345;

[KEI01] R. Keitel et al., *Status Update on the ISAC Control System*, Proceedings of the 8th International Conference on Accelerator and Large Experimental Physics Control Systems, ICALEPCS, ed. H.Shoaee (2001);

[KOW87] S.B. Kowalsky & H.A. Enge, *Nucl. Inst. & Meth.* A 258 (1987) 407;

[LAX01] R.E. Laxdal, *ISAC at TRIUMF: Status of the Post-Accelerator*, Proceedings of the PRORIB Conference, (2001);

[LIU02] W. Liu et al., *Nucl. Instr. & Meth. in Phys. Res.* A 496 (2003) 198;

[MAR57] J.B. Marion & W.A. Fowler, *Astrophys. J.* 125 (1957) 221;

[NOL74] J. Nolan et al., *Nucl. Instr. & Meth.* 115 (1974) 189;

[NOV] NOVA is a public domain, TRIUMF maintained program, see http://daq.triumf.ca/nova for details;

[PAW] see http://wwwinfo.cern.ch/asd/paw for details;

[POW99] D.C. Powell et al., *Nucl. Phys.* A 660 (1999) 349;

[ROG03] Joel Rogers, TRIUMF Laboratory, private communication;

[ROL72] C.E. Rolfs et al., *Nucl. Phys.* A 191 (1972) 209;

[ROL74] C. Rolfs & W.S. Rodney, *Nucl. Phys.* 235 (1974) 450;

[ROL88] C.E. Rolfs & W.S. Rodney, *Cauldrons in the Cosmos*, The University of Chicago Press, Chicago & London (1988);

[RUI02] C. Ruiz et al., *Phys. Rev.* C 65 (2002) 042801;

[RUI03] Chris Ruiz, Edinburgh University, private communication;

[SCH02] Hendrik Schatz, Michigan State University, private communication;

[STA89] S. Starrfield, *Classical Novae*, eds. M.F. Bode & A. Evans, Wiley, New York (1989);

[TRA75] H.P. Trautvetter, *Nucl. Phys.* A 243 (1975) 37;

[VIS02] Dale Visser, Anuj Parikh & Peter D. Parker, Wright Nuclear Structure Laboratory, Yale University, private communication;

[WEI90] A. Weiss & J.W. Truran, *Astr. Astrophys.* 238 (1990) 178;

[WRE02] C. Wrede et al. *Double Sided Silicon Strip Detector as an End Detector for DRAGON*, accepted for Nucl. Inst. & Meth;

[WIE98] M. Wiescher, H. Schatz & A.E. Champagne, *Phil. Trans. R. Soc. Lond.* A 356 (1998) 2105;

[WOL87] H. Wollnik, J. Brezina & M. Berz, *Nucl. Instr. & Meth.* A 258 (1987) 408;

[ZIN95] E. Zinner *Interstellar grains from primitive meteorites: New constraints on nucleosynthesis theory and stellar evolution models*, eds. M. Busso, R. Gallino & C.M. Raitieri, Proceedings of the Nuclei in the Cosmos III Conference, AIP Conference Proceedings vol. 327, AIP Press, Washington D.C. (1995) 567.

Acknowledgements

First and foremost, I would like to thank my supervisor John D'Auria. With his very special combination of candid temperament and charming encouragement he pushed me to maximum capacity in the work, while aspiring affection for that work I have been accomplishing over the complete course of my thesis project.

Many thanks I owe to Uwe Greife who, through his own initiative, offered me the chance to study in one of the world's leading facilities in Nuclear Astrophysics. During his many visits, he also vigorously supported my experimental studies, my personal development as a scientist and the progress of this thesis.

I would also like to express my gratitude to Dave Hutcheon. He never hesitated to share his amazing knowledge and rich experience with me. He listened carefully to my ideas and answered my questions with great patience and understanding.

Professor Claus E. Rolfs provided financial support and allowed me to complete this thesis under his name and professorship. I am grateful for his confidence in me.

And I thank Frank Strieder, who sustained the advancement of my PhD and kept the connection to the Bochum group alive through his visits and emails.

Special thanks also to Alan Chen for many scientific and personal talks over numerous cups of espresso coffee.

Furthermore, I would like to thank the DRAGON crew, especially Lothar Buchmann and Mohan Chatterjee, as well as Shawn Bishop, Dario Gigliotti, Don Hunter, Cybele Jewett, Naimat Khan, Alison Laird, Mike Lamey, Wenjie Liu, Art Olin, Dave Ottewell, Joel Rogers, Hart Sprenger and Chris Wrede. Each contributed their own individual ideas and labor to this project and helped banish the tedium from our weekly meetings through spirited discussion and vivid arguments.

Peter Machule and Doug Preddy offered endless help with little and not so little problems, delicious lunches and a laugh or two during the daily routine.

Dustin Lang largely participated in the commissioning studies of the DRAGON optical equipment.

The TRIUMF technical staff have earned my applause. They are the hidden heros that keep the facility going, particularly in the machine and electronics shops, computer support, beam lines, controls group, design office, and cyclotron division. Of course the ISAC operations group, with Bob Laxdal and Matteo Pasini, is the part of the staff to which I am especially indebted.

Finally, Hanns-Peter Trautvetter has won my respect for chivalrously standing in as a co-corrector for this thesis.

Very personal thanks I owe to my family, my Mum, my Dad, my sister Anna and my grannies. They never stopped encouraging me. Whether it was during fond conversations on the phone or care parcels sent half way around the world, their expressions of warmth helped assure me that I was never alone.

I have appreciated the great time I enjoyed in beautiful British Columbia thanks largely to the friends and acquaintances I found here: above all Jutta Escher as well as Mark & Dante, Abby, Jutta, Wolfgang & Henry, Gail, Lexi, Eric & Lisa, Pierre & Candide, Carol & Jens, Nathalie, Debbie, Jürgen, Christine, Jens, Sabine, Jan Lukas & Lea, Leslee & Orrin.

And I am grateful to my friends back in Germany Alex, Moni, Mela, Sandra, Vivi & Guido, Nicole & Markus, Sanne, André, Tina, Christel, Veit, Claudia, Martina, Nadyah, and Mac for not forgetting me, but keeping in close touch even over such a long distance and such a long time.

Last but not least I wish to thank my dear friend and husband Thomas, who never complained no matter how late the shift ended, but always believed in me and who supported my work with unwearying care.

Curriculum Vitae

Personal Data:

Birthday and -place:	13th of March 1974, Aachen, Germany
Parents:	Marlies Theis, née. Risthaus and Dr. Wolfgang Theis
Marital Status:	married

Education:

1980 - 1984	Gemeinschaftsgrundschule An der Trooststraße, Mülheim an der Ruhr, Germany
1984 - 1990	Städtisches Gymnasium Luisenschule, Mülheim an der Ruhr, Germany
1989 - 1990	Public High School Falls City High School, Falls City, TX, USA
1990 - 1993	Städtisches Gymnasium Clara-Schumann-Gymnasium, Bonn, Germany
June 1993	Abitur Clara-Schumann-Gymnasium, Bonn, Germany

University

June 1995	Vordiplom in Physics and Astronomy Rheinische Friedrich-Wilhelms-Universität, Bonn, Germany
April 1999	Diplom in Nuclear Astrophysics Ruhr-Universität, Bochum, Germany
since Sep. 1999	Dissertation Ruhr-Universität, Bochum, Germany TRIUMF Laboratory, Vancouver, Canada

Internships:

Aug. 1997 - Sep. 1997	Sommerstudium Deutsches Elektronen-Synchrotron, DESY, Hamburg, Germany
Oct. 1997 - Feb. 1998	Sokrates Stipendium Observatoire de Paris, France

Publications

Nuclear Astrophysics Studies at DRAGON: The $^{21}Na(p,\gamma)^{22}Mg$ Reaction and Oxygen-Neon Novae
S. Bishop, R.E. Azuma, L. Buchmann, A.A. Chen, M.L. Chatterjee, J.M. D'Auria, S. Engel, D. Gigliotti, U. Greife, M. Hernanz, D. Hunter, A. Hussein, D. Hutcheon, C. Jewett, J. José, J. King, S. Kubono, M. Lamey, R. Lewis, W. Liu, S. Michimasa, A. Olin, D. Ottewell, P.D. Parker, J. Rogers, F. Strieder, C. Wrede
submitted to Phys. Rev. Let.;

The DRAGON Facility for Nuclear Astrophysics at TRIUMF-ISAC: Design, Construction and Operation
D.A. Hutcheon, S. Bishop, L. Buchmann, M.L. Chatterjee, A.A. Chen, J.M. D'Auria, S. Engel, D. Gigilotti, U. Greife, D. Hunter, A. Hussein, C.C. Jewett, N. Khan, M. Lamey, A.M. Laird, W. Liu, A. Olin, D. Ottewell, J. Rogers, G. Roy, H. Sprenger, C. Wrede
Nucl. Instr. & Meth. in Phys. Res. A 498/1-3 (2003) 190;

Energy Loss of Stable and Radioactive Ions in Hydrogen Gas
U. Greife, S. Bishop, L. Buchmann, M.L. Chatterjee, A.A. Chen, J.M. D'Auria, S. Engel, D. Gigliotti, D. Hunter, D.A. Hutcheon, A. Hussein, C.C. Jewett, A.M. Laird, M. Lamey, W. Liu, A. Olin, D. Ottewell, J. Rogers, C. Wrede
submitted to Nucl. Instr. & Meth. in Phys. Res. B;

Charge State Studies of Low Energy Heavy Ions Passing Through Hydrogen and Helium Gas
W. Liu, G. Imbriani, L. Buchmann, A.A. Chen, J.M. D'Auria, A. D'Onofrio, S. Engel, L. Gialanella, U. Greife, D. Hunter, A. Hussein, D.A. Hutcheon, A. Olin, D. Ottewell, D. Rogalla, J. Rogers, M. Romano, G. Roy, F. Terrasi
Nucl. Instr. & Meth. in Phys. Res. A 496 (2003) 198;

The E1 capture amplitude in $^{12}C(\alpha,\gamma)^{16}O$
L. Gialanella, D. Rogalla, F. Strieder, S. Theis, G. Gyrky, C. Agodi, M. Aliotta, L. Campajola, A. Del Zoppo, A. D'Onofrio, P. Figuera, U. Greife, G. Imbriani, A. Ordine, V. Roca, C. Rolfs, M. Romano, C. Sabbarese, P. Sapienza, F. Schümann, E. Somorjai, F. Terrasi. and H.-P. Trautvetter
Eur. Phys. J. A 11 (2001) 357;

Recoil separator ERNA: ion beam purification
D. Rogalla, S. Theis, L. Campajola, A. D'Onofrio, L. Gialanella, U. Greife, G. Imbriani, A. Ordine, V. Roca, C. Rolfs, M. Romano, C. Sabbarese, F. Schümann, F. Strieder, F. Terrasi, and H.-P. Trautvetter
Nucl. Instr. & Meth. A 437 (1999) 266;

Recoil separator ERNA: ion beam specification
D. Rogalla, M. Aliotta, C.A. Barnes, L. Campajola, A. D'Onofrio, E. Fritz, L. Gialanella, U. Greife, G. Imbriani, A. Ordine, J. Ossmann, V. Roca, C. Rolfs, M. Romano, C. Sabbarese, D. Schürmann, F. Schümann, F. Strieder, F. Terrasi, S. Theis, and H.-P. Trautvetter
Eur. Phys. J. A 6 (1999) 471;

Robustness of the quantum hall effect, sample size versus sample topology, and quality management of III-V molecular beam epitaxy
R.D. Tscheuschner, S. Hoch, E. Leschinsky, C. Meier, S. Theis, A.D. Wieck
Int. J. Mod. Phys. B 12 (1998) 1147.

Conference Proceedings

Measurement of the $^{21}Na(p,\gamma)^{22}Mg$ Reaction with the DRAGON Separator at TRIUMF-ISAC
A.A. Chen, S. Bishop, L. Buchmann, M.L. Chatterjee, J.M. D'Auria, S. Engel, D. Gigliotti, U. Greife, A. Hussein, D.A. Hutcheon, C. Jewett, J. King, S. Kubono, A. Laird, M. Lamey, R. Lewis, W. Liu, S. Michimasa, A. Olin, D. Ottewell, P. Parker, J. Rogers, F. Strieder, M. Wiescher, C. Wrede
Proceedings of the 17th International Conference on the Application of Accelerators in Research and Industry, CAARI 2002, Denton/USA, November 2002,
submitted;

Nuclear Astrophysics at ISAC with DRAGON: Initial Studies
A. Olin, S. Bishop, L. Buchmann, M.L. Chatterjee, A. Chen, J.M. D'Auria, S. Engel, D. Gigliotti, U. Greife, D. Hunter, A. Hussein, D. Hutcheon, C. Jewett, J. King, S. Kubono, M. Lamey, A.M. Laird, R. Lewis, W. Liu, S. Michimassa, D. Ottewell, P. Parker, J. Rogers, F. Strieder, C. Wrede
Proceedings of the XVI Particles and Nuclei International Conference PANIC 2002, Osaka/Japan, September/October 2002,
submitted;

Measurements with DRAGON on resonances in the $^{21}Na(p,\gamma)^{22}Mg$ reaction with a radioactive beam
S. Engel, S. Bishop, L. Buchmann, M.L. Chatterjee, A. Chen, J.M. D'Auria, D. Gigliotti, U. Greife, D. Hunter, A. Hussein, R. Lewis, W. Liu, A. Olin, D. Ottewell, P. Parker, J. Rogers, F. Strieder, C. Wrede
Proceedings of the Nuclear Physics in Astrophysics conference, 17th International Nuclear Physics Divisional Conference of the EPS, NPDC-17, Debrecen/Hungary, September/October 2002,
accepted for Nuclear Physics A;

Nuclear Astrophysics at DRAGON: The $^{21}Na(p,\gamma)^{22}Mg$ Reaction and Oxygen-Neon Novae
S. Bishop, R.E. Azuma, L. Buchmann, A.A. Chen, M.L. Chatterjee, J.M. D'Auria, S. Engel, D. Gigliotti, U. Greife, D. Hunter, A. Hussein, D. Hutcheon, C. Jewett, J. José, J. King, S. Kubono, M. Lamey, R. Lewis, W. Liu, S. Michimasa, A. Olin, D. Ottewell, P.D. Parker, J. Rogers, C. Wrede
Proceedings of the 7th International Symposium on Nuclei in the Cosmos, NIC VII, Fuji-Yoshida/Japan, July 2002,
Nucl. Phys. A 718 (2003) 263c;

The DRAGON facility for nuclear astrophysics at TRIUMF-ISAC
D. Hutcheon, S. Bishop, L. Buchmann, M.L. Chatterjee, A.A. Chen, J.M. D'Auria, S. Engel, D. Gigliotti, U. Greife, D. Hunter, A. Hussein, C. Jewett, N. Khan, A. Lamey, W. Liu, A. Olin, D. Ottewell, J. Rogers, G. Roy, H. Sprenger and C. Wrede
Proceedings of the 7th International Symposium on Nuclei in the Cosmos, NIC VII, Fuji-Yoshida/Japan, July 2002,
Nucl. Phys. A 718 (2003) 515c;

Results of the $^{21}Na + p$ Experiments at ISAC
R.E. Azuma, S. Bishop, L. Buchmann, M.L. Chatterjee, J.M. D'Auria, T. Davinson, S. Engel, B.R. Fulton, D. Gigliotti, U. Greife, D. Groombridge, D. Hunter, A. Hussein, D. Hutcheon, C. Jewett, J.D. King, N. Khan, S. Kubono, A.M. Laird, M. Lamey, R. Lewis, L. Ling, W. Liu, S. Michimasa, A.S. Murphy, A. Olin, D. Ottewell, P. Parker, A. Shotter, H. Sprenger, F. Strieder, P. Walden, P.J. Woods, C. Wrede
Proceedings of the 7th International Symposium on Nuclei in the Cosmos, NIC VII, Fuji-Yoshida/Japan, July 2002,
Nucl. Phys. A 718 (2003);

Commissioning and Operation of DRAGON
S. Engel for the DRAGON Collaboration
Proceedings of the 14th International Conference on Electromagnetic Isotope Separators and Techniques Related to their Application, EMIS-14, Victoria/Canada, May 2002,
Nucl. Inst. & Meth. in Phys. Res. B 204 (2003) 154;

Testing the ISAC radioactive ion accelerator beam specifications using the $^1H(^{15}N, \alpha\gamma)^{12}C$ *reaction*
S. Engel, L. Buchmann, A. Chen, J.M. D'Auria, D.A. Hutcheon, C. Galovich, D. Gigliotti, U. Greife, D. Hunter, A. Hussein, C.C. Jewett, W. Liu, A. Olin, D. Ottewell, J. Rogers
Proceedings of the 14th International Conference on Electromagnetic Isotope Separators and Techniques Related to their Application, EMIS-14, Victoria/Canada, May 2002,
Nucl. Inst. & Meth. in Phys. Res. B 204 (2003) 416;

Nuclear Astrophysics at ISAC with DRAGON: Initial Studies
A. Olin, S. Bishop, L. Buchmann, M. L. Chatterjee, A. Chen, J.M. D'Auria, S. Engel, D. Gigliotti, U. Greife, D. Hunter, A. Hussein, D. Hutcheon, C. Jewett, J. King, S. Kubono, M. Lamey, A.M. Laird, R. Lewis, W. Liu, S. Michimassa, D. Ottewell, P. Parker, J. Rogers, F. Strieder, M. Wiescher, C. Wrede
Proceedings of the International Conference on Classical Nova Explosions, Sitges/Spain, May 2002,
AIP vol. 637 (2002) 119, eds. M. Hernanz & J. José;

Development of detection systems for low-energy heavy ions at DRAGON
S. Engel, S. Bishop, A. Chen, C. Dale, J.M. D'Auria, U. Giesen, U. Greife, R. Henderson, D. Hunter, D. Hutcheon, R. Openshaw, J. Rogers, C. Rolfs, A. Shotter
Proceedings of the Fifth International Conference on Radioactive Nuclear Beams, RNB 2000, Divonne/France April 2000,
Nucl. Phys. A 701 (2002) 228.

Presentations

The DRAGON is Puffing - First Results of the DRAGON Experiment with Stable and Unstable Beams
Seminar Talk at TRIUMF
Vancouver, British Columbia/Canada, April 2003;

Awakening of the DRAGON
Seminar Talk at Triangle Universities Nuclear Laboratory
Durham, North Carolina/USA, February 2003;

Awakening of the DRAGON
Talk at the TRIUMF Users' Group Annual General Meeting
Vancouver, British Columbia/Canada, December 2002;

Awakening of the DRAGON
Seminar Talk at Louvain-la-Neuve Cyclotron Laboratory
Louvain-la-Neuve/Belgium, November 2002;

Awakening of the DRAGON
Contributed Talk at the 17th International Nuclear Physics Divisional Conference of the EPS, Nuclear Physics in Astrophysics, NPDC
Debrecen/Hungary, September 2002;

Commissioning of the DRAGON
Poster at the 7th International Conference on Nuclei in the Cosmos, NIC 2002
Fuji-Yoshida/Japan, July 2002;

Commissioning and Operation of DRAGON
Contributed Talk at the 14th International Conference on Electromagnetic Isotope Separators and Techniques Related to Their Application, EMIS 2002
Victoria, British Columbia/Canada, May 2002;

Commissioning of the Detector of Recoils and Gammas of Nuclear Reactions, DRAGON at TRIUMF
Contributed Talk at the 38th Western Regional Nuclear and Particle Physics Conference
Lake Louise, Alberta/Canada, February 2001;

Development of Detection Systems for Low-Energy Heavy Ions at DRAGON
Poster at the 6th International Conference on Nuclei in the Cosmos, NIC 2000
Aarhus/Danemark, June 2000;

Development of Detection Systems for Low-Energy Heavy Ions at DRAGON
Poster at the 5th International Conference on Radioactive Nuclear Beams, RNB 2000
Divonne/France, April 2000;

Effizienter Nachweis der Reaktionsprodukte aus astrophysikalisch relevanten Fusionen
Poster at the DPG Frühjahrstagung, Fachverband Physik der Hadronen und Kerne
Freiburg/Germany, March 1999.